PRIMUS: CONSTRAINTS ON STAR FORMATION QUENCHING AND GALAXY MERGING, AND THE EVOLUTION OF THE STELLAR MASS FUNCTION FROM $z = 0$–1

John Moustakas[1], Alison L. Coil[2,11], James Aird[3], Michael R. Blanton[4], Richard J. Cool[5], Daniel J. Eisenstein[6], Alexander J. Mendez[2], Kenneth C. Wong[7], Guangtun Zhu[8], and Stéphane Arnouts[9,10]

[1] Department of Physics and Astronomy, Siena College, 515 Loudon Road, Loudonville, NY 12211, USA; jmoustakas@siena.edu
[2] Center for Astrophysics and Space Sciences, Department of Physics, University of California, 9500 Gilman Dr., La Jolla, CA 92093, USA
[3] Department of Physics, Durham University, Durham DH1 3LE, UK
[4] Center for Cosmology and Particle Physics, Department of Physics, New York University, 4 Washington Place, New York, NY 10003, USA
[5] MMT Observatory, University of Arizona, 1540 E Second Street, Tucson, AZ 85721, USA
[6] Harvard-Smithsonian Center for Astrophysics, 60 Garden Street, Cambridge, MA 02138, USA
[7] Steward Observatory, University of Arizona, 933 North Cherry Avenue, Tucson, AZ 85721, USA
[8] Department of Physics and Astronomy, The Johns Hopkins University, 3400 North Charles Street, Baltimore, MD 21218, USA
[9] Canada-France-Hawaii Telescope Corporation, 65-1238 Mamalahoa Hwy, Kamuela, HI 96743, USA
[10] Aix Marseille Université, CNRS, LAM (Laboratoire d'Astrophysique de Marseille) UMR 7326, F-13388 Marseille, France

ABSTRACT

We measure the evolution of the stellar mass function (SMF) from $z = 0$–1 using multi-wavelength imaging and spectroscopic redshifts from the PRism MUlti-object Survey (PRIMUS) and the Sloan Digital Sky Survey (SDSS). From PRIMUS we construct an $i < 23$ flux-limited sample of ∼40,000 galaxies at $z = 0.2$–1.0 over five fields totaling ≈5.5 deg^2, and from the SDSS we select ∼170,000 galaxies at $z = 0.01$–0.2 that we analyze consistently with respect to PRIMUS to minimize systematic errors in our evolutionary measurements. We find that the SMF of all galaxies evolves relatively little since $z = 1$, although we do find evidence for mass assembly downsizing; we measure a ≈30% increase in the number density of ∼$10^{10}\,\mathcal{M}_\odot$ galaxies since $z \approx 0.6$, and a ≲10% change in the number density of all ≳$10^{11}\,\mathcal{M}_\odot$ galaxies since $z \approx 1$. Dividing the sample into star-forming and quiescent using an evolving cut in specific star formation rate, we find that the number density of ∼$10^{10}\,\mathcal{M}_\odot$ star-forming galaxies stays relatively constant since $z \approx 0.6$, whereas the space density of ≳$10^{11}\,\mathcal{M}_\odot$ star-forming galaxies decreases by ≈50% between $z \approx 1$ and $z \approx 0$. Meanwhile, the number density of ∼$10^{10}\,\mathcal{M}_\odot$ quiescent galaxies increases steeply toward low redshift, by a factor of ∼2–3 since $z \approx 0.6$, while the number of massive quiescent galaxies remains approximately constant since $z \approx 1$. These results suggest that the rate at which star-forming galaxies are quenched increases with decreasing stellar mass, but that the bulk of the stellar mass buildup within the quiescent population occurs around ∼$10^{10.8}\,\mathcal{M}_\odot$. In addition, we conclude that mergers do not appear to be a dominant channel for the stellar mass buildup of galaxies at $z < 1$, even among massive (≳$10^{11}\,\mathcal{M}_\odot$) quiescent galaxies.

Key words: galaxies: evolution – galaxies: high-redshift – large-scale structure of universe – surveys

Online-only material: color figures

1. INTRODUCTION

Surveys of the galaxy population in the nearby universe such as the Sloan Digital Sky Survey (SDSS; York et al. 2000) have found that the distributions of many galaxy properties, including color, morphology, and star formation rate (SFR), are bimodal, reflecting the existence of two broad types of galaxies: blue, star-forming disk galaxies, and red, quiescent (i.e., non star-forming) spheroidal or elliptical galaxies (e.g., Kauffmann et al. 2003b; Blanton et al. 2003a; Baldry et al. 2004; Wyder et al. 2007). At low redshift, quiescent galaxies tend to be luminous and massive, and are prevalent in dense environments such as groups and clusters, whereas star-forming galaxies typically have lower stellar masses and are more commonly found in the field (Blanton & Moustakas 2009, and references therein). These broad empirical trends have been shown to persist at least to $z \sim 3$ (e.g., Bell et al. 2004; Cooper et al. 2007; Cassata et al. 2008; Brammer et al. 2009; Whitaker et al. 2011). Understanding how these two populations come into existence and evolve with cosmic time, therefore, is a fundamental outstanding problem in observational cosmology.

Galaxy bimodality is likely a consequence of star formation in some galaxies being *quenched*—shut off—relatively quickly. A wide variety of quenching mechanisms have been proposed to match the observed distributions of galaxy properties, including: major-merger induced feedback from star formation and supermassive black holes (Springel et al. 2005; Di Matteo et al. 2005); processes that prevent galaxies from replenishing their cold-gas supply such as virial shock heating (Kereš et al. 2005; Dekel & Birnboim 2006), often in concert with so-called radio-mode feedback from an accreting active galactic nucleus (AGN; Croton et al. 2006; Cattaneo et al. 2006; Gabor et al. 2011); and internal, secular quenching due to disk or bar instabilities (Cole et al. 2000; Martig et al. 2009). Late-type galaxies whose host halos are accreted by larger dark-matter halos (i.e., by groups and clusters) are also susceptible to *environmental* quenching, such as ram-pressure stripping (Gunn & Gott 1972), strangulation or starvation (Larson et al. 1980; Balogh et al. 2000), and gravitational harassment (Moore et al. 1998; see Boselli & Gavazzi 2006 for a review).

By incorporating these quenching mechanisms into a coherent cosmological framework, modern theoretical models have become reasonably successful at reproducing a wide range of galaxy properties, including galaxy bimodality (e.g., Hopkins

et al. 2008a, 2008b; Somerville et al. 2008; Bower et al. 2012). However, many discrepancies between observations and predictions persist (e.g., Fontana et al. 2006; Fontanot et al. 2009; Kereš et al. 2009; Davé et al. 2011a, 2011b; Lu et al. 2012; Weinmann et al. 2012). The exact cause of these problems is hard to determine because of the complexities of modeling the small-scale physics of star formation, feedback, and black-hole accretion. Consequently, empirical constraints on the relative fraction of quiescent and star-forming galaxies as a function of stellar mass, redshift, environment, AGN content, and dark-matter halo mass are critical for determining galaxy quenching, and the evolution of galaxy bimodality (e.g., Weinmann et al. 2006; Bell et al. 2007; Kimm et al. 2009; Peng et al. 2010; Wetzel et al. 2012; Aird et al. 2012; Knobel et al. 2012; Woo et al. 2013).

In this paper, we focus on one key aspect of this problem by measuring the stellar mass functions (SMFs) of quiescent and star-forming galaxies from $z = 0$–1, spanning the last $\sim$8 billion years of cosmic time. The SMF measures the comoving space density of galaxies of a given stellar mass, making it a powerful observational tracer of galaxy growth by in situ star formation, mergers, and galaxy transformations due to star formation quenching (e.g., Drory & Alvarez 2008; Peng et al. 2010). Measurements of the SMF are also important for connecting the physics of galaxy formation to the hierarchical assembly of dark matter halos, and large-scale structure (e.g., Conroy & Wechsler 2009; Cattaneo et al. 2011; Wang et al. 2012; Leauthaud et al. 2012; Behroozi et al. 2012).

Deep extragalactic surveys in the last decade have begun to characterize the evolution of galaxy bimodality over a significant fraction of the age of the universe. At the highest redshifts, $z \gtrsim 2$, studies have shown that although quiescent galaxies exist, they are outnumbered by star-forming galaxies at all stellar masses (e.g., Whitaker et al. 2010; Domínguez Sánchez et al. 2011). This early epoch is followed by a period of rapid growth in the space density of massive ($\gtrsim 10^{11}\,\mathcal{M}_\odot$) quiescent galaxies between $z \sim 2$ and $z \sim 1$ (Arnouts et al. 2007; Ilbert et al. 2010; Nicol et al. 2011; Brammer et al. 2011; Mortlock et al. 2011). By $z \sim 1$, the stellar mass dependence of galaxy bimodality as observed locally is largely in place: star-forming galaxies outnumber quiescent galaxies at the low-mass end of the SMF, while quiescent galaxies dominate the massive galaxy population (e.g., Bundy et al. 2006; Borch et al. 2006). Subsequently, between $z \sim 1$ and $z \sim 0$, the transformation of star-forming galaxies into quiescent, passively evolving galaxies continues, leading to an approximately factor of two increase in the integrated stellar mass density of quiescent galaxies (Bell et al. 2004; Blanton 2006; Faber et al. 2007). The bulk of this stellar mass growth appears to be due to a rapidly rising population of intermediate-mass ($\sim 10^{10}\,\mathcal{M}_\odot$) quiescent galaxies, although the extent to which massive galaxies also grow through stellar accretion (i.e., mergers) remains controversial (Cimatti et al. 2006; Scarlata et al. 2007; Brown et al. 2007; Rudnick et al. 2009; Stewart et al. 2009; Ilbert et al. 2010; Pozzetti et al. 2010; Robaina et al. 2010; Maraston et al. 2012). By the current epoch, quiescent galaxies vastly outnumber star-forming galaxies above $\sim 3 \times 10^{10}\,\mathcal{M}_\odot$, and account for more than half of the total stellar mass in the local universe (Bell et al. 2003; Baldry et al. 2004; Driver et al. 2006).

Despite significant progress, however, the detailed evolution of the SMFs of quiescent and star-forming galaxies since $z \sim 1$ remains relatively uncertain, leaving several unresolved issues.

One outstanding question is whether massive galaxies assemble their stellar mass earlier (i.e., at higher redshift) relative to lower-mass galaxies—that is, do galaxies undergo *mass assembly downsizing*?[12] Mass assembly downsizing poses a significant challenge for theoretical models, which predict the late-time assembly of massive galaxies (i.e., *mass assembly upsizing*; e.g., De Lucia et al. 2006); however, different observational studies have reached different conclusions (e.g., Pérez-González et al. 2008; Fontanot et al. 2009).

Another open question is the role of major and minor mergers for the stellar mass growth of galaxies at $z < 1$. Because the merger rate is notoriously difficult to measure directly (e.g., Lotz et al. 2011), measurements of the SMF as a function of redshift can place complementary constraints on the merger-driven growth of galaxies (e.g., Drory & Alvarez 2008; Pozzetti et al. 2010), in addition to constraining the buildup of the diffuse stellar component (or intercluster light) of groups and clusters (e.g., Murante et al. 2007; Gonzalez et al. 2007).

Finally, it remains poorly understood why the SMF of star-forming galaxies evolves relatively little from $z = 0$–1, despite vigorous ongoing star formation. In particular, it is not known why the stellar mass growth by in situ star formation balances—almost perfectly—the stellar mass growth of the quiescent galaxy population due to quenching (see, e.g., Arnouts et al. 2007; Martin et al. 2007; Peng et al. 2010).

Answers to these and related questions have remained elusive at intermediate redshift because a combination of depth, area, and large sample is needed to characterize the shape of the SMF over a large dynamic range of stellar mass, while simultaneously minimizing the effects of sample variance.[13] For example, Moster et al. (2011) estimate a $\sim$25% uncertainty in the number density of $\sim 10^{11}\,\mathcal{M}_\odot$ galaxies in a $\Delta z = 0.1$ wide redshift bin at $z = 0.5$ due to sample variance in the $\sim$2 deg^2 Cosmic Evolution Survey (COSMOS) field, which is among the largest extragalactic deep fields with high-quality spectroscopic and medium-band photometric redshifts (Scoville et al. 2007; Ilbert et al. 2009). Although broadband photometric redshifts enable the SMF to be constructed over larger areas (e.g., Matsuoka & Kawara 2010), the redshift precision typically achieved by these methods, $\sigma_z/(1 + z) \approx 1\%$–5%, can significantly bias the inferred shape of the SMF, and its evolution with redshift. Finally, previous studies have frequently relied on published measurements of the local SMF (e.g., from the SDSS), although the amount of evolution inferred can be significantly affected by systematic differences in how stellar masses are derived (Marchesini et al. 2009; Bernardi et al. 2010).

We alleviate many of these issues by measuring the evolution of the SMF at intermediate redshift using data from the PRism MUlti-object Survey (PRIMUS; Coil et al. 2011; Cool et al. 2013). From PRIMUS we select $\sim$40,000 galaxies at $z = 0.2$–1 with high-quality spectroscopic redshifts and deep multi-wavelength imaging in the ultraviolet (UV) from the *Galaxy Evolution Explorer* (*GALEX*; Martin et al. 2005), in the mid-infrared from the *Spitzer Space Telescope* (Werner et al. 2004) Infrared Array Camera (IRAC; Fazio et al. 2004), and in the optical and near-infrared from a variety of ground-based surveys. The broad wavelength coverage allows us to

---

[12] Also called *downsizing in stellar mass* in the extensive study of the various manifestations of downsizing by Fontanot et al. (2009).

[13] *Sample variance* refers to the variation in the number density of galaxies along a given line-of-sight due to large-scale clustering. The more commonly adopted term *cosmic variance* should only strictly be used in the context of the existence of just one (observable) universe.

estimate stellar masses and SFRs using detailed spectral energy distribution (SED) modeling, and to robustly identify quiescent and star-forming galaxies over the full redshift range. The total area subtended by this sample is ≈ 5.5 deg^2, making it the largest statistically complete sample of faint galaxies with spectroscopic redshifts ever assembled. Furthermore, we construct the SMF at $z \approx 0.1$ using a sample of $\sim$170,000 SDSS galaxies at $z = 0.01$–0.2 with UV, optical, and near-infrared photometry from *GALEX*, the Two Micron All Sky Survey (2MASS; Skrutskie et al. 2006), and the *Wide-field Infrared Survey Explorer* (*WISE*; Wright et al. 2010) that we analyze using the same methodology as PRIMUS to minimize systematic errors in the evolutionary trends we measure.

Using these data, we measure the evolution in the number and stellar mass density of quiescent and star-forming galaxies since $z \approx 1$, in order to quantify their stellar mass growth by star formation and mergers, and to constrain the physical mechanisms responsible for quenching. In Section 2 we present the *GALEX*, optical, and IRAC photometry of galaxies in the PRIMUS fields that we use, and we describe how we construct our local SDSS comparison sample. We select our parent sample of quiescent and star-forming galaxies in Section 3, and in Section 4 we describe the methodology we use to construct a statistically complete SMF for both quiescent and star-forming galaxies in seven redshift bins from $z = 0$–1. We present our SMFs and quantify the number and stellar mass density evolution of each galaxy type in Section 5, and quantify the role of galaxy growth by mergers and star formation quenching in Section 6. Finally, we summarize our results in Section 7.

Given the length of the paper, readers interested in our principal results can skip ahead to Section 5 (see especially Figures 11 and 12), and to the interpretation of our results in Section 6.

We adopt a concordance cosmology with $\Omega_m = 0.3$, $\Omega_\Lambda = 0.7$, and $h_{70} \equiv H_0/(70\,\mathrm{km\,s^{-1}\,Mpc^{-1}}) = 1.0$, and the AB magnitude system (Oke & Gunn 1983) throughout. Unless otherwise indicated, all stellar masses and SFRs assume a universal Chabrier (2003) initial mass function (IMF) from 0.1–$100\,\mathcal{M}_\odot$.

2. OBSERVATIONS

Our analysis of the SMF at intermediate redshift combines multi-wavelength imaging of five distinct extragalactic deep fields with spectroscopic redshifts from PRIMUS. In Section 2.1 we briefly describe PRIMUS and introduce the fields that we analyze. We describe our analysis of the deep *GALEX*/UV imaging of these fields in Section 2.2, and the optical and mid-infrared photometric catalogs we use in Section 2.3. Finally, in Section 2.4 we describe how we construct our $z \approx 0.1$ SDSS galaxy sample.

2.1. PRIMUS

PRIMUS is a large faint-galaxy intermediate-redshift survey which obtained precise ($\sigma_z/(1 + z) \approx 0.5\%$) spectroscopic redshifts for a statistically complete sample of $\sim$120,000 galaxies at $z \approx 0$–1.2. The survey targeted galaxies in seven distinct extragalactic deep fields, totaling $\sim$9 deg^2, with a wealth of ancillary multi-wavelength imaging from the X-ray to the far-infrared. PRIMUS was conducted using the IMACS spectrograph (Bigelow & Dressler 2003) on the Magellan I Baade 6.5 m telescope with a slitmask and low-dispersion prism. This novel experimental design yielded low-resolution

($\lambda/\Delta\lambda \sim 40$) spectra for $\sim$2000 objects per slitmask, which is a factor of $\sim$10 higher multiplexing rate than traditional spectroscopic redshift surveys (see also Kelson et al. 2012). The full details of the survey design, targeting, and data summary are in Coil et al. (2011), while the details of the data reduction, redshift fitting and precision, and survey completeness can be found in Cool et al. (2013).

In this paper we restrict our analysis to the fields targeted by PRIMUS with *GALEX* and *Spitzer*/IRAC imaging. Three of these fields are part of the *Spitzer* Wide-area Infrared Extragalactic Survey (SWIRE;[14] Lonsdale et al. 2003): the European Large Area ISO Survey—South 1 field (ELAIS-S1;[15] Oliver et al. 2000); the *Chandra* Deep Field South SWIRE field (hereafter, CDFS); and the XMM Large Scale Structure Survey field (XMM-LSS; Pierre et al. 2004). In detail, the XMM-LSS field in PRIMUS consists of two separate (but spatially adjacent) subfields: the Subaru/*XMM-Newton* DEEP Survey field (XMM-SXDS;[16] Furusawa et al. 2008), and the Canada–France–Hawaii Telescope Legacy Survey (CFHTLS) field (hereafter, XMM-CFHTLS[17]). These fields were targeted by PRIMUS using different photometric catalogs; therefore, because of the slightly different selection functions we treat them separately in our analysis of the SMF. Finally, we include in our analysis the well-studied COSMOS[18] field (Scoville et al. 2007), giving a total of five distinct fields.

2.2. Ultraviolet Photometry

All five fields in our sample were observed in the near-UV (NUV) and far-UV (FUV) as part of the *GALEX* Deep Imaging Survey (DIS; Martin et al. 2005; Morrissey et al. 2005). The mean exposure times of these observations range from 58–78 ks in our COSMOS field, to between 15–42 ks in our ELAIS-S1, CDFS (but one with 90 ks), and XMM-SXDS and XMM-CFHTLS (but one with 150 ks) fields, making these among the deepest UV observations ever obtained.

Given the $4\farcs2$ and $5\farcs3$ FWHM point-spread function (PSF) of the *GALEX* telescope in the FUV and NUV, respectively, in $\gtrsim$10 ks exposures source confusion is a significant problem, requiring great care when extracting a photometric catalog. Therefore, to minimize contamination from neighboring sources, we use the Bayesian photometric code EMPHOT, which is based on the expectation maximization (EM) algorithm of Guillaume et al. (2006). EMPHOT uses optical positional priors to measure the UV fluxes of objects in the *GALEX* images by adjusting a model of the *GALEX* PSF. The prior positions are based on deep, high-resolution optical imaging of the same field in the bluest available band (see Section 2.3). EMPHOT has been used successfully in several previous studies to analyze deep *GALEX* imaging (Xu et al. 2005; Zamojski et al. 2007; Salim et al. 2009; Hammer et al. 2010), so we refer the interested reader to those papers for additional details.

2.3. Optical and Mid-infrared Photometry

In this section we describe the ground-based optical and *Spitzer*/IRAC mid-infrared photometric catalogs that we utilize in each field. As most of these catalogs are publicly available, we defer many of the finer details to the corresponding data release

---

[14] http://swire.ipac.caltech.edu/swire/swire.html
[15] http://dipastro.pd.astro.it/esis
[16] http://www.naoj.org/Science/SubaruProject/SDS
[17] http://www.cfht.hawaii.edu/Science/CFHLS
[18] http://cosmos.astro.caltech.edu

documentation and papers cited below; additional details can also be found in Coil et al. (2011).

Our general strategy for obtaining integrated (total) fluxes in all photometric bands is to use circular aperture photometry to constrain the shape of the SED of each galaxy, and then to tie the overall normalization of the SED to an estimate of the total magnitude in the detection band (usually i' or R). The strengths of this procedure are that aperture colors are less affected by neighboring sources, and they typically have higher signal-to-noise ratios than total magnitudes measured in each band independently. In three of our fields—XMM-SXDS, XMM-CFHTLS, and COSMOS—aperture colors have been measured from PSF matched images and so should be very accurate; in the other two fields—CDFS and ELAIS-S1—the aperture colors are not measured from PSF-matched mosaics, so for these sources we adopt slightly higher minimum photometric uncertainties when performing our SED modeling (see Section 4.1).

2.3.1. CDFS, ELAIS-S1, XMM-SXDS, and XMM-CFHTLS

In the CDFS field we use the ground-based optical photometric catalogs distributed as part of the SWIRE Data Release 2/3, as described in the SWIRE Data Delivery Document.[19] The SWIRE team obtained $Ug'r'i'z'$ imaging of this field using the MOSAIC-II imager at the CTIO/Blanco 4 m telescope, achieving a depth in each band of 25.2, 25.3, 25.2, 24.4, and 23.8 mag (5σ) for a point source in a $2''$ diameter aperture (Norris et al. 2006).[20] Source catalogs were generated (by the SWIRE team) in each bandpass individually using the Cambridge Astronomical Survey Unit (CASU[21]) pipeline, and then merged using the *Spitzer* Science Center bandmerge[22] software package. We adopt the fluxes measured in a fixed $2\rlap{.}''4$ diameter aperture, scaled to match CASU's estimate of the integrated i' flux.

In the ELAIS-S1 field we use the *BVR* and *Iz* catalogs published by Berta et al. (2006, 2008).[23] The *BVR* imaging was obtained using the Wide Field Imager (WFI) at the 2.2 m La Silla ESO-MPI telescope, achieving a depth of 24.9, 25.0, and 24.7 mag in B, V, and R, respectively. The *I*- and z-band observations were obtained using the VIsible Multi Object Spectrograph (VIMOS; Le Fèvre et al. 2003) camera at the VLT 8.2 m telescope, reaching a depth of $\sim$23.3 and $\sim$22.8 mag, respectively. All the quoted depths correspond to the 95% completeness limit for point sources. The publicly released photometric catalogs were generated using SExtractor (Bertin & Arnouts 1996). We adopt the aperture fluxes measured in a $3\rlap{.}''3$ diameter aperture, scaled to the MAG_AUTO (total) R-band magnitude.

Finally, in the XMM-SXDS and XMM-CFHTLS fields we rely on the high-fidelity $u^*g'r'i'z'$ photometric catalogs generated as part of the CFHTLS Archive Research Survey (CARS; Erben et al. 2009).[24] These catalogs are based on deep imaging obtained as part of the CFHTLS-Wide survey using the CFHT/Megacam camera (Boulade et al. 2003).[25] The CARS mosaics reach a 5σ depth of 25.2, 25.3, 24.4, 24.7, and 23.2 mag in a $2''$ diameter aperture in u^*, g', r', i', and z', respectively. The CARS photometric catalogs were generated from PSF-matched images

using SExtractor in dual-image mode, with the unconvolved i' mosaic serving as the detection image. We use the fluxes measured in a $3''$ diameter aperture, scaled to the MAG_AUTO magnitude measured from the unconvolved i'-band mosaic.

In addition to the ground-based optical observations described above, all four of the preceding fields were also observed at 3.6, 4.5, 5.8, and 8 μm with *Spitzer*/IRAC as part of SWIRE. We use the SWIRE Data Release 2/3 IRAC catalogs matched to the galaxies in PRIMUS using a $1''$ search radius. These catalogs are complete for point sources to a 5σ depth of 22.2, 21.5, 19.8, and 19.9 mag at 3.6, 4.5, 5.8, and 8 μm, respectively. Following the SWIRE Data Delivery document, we use the fluxes measured in a $3\rlap{.}''8$ diameter circular aperture, multiplied by an aperture correction derived in each band from isolated point sources (see also Surace et al. 2004; Ilbert et al. 2009).[26] These aperture-corrected fluxes optimize the trade-off between crowding, which favors a smaller aperture, and signal-to-noise ratio, which favors a larger aperture, and provide a reasonably accurate measurement of the total IRAC flux (see the SWIRE Data Delivery Document).

2.3.2. COSMOS

In the COSMOS field we rely on the multi-wavelength photometric catalog publicly released in 2009 April by the COSMOS team (see Capak et al. 2007).[27] This catalog includes $V_Jg^+r^+i^+z^+$ imaging obtained using the Suprime-Cam instrument (Miyazaki et al. 2002) on the Subaru 8.2 m telescope; u^*i^* imaging from the Megacam camera (Boulade et al. 2003) on the 3.6 m Canada–France–Hawaii Telescope (CFHT); and K_s-band imaging obtained using the Wide-field InfraRed Camera (WIRCam; Puget et al. 2004) on the CFHT (McCracken et al. 2010).[28] In a $3''$ diameter aperture, these images achieve a 5σ depth of 26.5, 26.6, 26.1, 23.5, and 25.1 mag in u^*, g^+, V_J, r^+, i^+, i^*, and z^+, respectively; the near-infrared imaging is more than 90% complete for point sources to $K_s = 23$. The COSMOS optical/near-infrared photometric catalog was generated from PSF-matched mosaics using SExtractor in dual-image mode, with the unconvolved i^+ mosaic as the detection image. We use the fluxes measured in a $3''$ diameter aperture, scaled to the i^+ MAG_AUTO magnitude measured from the unconvolved i^+-band mosaic.

We supplement these optical/near-infrared data with mid-infrared photometry generated by A. J. Mendez et al. (in preparation) using the public *Spitzer*-COSMOS[29] (S-COSMOS) IRAC mosaics (Sanders et al. 2007). The catalogs were generated using the same tools utilized by the SWIRE team (see Section 2.3.1), thereby ensuring that our IRAC photometry is consistent across all five fields; nevertheless, A. J. Mendez et al. (in preparation) demonstrate that their photometric measurements and uncertainties agree in the mean with the S-COSMOS/IRAC catalogs publicly released by the COSMOS team in 2007 June.[30] The catalogs are statistically complete for point sources brighter than 24.0, 23.3, 21.3, and 21.0 mag (5σ) in each of the four IRAC

[19] http://irsa.ipac.caltech.edu/data/SPITZER/SWIRE
[20] http://www.astro.caltech.edu/~bsiana/cdfs_opt
[21] http://casu.ast.cam.ac.uk
[22] http://ssc.spitzer.caltech.edu/dataanalysistools/tools/bandmerge
[23] http://www.astro.unipd.it/esis
[24] ftp://marvinweb.astro.uni-bonn.de/data_products/CARS_catalogues
[25] http://www.cfht.hawaii.edu/Science/CFHLS

[26] For reference, the aperture correction factors we use, as measured by the SWIRE team, are 0.736, 0.716, 0.606, and 0.543 at 3.6, 4.5, 5.8, and 8 μm, respectively. (The fluxes are *divided* by these factors.)
[27] http://irsa.ipac.caltech.edu/data/COSMOS
[28] We do not use the Subaru B_J- and V_J-band imaging of the COSMOS field, nor the UKIRT J-band imaging, because of their larger-than-average photometric zeropoint uncertainties (Ilbert et al. 2009).
[29] http://irsa.ipac.caltech.edu/data/SPITZER/S-COSMOS
[30] http://irsa.ipac.caltech.edu/data/COSMOS/gator_docs/scosmos_irac_colDescriptions.html

channels. As for the other four fields, we use the aperture-corrected 3″.8 diameter aperture fluxes and match each IRAC source to our PRIMUS sample using a 1″ search radius.

2.4. SDSS-GALEX Sample

An accurate measurement of the SMF at the current epoch is crucial because it provides a low-redshift anchor against which we can quantify the stellar mass buildup of galaxies through cosmic time. Although many previous studies have measured the local SMF for the global galaxy population (see Section 5.1), few have exploited the bimodality of the SFR versus stellar mass diagram to separately measure the SMFs of quiescent and star-forming galaxies. Moreover, given the susceptibility of stellar mass estimates to a variety of model-dependent systematic uncertainties (see, e.g., Marchesini et al. 2009; Bernardi et al. 2010; Appendix B), it is important that we measure the local SMF using the same assumptions and methodology used to generate the SMF of intermediate-redshift galaxies.

With these considerations in mind, we select a sample of low-redshift galaxies using the SDSS Data Release 7 (DR7; Abazajian et al. 2009), which provides high-fidelity *ugriz* photometry and spectroscopic redshifts for hundreds of thousands of galaxies in the nearby universe. Specifically, we select 504,437 galaxies from the New York University Value-Added Galaxy Catalog (VAGC;[31] Blanton et al. 2005b) that satisfy the main sample criteria defined by Strauss et al. (2002), and have Galactic extinction corrected (Schlegel et al. 1998) Petrosian magnitudes $14.5 < r < 17.6$, and spectroscopic redshifts $0.01 < z < 0.2$. Excluding areas of the survey that were masked because of bright stars and other artifacts (Blanton et al. 2005b), this sample covers 6956 deg². The VAGC also provides an estimate of the statistical weight for each galaxy, which we use to correct the sample for targeting incompleteness (generally due to fiber collisions) and redshift failures (Blanton et al. 2003c).

Next, we restrict the parent SDSS sample to galaxies with medium-depth observations from *GALEX*; UV photometry is needed to effectively divide the sample into quiescent and star-forming galaxies (see Section 3.2). First, we retrieve the positions of all the *GALEX* tiles publicly available as part of the *GALEX* Release 6 (GR6) with a total exposure time greater than 1 ks, which consists of more than 5400 tiles covering roughly 4450 deg² of the sky. The 1 ks exposure time cut is the minimum time necessary to obtain an accurate measurement of the total UV flux of extended sources at the typical redshift of galaxies in the SDSS (Wyder et al. 2007). Next, we use mangle[32] (v2.2; Hamilton & Tegmark 2004; Swanson et al. 2008) to construct the angular selection function of the joint SDSS-*GALEX* sample. For the SDSS we use the mangle polygons distributed as part of the VAGC, while for each *GALEX* pointing we adopt a simple 1°.1 diameter circular field-of-view (Morrissey et al. 2007). The final sample comprises 169,727 SDSS galaxies with *GALEX* imaging distributed over 2505 deg².

With the relevant list of objects in hand, we use the MAST/CasJobs[33] interface and a 4″ diameter search radius (Budavári et al. 2009) to retrieve the NUV and FUV photometry of the galaxies in our sample. We resolve duplicate *GALEX* observations due to overlapping tiles by selecting the measurement with the highest signal-to-noise ratio, and adopt the SExtractor MAG_AUTO magnitude (Bertin & Arnouts 1996) measured in the

Table 1
Sample Properties

Field	Selection Band	Magnitude Limit[b]	Ω[a] (deg²)	N[c]
CDFS[d]	i'	23.0	1.496	8050
COSMOS	I	23.0	0.856	7290
ELAIS-S1[d]	R	23.2	0.800	4140
XMM-SXDS	i'	23.0	0.646	6403
XMM-CFHTLS	i'	23.0	1.700	14547
PRIMUS[e]			5.499	40430
SDSS-*GALEX*	r	17.6	2504	169727

Notes.
[a] Angular area surveyed.
[b] Corrected for foreground Galactic extinction.
[c] Number of galaxies satisfying the selection criteria given in Section 3.1.
[d] Due to differences in the PRIMUS experimental design, our CDFS and ELAIS-S1 samples are also flux-limited in the 3.6 μm IRAC band between $17 < [3.6] < 21$.
[e] Combination of all five fields.

NUV band as an estimate of the total NUV flux. For the FUV photometry we use the FUV flux measured inside the elliptical aperture defined in the NUV band to ensure accurate galaxy colors.

For the *ugriz* bands we use the SDSS model magnitudes, which provide reliable, high signal-to-noise measurements of the optical colors of each galaxy (Stoughton et al. 2002). We scale the *ugriz* photometry to the *r*-band cmodel magnitude, which provides the most reliable estimate of the total (integrated) galaxy flux irrespective of galaxy type (Abazajian et al. 2004; Bernardi et al. 2010; Blanton et al. 2011). Finally, we supplement our UV and optical photometry with integrated *JHK$_s$* magnitudes from the 2MASS Extended Source Catalog (XSC; Jarrett et al. 2000), and with integrated photometry (or upper limits) at 3.4 and 4.6 μm from the *WISE* All-Sky Data Release.[34]

3. SAMPLE SELECTION

In Section 3.1 we define the PRIMUS parent sample, and in Section 3.2 we describe the criteria we use to select quiescent and actively star-forming galaxies as a function of redshift.

3.1. Parent Sample

We select our parent sample from the statistically complete *primary* sample of galaxies observed by PRIMUS (see Coil et al. 2011 for full details). In Table 1 we list the optical selection band and the corresponding magnitude limits we impose to define the parent sample in each of our five fields. These limits are $18 < i' < 23$ in the CDFS, XMM-SXDS, and XMM-CFHTLS fields, $18 < I < 23$ in COSMOS, and $18 < R < 23.2$ in ELAIS-S1. Due to differences in the PRIMUS experimental design, the sample of galaxies targeted for spectroscopy in the CDFS and ELAIS-S1 fields were also required to be detected in IRAC imaging at 3.6 μm; therefore, we further require our parent sample of galaxies in these two fields to have $17 < [3.6] < 21$. We emphasize that having our sample flux-limited in both the optical and mid-infrared does not preclude us from determining the SMF in these two fields, as we account for both flux limits in our analysis (see Section 4.3).

[31] http://sdss.physics.nyu.edu/vagc
[32] http://space.mit.edu/~molly/mangle
[33] http://galex.stsci.edu/casjobs

[34] http://wise2.ipac.caltech.edu/docs/release/allsky

Next, we construct the angular selection (window) function of our sample by joining the PRIMUS, *GALEX*, and IRAC window functions using `mangle`. The final window function includes regions of the sky with *GALEX* and IRAC imaging, and ensures coverage from two or more PRIMUS slitmasks, thereby minimizing targeting incompleteness due to slit collisions. The solid angle of each field ranges from 0.80 deg^2 in ELAIS-S1 to 1.70 deg^2 in the XMM-CFHTLS field, totaling 5.50 deg^2 (see Table 1).

Finally, we select objects spectroscopically classified as galaxies by the PRIMUS pipeline (thereby excluding stars and broad-line AGNs; see Cool et al. 2013 for details) with high-quality ($Q \geqslant 3$) spectroscopic redshifts in the range $z = 0.2$–1.0. Below $z = 0.2$ PRIMUS is severely limited by sample variance, while our upper redshift cut eliminates <5% of the primary sample. The redshift confidence cut $Q \geqslant 3$ balances the need for a large sample while minimizing the catastrophic outlier rate and maximizing the redshift precision. Based on a comparison with redshifts derived from high-resolution spectroscopy, we estimate that the redshift precision of our sample is $\sigma_z/(1 + z) \approx 0.4\%$, with a catastrophic outlier rate of $\lesssim 3\%$. Table 1 lists the final number of galaxies in our sample.

To correct our sample for targeting incompleteness and redshift failures, we use the statistical weights described by Coil et al. (2011) and Cool et al. (2013). Briefly, we assign a statistically derived weight, w_i, to each galaxy given by

$$w_i = (f_{\text{target}} \times f_{\text{collision}} \times f_{\text{success}})^{-1}, \qquad (1)$$

where f_{target} is the fraction of galaxies that passed the PRIMUS magnitude- and density-dependent target selection criteria; $f_{\text{collision}}$ is the fraction of potential targets observed spectroscopically (i.e., whose spectrum would not collide, or overlap with another potential target); and f_{success} is the fraction of galaxies in a given bin of apparent magnitude and color (typically $g - r$ or $B - R$) that yielded a robust (i.e., $Q \geqslant 3$) redshift. Both the targeting fraction ($f_{\text{target}} \approx 80\%$; Coil et al. 2011) and the fraction of targets observed ($f_{\text{collision}} \approx 95\%$; Cool et al. 2013) are high in PRIMUS due to its novel experimental design and survey strategy. The redshift success rate decreases smoothly with apparent magnitude—essentially, spectroscopic signal-to-noise ratio—and varies weakly with observed-frame color. For reference, f_{success} decreases from $\gtrsim 75\%$ at $i = 21$, to $\approx 45\%$ at $i = 22.5$, and to $\approx 30\%$ at the limit of our survey, $i \approx 23$ (Cool et al. 2013). We emphasize that the lack of a significant trend of f_{success} with observed-frame color, as well as extensive comparisons of the PRIMUS redshifts with redshifts derived from high-resolution spectroscopic surveys for both intrinsically red and blue (i.e., quiescent and star-forming) galaxies, indicate that the redshift success in PRIMUS is not a strong function of galaxy type.

3.2. Selecting Quiescent and Star-forming Galaxies

A variety of techniques have been proposed to separate passively evolving galaxies from galaxies with ongoing star formation (see, e.g., Williams et al. 2009; Pozzetti et al. 2010), but at a basic level all methods exploit to varying degrees the existence of galaxy bimodality (see Section 1).

Here, we leverage our broad wavelength coverage and precise spectroscopic redshifts (see Section 2) to measure accurate stellar masses and SFRs for the galaxies in our sample using `iSEDfit`, a new Bayesian SED modeling code (see Section 4.1
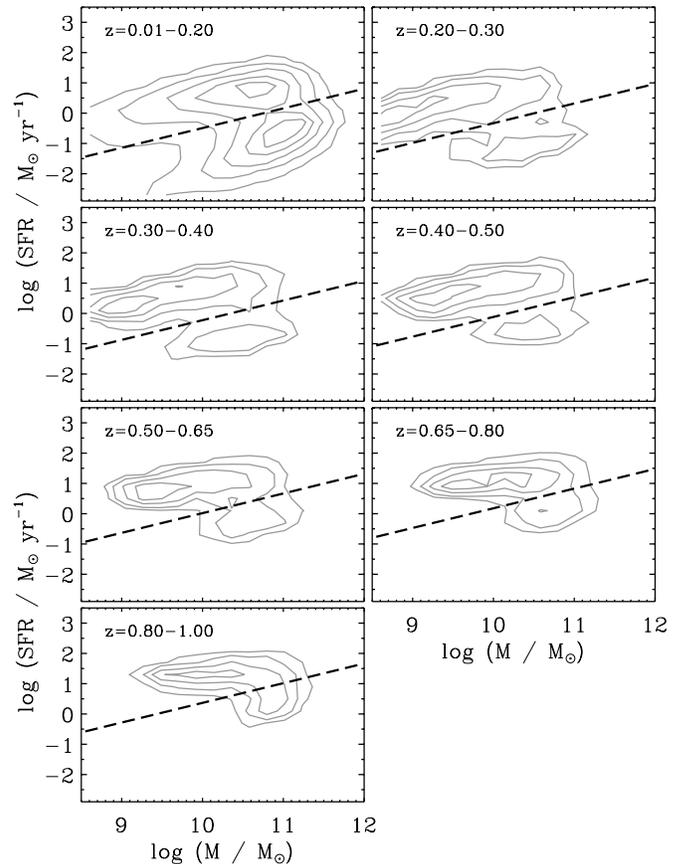
Figure 1. Star formation rate (SFR) vs. stellar mass in seven bins of redshift from $z = 0$–1 based on our SDSS-*GALEX* (upper-left panel) and PRIMUS (subsequent six panels) samples. We divide our sample into star-forming or quiescent according to whether they lie above or below the dashed line, respectively; this line is parallel to the star formation (SF) sequence at $z \approx 0.1$ and evolves with redshift according to Equation (2).

for details). With these quantities in hand, we divide the galaxy population into star-forming and quiescent based on whether they lie on or below the so-called star formation (SF) sequence. The SF sequence (also called the *main sequence* of star formation; Noeske et al. 2007) is the correlation between SFR and stellar mass exhibited by star-forming galaxies at least to $z \sim 2$ (e.g., Oliver et al. 2010; Karim et al. 2011). In Figure 1 we plot SFR versus stellar mass in seven redshift bins from $z = 0$–1 for both our SDSS-*GALEX* and PRIMUS samples. We find a well-defined SF sequence whose amplitude increases smoothly toward higher redshift, and a distinct population of quiescent galaxies that fall below the SF sequence at a given stellar mass (e.g., Salim et al. 2007; Elbaz et al. 2007). We postpone a more detailed discussion of the evolution of the SF sequence to $z = 1$ using PRIMUS to another paper.

To divide the galaxy population we use an evolving cut that traces the lower envelope of the SF sequence in each redshift bin. In detail, we first rotate the SFR versus stellar mass diagram using the power-law slope of the SF sequence derived by Salim et al. (2007); Salim et al. find SFR $\propto \mathcal{M}^{0.65}$ for galaxies at $z \approx 0.1$, which is also a good fit to our SDSS-*GALEX* sample. Next, we construct the histogram distribution of "rotated" SFRs, given by $\log(\text{SFR}_{\text{rot}}) = \log(\text{SFR}) - 0.65(\log \mathcal{M} - 10)$, where SFR is in units of $\mathcal{M}_\odot \, \text{yr}^{-1}$ and $\mathcal{M}$ is in $\mathcal{M}_\odot$, and identify (by eye) the minimum of the bimodality in each redshift bin. Finally, we fit the minimum of the bimodality versus redshift to obtain

the following linear relation:

$$\log{(\mathrm{SFR}_{\min})} = -0.49 + 0.65 \log{(\mathcal{M} - 10)} + 1.07 (z - 0.1). \tag{2}$$

We classify each galaxy in our sample into star-forming and quiescent based on whether its SFR and stellar mass place it above or below the SFR given by Equation (2), interpolated at the redshift of the galaxy.

4. BUILDING THE STELLAR MASS FUNCTION

In this section we describe how we infer the stellar masses and SFRs for the galaxies in our sample (Section 4.1), present the technique we use to construct a non-parametric estimate of the SMF (Section 4.2), and calculate the stellar mass above which our full (hereafter, the *all* sample), quiescent, and star-forming galaxy samples are statistically complete as a function of redshift (Section 4.3).

4.1. Stellar Masses and Star Formation Rates

Modeling the broadband SEDs of galaxies using stellar population synthesis models has become a powerful technique for inferring their physical properties (see the recent review by Walcher et al. 2011, and references therein). We have developed iSEDfit, a suite of routines written in the IDL programming language to determine within a simplified Bayesian framework the stellar masses, SFRs, and other physical properties of galaxies from their observed broadband SEDs (e.g., Kauffmann et al. 2003a; Salim et al. 2007; Auger et al. 2009). We describe iSEDfit in more detail in Appendix A, but in essence the code uses the redshift and observed photometry of each galaxy to compute the statistical likelihood of a large ensemble of model SEDs—generated using population synthesis models—spanning a wide range of observed colors and physical properties (stellar mass, age, metallicity, star formation history, dust content, etc.). Random draws of the model parameters are chosen from user-defined prior parameter distributions using a Monte Carlo technique. Once the posterior probability distribution function (PDF) has been computed, the marginalized PDF of the quantity of interest, such as the stellar mass, follows from the probability-weighted histogram of the corresponding parameter values. The median of the posterior PDF can then be adopted as the best estimate of that parameter, and the uncertainty can be derived from the cumulative distribution function (see Appendix A for more details).

Although SED modeling is conceptually straightforward, the inferred physical properties depend on which population synthesis models and prior parameters are adopted (e.g., Marchesini et al. 2009; Kajisawa et al. 2009; Muzzin et al. 2009). For example, differences in the stellar libraries (e.g., theoretical versus empirical) among population synthesis models, and the exact treatment of post-main sequence stellar evolution can result in widely different predictions of the time- and metallicity-dependent spectral evolution of even simple (i.e., coeval) stellar populations (Conroy et al. 2009; Conroy & Gunn 2010; Mancone & Gonzalez 2012). Moreover, the exact choice of prior parameters (e.g., dust attenuation curve, bursty versus smooth star formation histories, treatment of metallicity evolution, etc.) can also have a significant effect on the derived properties (Kannappan & Gawiser 2007; Pérez-González et al. 2008; Carter et al. 2009; Longhetti & Saracco 2009; Muzzin et al. 2009; Kajisawa et al. 2009; Marchesini et al. 2009; Maraston et al. 2006, 2010; Conroy et al. 2010; Pforr et al. 2012). Finally,

SED modeling typically includes an implicit assumption of a fixed, universal IMF—an IMF that does not vary with redshift or galactic physical conditions. Throughout this paper we make the same simplifying assumption, although recent observations suggest the IMF may not be as universal as once was thought (Davé 2008; Treu et al. 2010; van Dokkum et al. 2010; Cappellari et al. 2012, but see Bastian et al. 2010 for a critical review of the evidence).

An exhaustive investigation of the preceding issues is beyond the scope of the current study. Nevertheless, we would like to have a qualitative and quantitative sense of which of our results are (in)sensitive to the exact choice of population synthesis models and priors. Therefore, we proceed by presenting our principal results in the main body of the paper using a fiducial set of SED modeling assumptions, and in Appendix B we examine the effect of varying these assumptions on our conclusions.

Here, we briefly summarize the default population synthesis models and prior parameters we use, but refer the interested reader to Appendices A and B for additional parameter definitions and details. Our fiducial stellar masses and SFRs are derived using the Flexible Stellar Population Synthesis (FSPS[35]) models (v2.3; Conroy et al. 2009; Conroy & Gunn 2010), based on the Chabrier (2003) IMF from 0.1–100 $\mathcal{M}_{\odot}$. We consider exponentially declining star formation histories with stochastic bursts of varying onset, strength, and duration superposed (Kauffmann et al. 2003a; Salim et al. 2007), and allow a wide range of galaxy ages and possible star formation histories. Finally, we assume sensibly distributed priors on stellar metallicity and dust attenuation, and adopt the time-dependent attenuation curve of Charlot & Fall (2000).

The photometric bands we use vary with the sample. In our SDSS-*GALEX* sample we fit to 12 bands of photometry: FUV and NUV from *GALEX*; *ugriz* from the SDSS; *JHK$_s$* from 2MASS; and the 3.4 and 4.6 μm bands from *WISE* (see Section 2.4). In our PRIMUS sample we fit to our *GALEX* FUV and NUV photometry (see Section 2.2), the two shortest IRAC bands at 3.6 and 4.5 μm, and five optical bands, except in COSMOS where we fit to seven optical and near-infrared bands (see Section 2.3). We do not fit to the two longer-wavelength IRAC channels at 5.8 and 8 μm because of the potential contributions from hot dust and polycyclic aromatic hydrocarbon (PAH) emission lines at these wavelengths (e.g., Smith et al. 2007), which iSEDfit does not currently model. When fitting, we assume minimum photometric uncertainties of 5.2% and 2.6% in the FUV and NUV, respectively (Morrissey et al. 2007), 2%–5% in the optical/near-infrared bands, and 3% in the 2MASS and *WISE* near- and mid-infrared photometric bands.

4.2. A Non-parametric Estimate of the Stellar Mass Function

We build the SMF using the non-parametric $1/V_{\max}$ estimator widely used in analyses of the galaxy luminosity function (see the recent review by Johnston 2011, and references therein). We use this technique in favor of complementary *parametric* methods because accurately fitting the observed SMF at $z = 0$–1 requires additional free parameters at the low-mass end (Baldry et al. 2008; Drory et al. 2009; Peng et al. 2010), which cannot be reliably constrained at higher redshift with PRIMUS. Nevertheless, when calculating number and stellar mass densities, we do rely on either a single standard Schechter (1976) function, or a *double* Schechter function (see, e.g., Baldry

---

[35] http://www.ucolick.org/~cconroy/FSPS.html

et al. 2008), depending on which model is a better fit to the data, to extrapolate the observed binned SMF over small intervals of stellar mass as needed. We will also occasionally refer to the "knee" of the SMF as $\mathcal{M}^*$, which marks the stellar mass above which the SMF declines exponentially.

The differential, non-parametric SMF is given by

$$\Phi(\log \mathcal{M}) \, \Delta(\log \mathcal{M}) = \sum_{i=1}^{N} \frac{w_i}{V_{\mathrm{max,i}}}, \qquad (3)$$

where V_{max} is the maximum cosmological volume within which each galaxy i could have been observed given the apparent magnitude limits of the survey, w_i is the statistical weight for each object (see Section 3.1), $\Phi(\log \mathcal{M}) \times \Delta(\log \mathcal{M})$ is the number of galaxies (N) per unit volume with stellar masses in the range $\log \mathcal{M} \to \log \mathcal{M} + \Delta(\log \mathcal{M})$, and $\mathcal{M}$ has units of $\mathcal{M}_\odot$.

To estimate V_{max} for each galaxy we first use K-correct[36] (v4.2; Blanton & Roweis 2007) to derive the redshift-dependent K-correction, $K(z)$, from the observed SED. We use K-correct because of its speed and convenience, although we obtain similar results if we instead use the best-fitting iSEDfit model (Section 4.1). Next, we write the apparent magnitude, m, of a galaxy of absolute magnitude M as

$$m = M + \mathrm{DM} + K - Qz, \qquad (4)$$

where $\mathrm{DM}(z)$ is the distance modulus (Hogg 1999) and Q is a (constant) luminosity evolution term which we discuss below. Given the observed apparent magnitude, m_{obj}, of an object at redshift z_{obj}, we can use Equation (4) to write $\Delta m(z)$, the change in the apparent magnitude of the object as a function of redshift, as

$$\Delta m(z) \equiv m_{\mathrm{obj}} - m(z) = \mathrm{DM}(z_{\mathrm{obj}}) - \mathrm{DM}(z)$$
$$+ K(z_{\mathrm{obj}}) - K(z) - Q(z_{\mathrm{obj}} - z). \qquad (5)$$

By definition, z_{max} (z_{min}) is the redshift at which Δm equals the faint (bright) apparent magnitude limit of the survey. Once z_{max} and z_{min} have been computed for each galaxy with a measured redshift in the interval $[z_{\mathrm{lower}}, z_{\mathrm{upper}}]$, V_{max} can be computed using

$$V_{\mathrm{max}} = \int_\Omega \int_{z_1}^{z_2} \frac{d^2 V_c}{dz \, d\Omega} \, dz \, d\Omega, \qquad (6)$$

where $z_1 = \mathtt{max}\,(z_{\mathrm{min}}, z_{\mathrm{lower}})$, $z_2 = \mathtt{min}\,(z_{\mathrm{max}}, z_{\mathrm{upper}})$, Ω is the solid angle of the survey, and V_c is the comoving volume (Hogg 1999).

The coefficient Q in Equations (4) and (5) allows us to include a simple luminosity evolution model into our V_{max} estimates. Many recent measurements of the optical luminosity function have shown that galaxies brighten toward higher redshift (e.g., Blanton et al. 2003b; Faber et al. 2007; Loveday et al. 2012; Cool et al. 2012); consequently, higher-redshift galaxies will be observable over a larger cosmological volume (i.e., V_{max} will be larger) relative to the no-evolution case. Using $Q > 0$ in Equation (5) allows us to mimic the observed luminosity evolution, at least in a statistical sense.

Of course, our luminosity evolution model is intentionally simplistic and should not be over-interpreted. For example, Blanton et al. (2003b) find that among $z \approx 0.1$ galaxies Q varies by roughly a factor of two at rest-frame optical wavelengths redward of the 4000 Å break, whereas our simple model

assumes that Q is independent of wavelength. Nevertheless, the distribution of V_c/V_{max} for our SDSS-GALEX sample clearly shows the need to account for luminosity evolution when estimating V_{max}. For example, without luminosity evolution (i.e., $Q = 0$), V_c/V_{max} for our SDSS-GALEX sample correlates with redshift, stellar mass, and other intrinsic galaxy properties; adopting $Q = 1$–2 mag z^{-1}, on the other hand, removes these first-order dependencies and results in $\langle V_c/V_{\mathrm{max}} \rangle \approx 0.5$, as expected for a homogenous, statistically complete sample (Johnston 2011). The distribution of V_c/V_{max} for PRIMUS, on the other hand, is largely insensitive to Q because of the fairly narrow redshift bins we adopt (see, e.g., Figure 1). Using $Q > 0$ in place of $Q = 0$ changes V_{max} for just $\approx 10\%$ of PRIMUS galaxies in each redshift interval, and has no significant effect on our derived SMFs.

With the preceding discussion in mind, we calculate V_{max} for each galaxy using Equation (6) and the solid angle and optical apparent magnitude limits listed in Table 1. We adopt $Q = 1.6$ mag z^{-1} (Blanton et al. 2003b; Cool et al. 2012) when calculating V_{max} based on our optical magnitude limits; in the CDFS and ELAIS-S1 fields we separately estimate V_{max} based on our 3.6 μm flux limits assuming $Q = 1.2$ mag z^{-1} (Dai et al. 2009), and adopt the *smaller* of the two (optical versus mid-infrared) V_{max} values.

Neglecting stellar mass uncertainties (see Appendix B), the two principal sources of uncertainty in the SMF are due to sample size (i.e., Poisson uncertainty) and sample variance. In the limit $N \gg 1$, the formal Poisson uncertainty is given by

$$\sigma_\Phi = \frac{1}{\Delta(\log \mathcal{M})} \sqrt{\sum_{i=1}^{N} \frac{w_i}{V_{\mathrm{max},i}^2}}. \qquad (7)$$

Equation (7) becomes increasingly inaccurate, however, as the number of galaxies approaches zero; therefore, we calculate the effective number of galaxies in each mass bin following Zhu et al. (2009), and use the analytic formulae of Gehrels (1986) to compute the upper and lower statistical uncertainty of the SMF.

To estimate the uncertainty in the SMF due to sample variance we use a standard jackknife technique. We construct the SMF excluding one field at a time, and calculate the uncertainty in the mean number of galaxies in each stellar mass bin due to the field-to-field variations. Formally, we estimate the uncertainty, σ_{cv}^j, in the jth stellar mass bin due to sample variance as

$$\sigma_{\mathrm{cv}}^j = \sqrt{\frac{M-1}{M} \sum_{k=1}^{M} \left(\Phi_k^j - \langle \Phi^j \rangle \right)^2}, \qquad (8)$$

where the sum extends over all M individual fields, and $\langle \Phi^j \rangle$ is the mean number density of galaxies in that stellar mass bin measured from all the available data. Note that when computing the cumulative number and stellar mass densities (see Section 5.2), we integrate each jackknife realization of the SMF, and compute the variance in these quantities using the same formalism.

This jackknife technique likely underestimates the level of sample variance in PRIMUS, because two of the five fields (XMM-SXDS and XMM-CFHTLS) are spatially adjacent, so there is covariance between the fields due to structure on scales larger than the combined field. For simplicity, however, we ignore this covariance in our analysis, and simply exclude each of the $M = 5$ fields sequentially as if they were independent.

---

[36] http://howdy.physics.nyu.edu/index.php/Kcorrect

Another potential issue is that the individual fields are not the same size (angular area); therefore, one might expect that the standard jackknife prefactor $\sqrt{(M-1)/M}$ is not strictly correct. However, we verified using a Monte Carlo calculation that the correct prefactor for our sample differs by $<5\%$ from the nominal value despite the more than factor of two variation in solid angle among our five fields (see Table 1).

Finally, to estimate the level of sample variance in our SDSS-*GALEX* sample, we divide the sky into a 12×9 rectangular grid, and retain the 27 $30 \times 60 \, \mathrm{deg}^2$ regions containing at least 1000 galaxies. We then compute the variance in the SDSS-*GALEX* SMF using the same methodology described above, once again ignoring the potential covariance between adjacent subfields.

4.3. Stellar Mass Completeness Limits

Before computing the SMF we need to determine the stellar mass above which our sample is complete. In a magnitude-limited survey such as PRIMUS, the stellar mass completeness limit is a function of redshift, the apparent magnitude limit of the survey, and the typical stellar mass-to-light ratio of galaxies near this flux limit. For example, a quiescent galaxy of a given stellar mass will preferentially fall below the survey flux limit compared to a star-forming galaxy with the same stellar mass, because the stellar mass-to-light ratios of quiescent galaxies are typically higher.

We empirically determine the stellar mass completeness limits of our sample following Pozzetti et al. (2010). First, we compute $\mathcal{M}_{\mathrm{lim}}$, the stellar mass each galaxy would have if its apparent magnitude was equal to the survey magnitude limit, $\log \mathcal{M}_{\mathrm{lim}} = \log \mathcal{M} + 0.4 \, (m - m_{\mathrm{lim}})$, where $\mathcal{M}$ is the stellar mass of the galaxy in units of $\mathcal{M}_{\odot}$, m is the observed apparent magnitude in the selection band, and m_{lim} is the corresponding magnitude limit (see Table 1). Next, we construct the cumulative distribution of $\mathcal{M}_{\mathrm{lim}}$ for the 15% faintest galaxies in $\Delta z = 0.04$ wide bins of redshift, and calculate the minimum stellar mass that includes 95% of the objects. We use the subset of galaxies near the flux limit to account for the fact that in a flux-limited sample the lowest-luminosity galaxies tend to have the lowest stellar mass-to-light ratios; however, we did verify that using the whole sample in each redshift slice changes the derived mass limits by $\lesssim 0.1$ dex. Finally, we fit the limiting stellar mass versus redshift with a quadratic polynomial separately for all, star-forming, and quiescent galaxies. We evaluate this fit at the center of each of our six adopted redshift intervals (see Figure 1), and list the results in Table 2.

In the CDFS and ELAIS-S1 fields we carry out the same procedure described above except we consider the flux limits in both the i' and R selection bands, respectively, and in the IRAC $3.6 \, \mu\mathrm{m}$ band (see Section 3.1 and Table 1). At each redshift we then take the greater of the two stellar mass limits implied by the two apparent magnitude limits. In detail, in these fields our sample is limited by the $3.6 \, \mu\mathrm{m}$ flux limit at low redshift, and by the optical flux limit at higher redshift, with the transition redshift occurring around $z \approx 0.6$.

Figure 2 plots stellar mass versus redshift for the galaxies in all five PRIMUS fields. The black squares, red diamonds, and blue points indicate the stellar mass completeness limits at the center of each redshift bin for all, quiescent, and star-forming galaxies, respectively, and the solid black, dot-dashed red, and dashed blue lines show the corresponding polynomial fits. As expected, the completeness limits for the quiescent galaxies lie above the star-forming galaxy limits at all redshifts, except in our

Table 2
Stellar Mass Completeness Limits[a]

Redshift Range	COSMOS	XMM-SXDS	XMM-CFHTLS	CDFS	ELAIS-S1
	$\log (\mathcal{M}_{\mathrm{lim}}/\mathcal{M}_{\odot})$				
All					
0.20–0.30	8.73	8.86	8.95	9.62	9.70
0.30–0.40	9.14	9.23	9.23	9.87	9.99
0.40–0.50	9.51	9.58	9.51	10.10	10.26
0.50–0.65	9.92	9.97	9.87	10.37	10.56
0.65–0.80	10.33	10.38	10.31	10.65	10.87
0.80–1.00	10.71	10.78	10.83	10.94	11.17
Star-forming					
0.20–0.30	8.68	8.79	8.80	9.60	9.58
0.30–0.40	9.05	9.13	9.06	9.92	9.94
0.40–0.50	9.38	9.44	9.30	10.19	10.25
0.50–0.65	9.75	9.77	9.58	10.44	10.59
0.65–0.80	10.12	10.10	9.89	10.63	10.90
0.80–1.00	10.46	10.38	10.21	10.69	11.14
Quiescent					
0.20–0.30	9.23	9.35	9.17	9.65	9.80
0.30–0.40	9.58	9.61	9.52	9.92	10.06
0.40–0.50	9.89	9.85	9.85	10.17	10.30
0.50–0.65	10.22	10.13	10.22	10.44	10.55
0.65–0.80	10.52	10.43	10.60	10.71	10.79
0.80–1.00	10.75	10.73	10.96	10.96	10.99

Notes. [a] Stellar mass completeness limits among all, quiescent, and star-forming galaxies as a function of redshift. Above these limits our sample includes more than 95% of all types of galaxies, accounting for the flux limit in each field and mass-to-light ratio variations. For comparison, in our SDSS-*GALEX* sample the completeness limit is $10^9 \, \mathcal{M}_{\odot}$ for all three samples.

CDFS and ELAIS-S1 fields, which are flux-limited in both the optical and at $3.6 \, \mu\mathrm{m}$. Moreover, the completeness limits for all galaxies overlap the star-forming galaxy limits at low redshift, and the quiescent galaxy limits at high redshift. This shift occurs because at low redshift the combined sample is dominated by low-mass star-forming galaxies, while at high redshift massive, quiescent galaxies dominate, as we demonstrate in the next section.

Finally, for our SDSS-*GALEX* sample we adopt a uniform stellar mass limit of $10^9 \, \mathcal{M}_{\odot}$, which is safely above the surface brightness and stellar mass-to-light ratio completeness limits of the survey (Blanton et al. 2005a; Baldry et al. 2008).

5. EVOLUTION OF THE STELLAR MASS FUNCTION FROM $z = 0$–1

We now have all the ingredients needed to compute the evolution of the SMF from $z = 0$–1. We begin in Section 5.1 by presenting the SMF at $z \approx 0.1$ using our SDSS-*GALEX* sample. Next, we combine the SDSS-*GALEX* and PRIMUS samples in Section 5.2 and show how the SMF of all, quiescent, and star-forming galaxies has evolved since $z = 1$. The results we present in this section are all based on our fiducial stellar mass estimates (see Section 4.1), although in Appendix B we present a detailed discussion of how systematic uncertainties in our stellar mass estimates affect our conclusions.
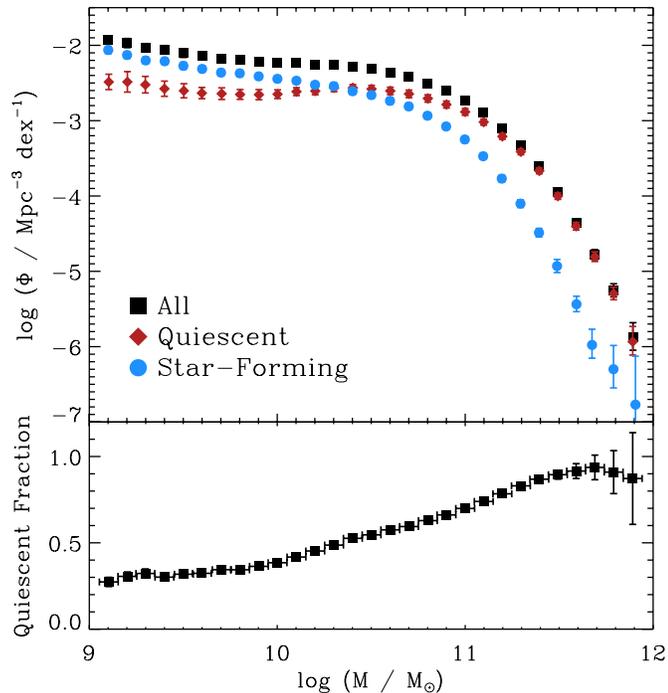
5.1. Stellar Mass Function at $z \approx 0.1$

We begin by presenting in the upper panel of Figure 3 the SMF at $z \approx 0.1$ based on the entire SDSS-*GALEX* sample
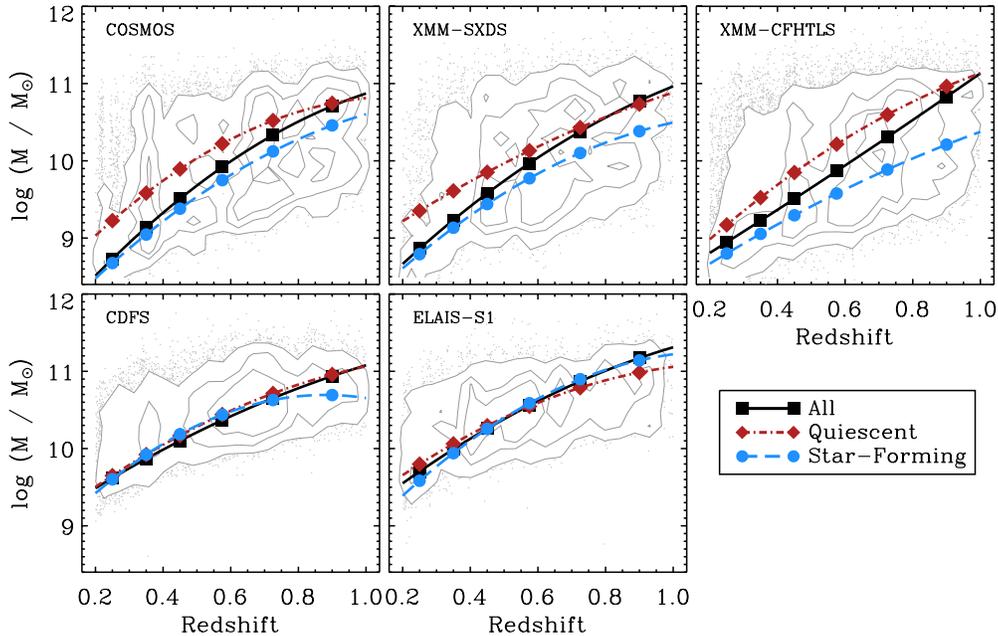
Figure 2. Stellar mass vs. redshift for all galaxies in the five individual PRIMUS fields. The contours enclose 30%, 60%, and 90% of the sample, while the gray points show galaxies lying outside the 90% quantile. The solid black, dot-dashed red, and dashed blue lines indicate the stellar mass completeness limit in each field, and the black squares, red diamonds, and blue points show the stellar mass limit at the center of each of our six adopted redshift bins (see Table 2). In the CDFS and ELAIS-S1 fields the stellar mass limits among all, quiescent, and star-forming galaxies are comparable at all redshifts because these two samples are limited in both the optical and at 3.6 μm (see Section 3.1). Meanwhile, in the COSMOS, XMM-SXDS, and XMM-CFHTLS fields we find that the stellar mass limit for quiescent (star-forming) galaxies is higher (lower) at all redshifts, as expected given their typically larger (lower) stellar mass-to-light ratios. Moreover, the stellar mass limit for the *all* sample tracks low-mass star-forming galaxies at low redshift, and massive quiescent galaxies at high redshift.

(A color version of this figure is available in the online journal.)

Figure 3. Upper panel: SDSS-*GALEX* SMF for all (black squares), quiescent (red diamonds), and star-forming (blue points) galaxies at $z \approx 0.1$. Lower panel: fraction of quiescent galaxies as a function of stellar mass. The massive end of the SMF is overwhelmingly comprised of quiescent galaxies, while below $\mathcal{M} \sim 3 \times 10^{10} \, \mathcal{M}_\odot$ star-forming galaxies increasingly dominate the global galaxy population. Quantitatively, the fraction of quiescent galaxies ranges from ~25% around ~3 × $10^9 \, \mathcal{M}_\odot$ to ~95% around ~3 × $10^{11} \, \mathcal{M}_\odot$.

(A color version of this figure is available in the online journal.)

(black squares), and separately for the star-forming (blue points) and quiescent (red diamonds) galaxy subsamples. Each point represents the comoving number density of galaxies in 0.1 dex wide bins of stellar mass, and the vertical error bars indicate the quadrature sum of the Poisson and sample variance uncertainties in each stellar mass bin. We tabulate the SMF for each sample in Table 3. The lower panel of this figure shows the variation in the fraction of quiescent galaxies with stellar mass.

Figure 3 conveys several striking (albeit well-known) results. First, the massive end of the SMF is almost entirely comprised of quiescent galaxies, while star-forming galaxies vastly outnumber quiescent galaxies at the low-mass end (see, e.g., Blanton & Moustakas 2009, and references therein). Above ~$2 \times 10^{11} \, \mathcal{M}_\odot$ more than ~90% of galaxies are quiescent, whereas below ~$10^{10} \, \mathcal{M}_\odot$ star-forming galaxies outnumber quiescent galaxies by more than a factor of three. The stellar mass at which each population begins to outnumber the other is $\mathcal{M} \sim 3 \times 10^{10} \, \mathcal{M}_\odot$, in good agreement with previous studies (e.g., Bell et al. 2003; Kauffmann et al. 2003b; Baldry et al. 2004). Integrating the observed distributions above $\mathcal{M} = 10^9 \, \mathcal{M}_\odot$ yields a total stellar mass density of $2.36 \times 10^8 \, \mathcal{M}_\odot \, \mathrm{Mpc}^{-3}$, of which approximately 60% resides in quiescent galaxies.[37] For comparison, Baldry et al. (2004) find that 54%–60% of the stellar mass density at $z \approx 0.1$ is in red, early-type galaxies, where the precise result depends on the method used to derive stellar masses.

We compare our results to previously published measurements of the local SMF in Figure 4, adjusting where necessary for differences in the adopted IMF and cosmological parameters. We plot the SDSS-*GALEX* SMF using filled black

---

[37] Note that galaxies with $\mathcal{M} < 10^9 \, \mathcal{M}_\odot$ contribute a negligible amount to the overall stellar mass budget of the nearby universe (see also Brinchmann et al. 2004).

Table 3
SDSS-*GALEX* Stellar Mass Function

$\log(\mathcal{M})$ $(h_{70}^{-2}\,\mathcal{M}_\odot)$	All			Star-forming			Quiescent		
	$\log(\Phi)$ $(h_{70}^3\,\mathrm{Mpc}^{-3}\,\mathrm{dex}^{-1})$	σ_{SV}	N	$\log(\Phi)$ $(h_{70}^3\,\mathrm{Mpc}^{-3}\,\mathrm{dex}^{-1})$	σ_{SV}	N	$\log(\Phi)$ $(h_{70}^3\,\mathrm{Mpc}^{-3}\,\mathrm{dex}^{-1})$	σ_{SV}	N
9.0	$-1.899^{+0.017}_{-0.017}$	0.052	1040	$-2.026^{+0.018}_{-0.017}$	0.043	854	$-2.495^{+0.048}_{-0.043}$	0.096	186
9.1	$-1.923^{+0.017}_{-0.016}$	0.048	1239	$-2.062^{+0.017}_{-0.016}$	0.045	1030	$-2.486^{+0.044}_{-0.041}$	0.093	209
9.2	$-1.970^{+0.015}_{-0.015}$	0.059	1397	$-2.129^{+0.015}_{-0.014}$	0.041	1162	$-2.485^{+0.038}_{-0.035}$	0.10	235
9.3	$-2.031^{+0.015}_{-0.014}$	0.052	1594	$-2.201^{+0.014}_{-0.014}$	0.044	1328	$-2.523^{+0.037}_{-0.034}$	0.10	266
9.4	$-2.055^{+0.014}_{-0.013}$	0.050	1874	$-2.211^{+0.014}_{-0.013}$	0.040	1594	$-2.576^{+0.033}_{-0.031}$	0.096	280
9.5	$-2.106^{+0.012}_{-0.012}$	0.053	2106	$-2.272^{+0.012}_{-0.012}$	0.044	1790	$-2.603^{+0.030}_{-0.028}$	0.090	316
9.6	$-2.144^{+0.012}_{-0.011}$	0.046	2465	$-2.313^{+0.012}_{-0.012}$	0.040	2079	$-2.634^{+0.026}_{-0.025}$	0.070	386
9.7	$-2.179^{+0.012}_{-0.012}$	0.051	2820	$-2.362^{+0.011}_{-0.011}$	0.043	2385	$-2.642^{+0.028}_{-0.026}$	0.072	435
9.8	$-2.188^{+0.010}_{-0.010}$	0.046	3434	$-2.371^{+0.011}_{-0.011}$	0.040	2886	$-2.652^{+0.021}_{-0.020}$	0.062	548
9.9	$-2.2160^{+0.0086}_{-0.0084}$	0.048	3971	$-2.4120^{+0.0092}_{-0.0090}$	0.039	3255	$-2.655^{+0.018}_{-0.017}$	0.065	716
10.0	$-2.2340^{+0.0080}_{-0.0078}$	0.047	4667	$-2.4450^{+0.0090}_{-0.0088}$	0.041	3710	$-2.649^{+0.015}_{-0.015}$	0.056	957
10.1	$-2.2350^{+0.0069}_{-0.0068}$	0.045	5631	$-2.4700^{+0.0074}_{-0.0078}$	0.040	4247	$-2.614^{+0.013}_{-0.012}$	0.051	1384
10.2	$-2.2620^{+0.0063}_{-0.0062}$	0.046	6601	$-2.5240^{+0.0074}_{-0.0072}$	0.041	4746	$-2.607^{+0.011}_{-0.011}$	0.048	1855
10.3	$-2.2520^{+0.0056}_{-0.0056}$	0.049	8096	$-2.5410^{+0.0071}_{-0.0070}$	0.042	5423	$-2.5640^{+0.0089}_{-0.0087}$	0.050	2673
10.4	$-2.2850^{+0.0051}_{-0.0051}$	0.045	9341	$-2.6090^{+0.0066}_{-0.0065}$	0.042	5831	$-2.5640^{+0.0077}_{-0.0076}$	0.043	3510
10.5	$-2.3170^{+0.0047}_{-0.0046}$	0.046	10901	$-2.6600^{+0.0063}_{-0.0062}$	0.041	6441	$-2.5800^{+0.0069}_{-0.0068}$	0.047	4460
10.6	$-2.3650^{+0.0044}_{-0.0044}$	0.049	12177	$-2.7370^{+0.0062}_{-0.0061}$	0.043	6706	$-2.6050^{+0.0062}_{-0.0061}$	0.049	5471
10.7	$-2.4190^{+0.0041}_{-0.0041}$	0.049	13594	$-2.8110^{+0.0059}_{-0.0059}$	0.044	7001	$-2.6450^{+0.0057}_{-0.0056}$	0.050	6593
10.8	$-2.5040^{+0.0040}_{-0.0040}$	0.047	14172	$-2.9340^{+0.0061}_{-0.0060}$	0.040	6580	$-2.7050^{+0.0053}_{-0.0052}$	0.049	7592
10.9	$-2.6070^{+0.0039}_{-0.0039}$	0.046	14148	$-3.0770^{+0.0064}_{-0.0063}$	0.041	5829	$-2.7860^{+0.0050}_{-0.0050}$	0.046	8319
11.0	$-2.7280^{+0.0040}_{-0.0040}$	0.046	13361	$-3.2500^{+0.0071}_{-0.0070}$	0.043	4715	$-2.8840^{+0.0049}_{-0.0049}$	0.045	8646
11.1	$-2.8880^{+0.0043}_{-0.0043}$	0.043	11592	$-3.4720^{+0.0085}_{-0.0084}$	0.041	3306	$-3.0190^{+0.0050}_{-0.0050}$	0.041	8286
11.2	$-3.1040^{+0.0049}_{-0.0048}$	0.041	8682	$-3.769^{+0.011}_{-0.010}$	0.044	1918	$-3.2090^{+0.0055}_{-0.0054}$	0.038	6764
11.3	$-3.3320^{+0.0059}_{-0.0059}$	0.042	5717	$-4.102^{+0.016}_{-0.015}$	0.049	936	$-3.4130^{+0.0065}_{-0.0064}$	0.038	4781
11.4	$-3.6060^{+0.024}_{-0.0079}$	0.042	3119	$-4.487^{+0.024}_{-0.023}$	0.052	391	$-3.6670^{+0.0085}_{-0.0084}$	0.037	2728
11.5	$-3.953^{+0.012}_{-0.012}$	0.047	1398	$-4.930^{+0.042}_{-0.038}$	0.077	140	$-4.002^{+0.013}_{-0.012}$	0.041	1258
11.6	$-4.363^{+0.020}_{-0.019}$	0.050	535	$-5.437^{+0.079}_{-0.067}$	0.072	43	$-4.401^{+0.021}_{-0.020}$	0.046	492
11.7	$-4.778^{+0.033}_{-0.031}$	0.057	201	$-5.98^{+0.20}_{-0.10}$	0.10	12	$-4.806^{+0.034}_{-0.032}$	0.055	189
11.8	$-5.255^{+0.060}_{-0.053}$	0.066	67	$-6.30^{+0.30}_{-0.20}$	0.20	6	$-5.296^{+0.063}_{-0.056}$	0.059	61
11.9	$-5.87^{+0.10}_{-0.10}$	0.10	16	$-6.77^{+0.60}_{-0.30}$	0.30	2	$-5.93^{+0.10}_{-0.10}$	0.10	14
12.0	$-6.49^{+0.30}_{-0.20}$	0.20	4	$-7.09^{+1.00}_{-0.40}$	0.40	1	$-6.61^{+0.40}_{-0.20}$	0.30	3

squares, and the results from Cole et al. (2001), Bell et al. (2003), Li & White (2009), and Baldry et al. (2012) using orange diamonds, red circles, green triangles, and blue squares, respectively. Overall, our results agree reasonably well with these studies, although there are some notable differences. The agreement between our SMF and the recent measurement by Baldry et al. (2012), who analyzed a sample of $\sim10^5$ galaxies at $z < 0.06$ over 143 deg^2 with spectroscopic redshifts from the SDSS and GAMA (Driver et al. 2011) surveys, is especially good. Unfortunately, the Baldry et al. (2012) sample included too few galaxies with stellar masses $\mathcal{M} \gtrsim 3 \times 10^{11}\,\mathcal{M}_\odot$ for them to reliably measure the massive end of the SMF.

Compared to Li & White (2009), the exponential tail of our SMF falls off less steeply, which is somewhat surprising given that they analyzed a comparably large sample of SDSS galaxies. However, Bernardi et al. (2010) argue that Li & White likely underestimated the stellar masses of the most massive galaxies in their sample for two reasons: first, Li & White used Petrosian magnitudes, which are known to underestimate the fluxes of galaxies with extended surface brightness profiles such as the spheroidal galaxies that dominate the massive end of the

SMF (see also Blanton et al. 2011); and second, Li & White derived stellar masses using the standard set of K-correct basis templates (Blanton & Roweis 2007), which can underestimate the stellar masses of massive early-type galaxies dominated by very old stellar populations (see Bernardi et al. 2010 and Appendix B).

Finally, Figure 4 shows that the SMF measured by Bell et al. (2003) lies systematically above our SMF at all stellar masses. Bell et al. constructed their SMF from a sample of ~7000 galaxies distributed over ~400 deg^2 in the SDSS Early Data Release (EDR) survey area (Stoughton et al. 2002). However, this area of the sky is now known to contain one of the largest structures ever mapped, the SDSS Great Wall at $z = 0.078$ (Gott et al. 2005). Therefore, one possibility for the origin of the discrepancy is that the Bell et al. SMF may be more affected by large-scale structure (i.e., sample variance) than originally estimated. Alternatively, a strong color-dependent difference in stellar mass-to-light ratio that is negligible for massive quiescent galaxies and ~0.3 dex (factor of ~2) for low-mass star-forming galaxies could also explain the observed discrepancy (E. F. Bell 2012, private communication). Whatever the reason, a practical
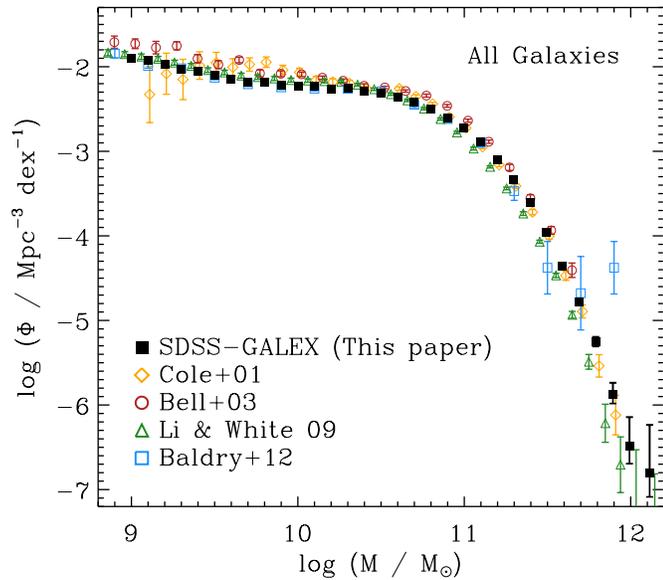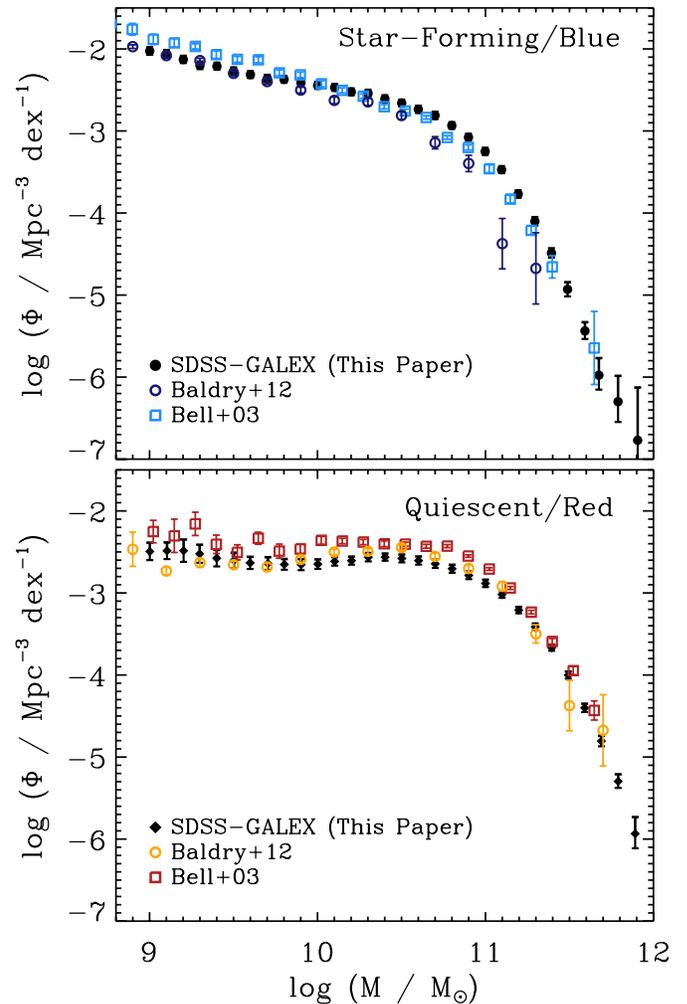
Figure 4. Comparison of our measurement of the SMF at $z \approx 0.1$ for all galaxies against previous determinations from the literature, adjusted to our adopted cosmology and IMF where necessary. Overall, our results agree well with these previous studies, albeit with some notable differences (see Section 5.1).

(A color version of this figure is available in the online journal.)

Figure 5. Comparison of the SDSS-*GALEX* SMF of star-forming (top) and quiescent (bottom) galaxies against the SMFs of optically-selected blue-cloud and red-sequence galaxies from Bell et al. (2003) and Baldry et al. (2012), respectively. We verified that when we divide the galaxy population using the $u - r$ vs. M_r color-magnitude diagram we obtain excellent agreement with the corresponding SMFs from Baldry et al. Therefore, we attribute the apparent differences between the SMFs to contamination of the red sequence by dusty star-forming galaxies.

(A color version of this figure is available in the online journal.)

consequence of this result is that previous studies which relied on the Bell et al. SMF, and to a lesser degree the Cole et al. SMF as their low-redshift anchor, may have overestimated the amount of number and stellar mass density evolution (e.g., Brammer et al. 2011; Mortlock et al. 2011).

Next, we compare our SMFs of quiescent and star-forming galaxies against previous measurements. Most previous analyses have used the optical color-magnitude diagram to identify "quiescent" and "star-forming" galaxies according to whether they lie on the *red sequence* or the *blue cloud* (e.g., Bell et al. 2003; Taylor et al. 2009; Baldry et al. 2012); however, the optical red sequence is known to contain both bona fide quiescent galaxies and dust-obscured star-forming galaxies (e.g., Brand et al. 2009; Maller et al. 2009; Zhu et al. 2011). By contrast, we identify quiescent and star-forming galaxies according to whether they lie on or below the star-forming sequence, which allows us to select a purer sample of quiescent galaxies (Salim et al. 2007; Schiminovich et al. 2007). Therefore, we anticipate that the overall normalization of our quiescent-galaxy SMF will be lower relative to these previous studies. Moreover, the differences are likely to be stellar mass-dependent because the level of star formation activity and amount of dust attenuation vary systematically with stellar mass (Brinchmann et al. 2004; Elbaz et al. 2007; Garn & Best 2010).

With the preceding ideas in mind, in Figure 5 we compare our SMFs for star-forming and quiescent galaxies against the SMFs published by Bell et al. (2003) and Baldry et al. (2012). Bell et al. used the $g - r$ color-magnitude diagram to identify red-sequence and blue-cloud galaxies, while Baldry et al. leveraged the bimodality in $u - r$ color. As expected, our SMF of quiescent galaxies agrees reasonably well with the SMFs from Bell et al. and Baldry et al. at the massive end, where the amount of contamination from dusty starburst galaxies is minimal, but is displaced systematically below their SMFs below $\sim 10^{11} \mathcal{M}_{\odot}$. As anticipated above, the reason for these differences is likely because the $g - r$ and $u - r$ red sequences at intermediate mass contain an admixture of both quiescent and dust-obscured star-

forming galaxies. In our analysis, these galaxies are (correctly) assigned to the star-forming galaxy SMF, as illustrated in the upper panel of Figure 5. We verified this interpretation by constructing the SMFs for red-sequence and blue-cloud galaxies in our SDSS-*GALEX* sample using the same $u - r$ versus M_r optical color-magnitude diagram as Baldry et al., and found outstanding agreement.

5.2. Evolution of the Stellar Mass Function since $z \approx 1$

In the previous section we established the SMF at $z \approx 0.1$ using our SDSS-*GALEX* sample. Here, we measure how the stellar mass distribution of all, quiescent, and star-forming galaxies has changed since $z \approx 1$.

5.2.1. All Galaxies

We begin by comparing the SMFs in the five individual PRIMUS fields. In Figure 6 we plot the SMFs in 0.15 dex wide bins of stellar mass divided into six redshift bins from $z = 0.2$–1.0 centered on $\langle z \rangle = 0.25, 0.35, 0.45, 0.575, 0.725,$
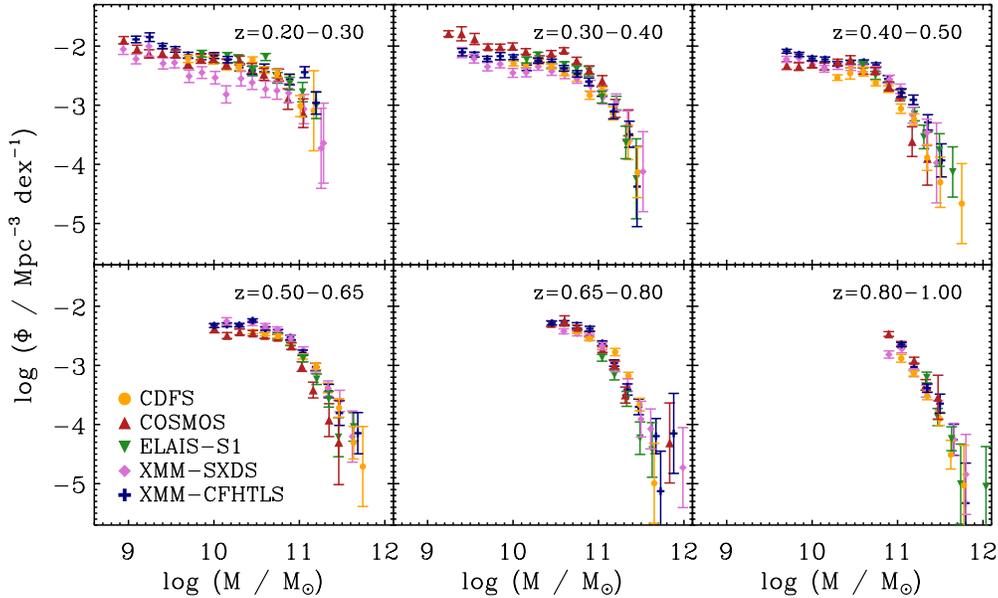
Figure 6. Comparison of the SMFs in each of the five individual PRIMUS fields in six redshift bins from $z = 0.2$–1.0. The error bars reflect the statistical (Poisson) uncertainty in each stellar mass bin, and for clarity we only show the SMF in each field above our stellar mass completeness limit (see Section 4.3). This comparison demonstrates the overall consistency of the SMFs across the five fields, modulo expected differences due to sample variance.

(A color version of this figure is available in the online journal.)
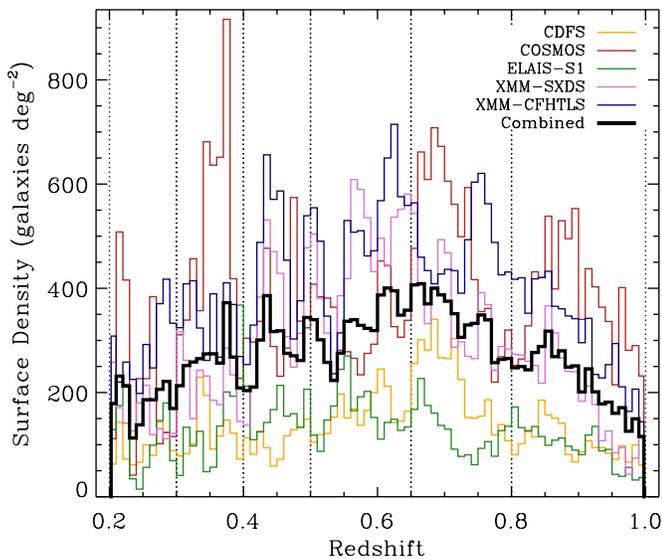
Figure 7. Projected surface density of galaxies vs. redshift in the five individual PRIMUS fields as indicated in the legend, and for the combined sample (thick black histogram). The vertical dotted lines indicate the boundaries of the six redshift bins we have adopted. The variation in the number density of galaxies in each field and redshift interval bin due to large-scale structure (sample variance) is striking. The largest overdensities are in the COSMOS field at $z \approx 0.35$, ≈ 0.7, and ≈ 0.85; in the XMM-CFHTLS field at $z \approx 0.45$, ≈ 0.6, and ≈ 0.75; and in our CDFS field at $z \approx 0.7$. Note that the overall surface density in our CDFS and ELAIS-S1 fields is lower at all redshifts because of the additional 3.6 μm flux limit imposed in these fields (see Section 3.1).

(A color version of this figure is available in the online journal.)

and 0.9. We choose these redshift bins because they correspond to roughly equal ~ 0.9 Gyr intervals of cosmic time. For clarity we only plot the portion of each SMF above our stellar mass completeness limit in each field (see Section 4.3).

We find good overall agreement among the individual SMFs, modulo expected deviations due to sample variance. In Figure 7 we illustrate the effects of large-scale structure explicitly by

plotting the differential surface density of galaxies brighter than $i \approx 23$ versus redshift in each of our five fields, and for our combined PRIMUS sample.[38] We find significant overdensities in the COSMOS field at $z \approx 0.35$, ≈ 0.7, and ≈ 0.85 (see also Lilly et al. 2009; Kovač et al. 2010); in our XMM-CFHTLS field at $z \approx 0.45$, ≈ 0.6, and ≈ 0.75; and in our CDFS field at $z \approx 0.7$. By constructing the area-weighted average of all five fields (thick black histogram) we are able to reduce these field-to-field variations significantly, although the effects of sample variance are still apparent. Indeed, in this and subsequent sections we show that even with five independent fields covering ≈ 5.5 deg^2, sample variance frequently limits the precision with which we can constrain the evolution of the SMF since $z = 1$. This conclusion is particularly sobering when one considers that all previous analyses of the SMF at intermediate redshift which utilized spectroscopic redshifts have been based on samples covering at most 1–2 deg^2. In any case, in the remainder of this paper we analyze the SMF constructed from the area-weighted average of all five fields, and use the jackknife technique described in Section 4.2 to empirically estimate the uncertainty in the SMF due to sample variance.

In Figure 8 we plot the SMF of all galaxies in seven redshift bins from $z = 0$–1 using our combined SDSS-*GALEX* and PRIMUS samples (see Table 4). The black squares reflect the comoving number density of galaxies in 0.1 dex wide bins of stellar mass, and the filled (open) symbols correspond to stellar mass bins above (below) our completeness limit in each redshift interval. The tan shaded region shows the total (Poisson plus sample variance) uncertainty in the SMF, and the solid curve in each panel shows the SDSS-*GALEX* SMF as the null-evolution hypothesis.

Examining Figure 8, we find strikingly little evolution in the SMF for the global galaxy population since $z \approx 1$, at least over the range of stellar masses where PRIMUS is complete. In every redshift bin the observed SMF lies very close to the local SMF, a

---

[38] Recall that a [3.6] < 21 flux cut was also applied to the CDFS and ELAIS-S1 samples (see Section 3.1).

Table 4
PRIMUS Stellar Mass Function for All, Quiescent, and Star-forming Galaxies

| log $\mathcal{M}$ ($\mathcal{M}_\odot$)	0.20 < z < 0.30			0.30 < z < 0.40			0.40 < z < 0.50			0.50 < z < 0.65			0.65 < z < 0.80			0.80 < z < 1.00		
	Φ	σ_{cv}	N	Φ	σ_{cv}	N	Φ	σ_{cv}	N	Φ	σ_{cv}	N	Φ	σ_{cv}	N	Φ	σ_{cv}	N
							All											
8.8	$-2.009^{+0.054}_{-0.048}$	0.20	172	...	...	...	...	...	...	...	...	...	...	...	...	...	...	...
8.9	$-2.039^{+0.056}_{-0.050}$	0.20	157	...	...	...	...	...	...	...	...	...	...	...	...	...	...	...
9.0	$-2.160^{+0.045}_{-0.041}$	0.10	146	...	...	...	...	...	...	...	...	...	...	...	...	...	...	...
9.1	$-2.185^{+0.050}_{-0.045}$	0.20	140	...	...	...	...	...	...	...	...	...	...	...	...	...	...	...
9.2	$-2.078^{+0.066}_{-0.057}$	0.10	160	$-2.132^{+0.043}_{-0.040}$	0.088	240	...	...	...	...	...	...	...	...	...	...	...	...
9.3	$-2.085^{+0.061}_{-0.054}$	0.099	170	$-2.210^{+0.042}_{-0.038}$	0.080	218	...	...	...	...	...	...	...	...	...	...	...	...
9.4	$-2.142^{+0.038}_{-0.035}$	0.089	190	$-2.190^{+0.079}_{-0.068}$	0.20	200	...	...	...	...	...	...	...	...	...	...	...	...
9.5	$-2.155^{+0.036}_{-0.033}$	0.042	202	$-2.183^{+0.055}_{-0.049}$	0.20	238	...	...	...	...	...	...	...	...	...	...	...	...
9.6	$-2.124^{+0.036}_{-0.033}$	0.045	227	$-2.282^{+0.032}_{-0.030}$	0.10	237	$-2.292^{+0.072}_{-0.063}$	0.20	243	...	...	...	...	...	...	...	...	...
9.7	$-2.200^{+0.037}_{-0.034}$	0.044	206	$-2.258^{+0.030}_{-0.028}$	0.094	263	$-2.347^{+0.031}_{-0.029}$	0.20	268	...	...	...	...	...	...	...	...	...
9.8	$-2.212^{+0.034}_{-0.031}$	0.040	207	$-2.235^{+0.038}_{-0.035}$	0.078	288	$-2.289^{+0.030}_{-0.028}$	0.10	311	...	...	...	...	...	...	...	...	...
9.9	$-2.242^{+0.034}_{-0.032}$	0.035	197	$-2.241^{+0.029}_{-0.027}$	0.080	290	$-2.308^{+0.040}_{-0.036}$	0.097	308	...	...	...	...	...	...	...	...	...
10.0	$-2.215^{+0.038}_{-0.035}$	0.052	199	$-2.208^{+0.031}_{-0.029}$	0.031	327	$-2.325^{+0.028}_{-0.027}$	0.060	328	$-2.419^{+0.036}_{-0.033}$	0.074	459	...	...	...	...	...	...
10.1	$-2.320^{+0.037}_{-0.034}$	0.033	169	$-2.288^{+0.033}_{-0.030}$	0.071	288	$-2.253^{+0.087}_{-0.073}$	0.023	342	$-2.394^{+0.027}_{-0.026}$	0.058	499	...	...	...	...	...	...
10.2	$-2.285^{+0.035}_{-0.033}$	0.073	184	$-2.241^{+0.026}_{-0.024}$	0.041	338	$-2.342^{+0.030}_{-0.028}$	0.093	322	$-2.371^{+0.022}_{-0.021}$	0.048	550	...	...	...	...	...	...
10.3	$-2.330^{+0.038}_{-0.035}$	0.039	166	$-2.233^{+0.027}_{-0.025}$	0.017	341	$-2.372^{+0.027}_{-0.025}$	0.055	326	$-2.388^{+0.027}_{-0.025}$	0.036	550	...	...	...	...	...	...
10.4	$-2.350^{+0.038}_{-0.035}$	0.039	158	$-2.290^{+0.027}_{-0.025}$	0.043	316	$-2.327^{+0.036}_{-0.033}$	0.026	357	$-2.382^{+0.021}_{-0.020}$	0.050	588	$-2.387^{+0.022}_{-0.021}$	0.047	593	...	...	...
10.5	$-2.380^{+0.039}_{-0.036}$	0.062	154	$-2.283^{+0.027}_{-0.025}$	0.050	309	$-2.332^{+0.030}_{-0.028}$	0.072	369	$-2.346^{+0.020}_{-0.019}$	0.035	667	$-2.320^{+0.027}_{-0.025}$	0.037	672	...	...	...
10.6	$-2.396^{+0.041}_{-0.037}$	0.067	145	$-2.332^{+0.028}_{-0.027}$	0.082	278	$-2.384^{+0.028}_{-0.026}$	0.065	336	$-2.408^{+0.020}_{-0.019}$	0.031	614	$-2.353^{+0.033}_{-0.031}$	0.055	673	...	...	...
10.7	$-2.422^{+0.043}_{-0.039}$	0.040	132	$-2.407^{+0.031}_{-0.029}$	0.060	238	$-2.360^{+0.033}_{-0.031}$	0.049	331	$-2.431^{+0.020}_{-0.019}$	0.039	609	$-2.387^{+0.029}_{-0.027}$	0.053	673	...	...	...
10.8	$-2.542^{+0.052}_{-0.047}$	0.033	94	$-2.472^{+0.034}_{-0.032}$	0.070	199	$-2.493^{+0.029}_{-0.028}$	0.086	265	$-2.502^{+0.021}_{-0.020}$	0.038	525	$-2.443^{+0.020}_{-0.019}$	0.045	667	$-2.583^{+0.028}_{-0.026}$	0.084	521
10.9	$-2.642^{+0.063}_{-0.055}$	0.074	69	$-2.579^{+0.042}_{-0.039}$	0.083	150	$-2.644^{+0.039}_{-0.036}$	0.041	187	$-2.602^{+0.025}_{-0.023}$	0.031	428	$-2.487^{+0.023}_{-0.021}$	0.054	626	$-2.658^{+0.023}_{-0.022}$	0.052	517
11.0	$-2.784^{+0.089}_{-0.075}$	0.10	39	$-2.709^{+0.046}_{-0.042}$	0.048	117	$-2.734^{+0.039}_{-0.036}$	0.058	159	$-2.729^{+0.027}_{-0.025}$	0.023	329	$-2.599^{+0.033}_{-0.031}$	0.052	473	$-2.701^{+0.028}_{-0.026}$	0.061	499
11.1	$-2.83^{+0.10}_{-0.084}$	0.30	30	$-2.819^{+0.052}_{-0.047}$	0.037	90	$-2.978^{+0.052}_{-0.047}$	0.084	93	$-2.921^{+0.033}_{-0.031}$	0.058	212	$-2.772^{+0.028}_{-0.026}$	0.040	352	$-2.842^{+0.028}_{-0.026}$	0.059	398
11.2	$-3.17^{+0.40}_{-0.20}$	0.073	8	$-3.109^{+0.076}_{-0.065}$	0.059	46	$-3.114^{+0.066}_{-0.057}$	0.10	64	$-3.118^{+0.042}_{-0.039}$	0.065	139	$-2.919^{+0.042}_{-0.039}$	0.091	235	$-3.039^{+0.035}_{-0.032}$	0.036	274
11.3	$-3.54^{+0.30}_{-0.20}$	0.030	6	$-3.34^{+0.10}_{-0.086}$	0.090	27	$-3.46^{+0.10}_{-0.083}$	0.10	30	$-3.311^{+0.059}_{-0.052}$	0.076	82	$-3.233^{+0.045}_{-0.041}$	0.065	133	$-3.296^{+0.039}_{-0.036}$	0.077	169
11.4	...	...	...	$-3.58^{+0.20}_{-0.10}$	0.079	12	$-3.67^{+0.10}_{-0.10}$	0.20	17	$-3.649^{+0.083}_{-0.071}$	0.083	42	$-3.470^{+0.056}_{-0.050}$	0.10	81	$-3.453^{+0.079}_{-0.068}$	0.063	100
11.5	...	...	...	$-4.34^{+0.40}_{-0.20}$	0.044	3	$-4.12^{+0.30}_{-0.20}$	0.047	6	$-3.80^{+0.10}_{-0.097}$	0.094	23	$-3.93^{+0.10}_{-0.10}$	0.20	22	$-3.77^{+0.10}_{-0.090}$	0.084	50
11.6	...	...	...	...	...	...	$-4.35^{+0.40}_{-0.20}$	0.091	4	$-4.52^{+0.20}_{-0.10}$	0.10	7	$-4.22^{+0.20}_{-0.10}$	0.088	11	$-4.32^{+0.10}_{-0.10}$	0.087	19
11.7	...	...	...	...	...	...	$-5.09^{+1.00}_{-0.40}$	0.50	1	$-4.21^{+0.20}_{-0.20}$	0.10	8	$-4.60^{+0.30}_{-0.20}$	0.20	5	$-4.44^{+0.20}_{-0.20}$	0.10	11
11.8	...	...	...	...	...	...	$-5.05^{+1.00}_{-0.40}$	0.50	1	...	...	...	$-4.94^{+1.00}_{-0.40}$	0.40	1	$-5.07^{+0.40}_{-0.20}$	0.088	3
11.9	...	...	...	...	...	...	...	...	...	...	...	...	$-4.48^{+1.00}_{-0.40}$	0.10	1	...	...	...
12.0	...	...	...	...	...	...	...	...	...	...	...	...	$-5.48^{+1.00}_{-0.40}$	1.4	1	$-5.71^{+1.00}_{-0.40}$	0.40	1

Moustakas et al.

Table 4
(Continued)

log $\mathcal{M}$ ($\mathcal{M}_\odot$)	0.20 < z < 0.30			0.30 < z < 0.40			0.40 < z < 0.50			0.50 < z < 0.65			0.65 < z < 0.80			0.80 < z < 1.00		
	Φ	σ_{cv}	N	Φ	σ_{cv}	N	Φ	σ_{cv}	N	Φ	σ_{cv}	N	Φ	σ_{cv}	N	Φ	σ_{cv}	N
							Star-forming											
8.8	$-2.014^{+0.054}_{-0.049}$	0.20	171	...	...	...	...	...	...	...	...	...	...	...	...	...	...	...
8.9	$-2.125^{+0.043}_{-0.040}$	0.084	149	...	...	...	...	...	...	...	...	...	...	...	...	...	...	...
9.0	$-2.205^{+0.044}_{-0.040}$	0.10	140	...	...	...	...	...	...	...	...	...	...	...	...	...	...	...
9.1	$-2.250^{+0.045}_{-0.041}$	0.20	133	$-2.156^{+0.057}_{-0.051}$	0.097	196	...	...	...	...	...	...	...	...	...	...	...	...
9.2	$-2.133^{+0.071}_{-0.062}$	0.10	147	$-2.196^{+0.032}_{-0.030}$	0.085	235	...	...	...	...	...	...	...	...	...	...	...	...
9.3	$-2.114^{+0.064}_{-0.056}$	0.087	160	$-2.290^{+0.034}_{-0.031}$	0.073	209	...	...	...	...	...	...	...	...	...	...	...	...
9.4	$-2.216^{+0.038}_{-0.035}$	0.099	171	$-2.316^{+0.041}_{-0.037}$	0.20	188	$-2.325^{+0.034}_{-0.032}$	0.10	228	...	...	...	...	...	...	...	...	...
9.5	$-2.233^{+0.037}_{-0.034}$	0.052	180	$-2.294^{+0.034}_{-0.031}$	0.10	220	$-2.335^{+0.034}_{-0.032}$	0.10	248	...	...	...	...	...	...	...	...	...
9.6	$-2.231^{+0.035}_{-0.033}$	0.053	195	$-2.364^{+0.034}_{-0.031}$	0.088	208	$-2.318^{+0.077}_{-0.066}$	0.20	233	...	...	...	...	...	...	...	...	...
9.7	$-2.289^{+0.041}_{-0.038}$	0.047	170	$-2.340^{+0.032}_{-0.030}$	0.075	229	$-2.369^{+0.032}_{-0.030}$	0.20	261	$-2.438^{+0.029}_{-0.027}$	0.20	383	...	...	...	...	...	...
9.8	$-2.336^{+0.039}_{-0.036}$	0.036	159	$-2.346^{+0.030}_{-0.029}$	0.054	248	$-2.364^{+0.032}_{-0.029}$	0.10	280	$-2.528^{+0.027}_{-0.025}$	0.20	354	...	...	...	...	...	...
9.9	$-2.347^{+0.039}_{-0.036}$	0.042	154	$-2.354^{+0.033}_{-0.031}$	0.074	233	$-2.402^{+0.033}_{-0.030}$	0.087	275	$-2.493^{+0.033}_{-0.031}$	0.10	390	...	...	...	...	...	...
10.0	$-2.364^{+0.046}_{-0.042}$	0.032	143	$-2.354^{+0.038}_{-0.035}$	0.030	236	$-2.430^{+0.031}_{-0.029}$	0.033	276	$-2.480^{+0.039}_{-0.036}$	0.052	421	$-2.642^{+0.029}_{-0.027}$	0.20	329	...	...	...
10.1	$-2.509^{+0.047}_{-0.043}$	0.035	109	$-2.452^{+0.042}_{-0.039}$	0.081	200	$-2.36^{+0.10}_{-0.093}$	0.048	268	$-2.516^{+0.024}_{-0.030}$	0.037	434	$-2.637^{+0.032}_{-0.030}$	0.082	329	...	...	...
10.2	$-2.526^{+0.047}_{-0.043}$	0.077	108	$-2.426^{+0.032}_{-0.030}$	0.038	224	$-2.502^{+0.036}_{-0.033}$	0.090	235	$-2.491^{+0.025}_{-0.024}$	0.018	443	$-2.564^{+0.030}_{-0.028}$	0.055	406	...	...	...
10.3	$-2.576^{+0.050}_{-0.045}$	0.039	97	$-2.430^{+0.032}_{-0.030}$	0.026	223	$-2.530^{+0.032}_{-0.030}$	0.050	234	$-2.593^{+0.025}_{-0.023}$	0.046	384	$-2.527^{+0.031}_{-0.029}$	0.041	429	$-2.639^{+0.066}_{-0.058}$	0.064	340
10.4	$-2.715^{+0.058}_{-0.051}$	0.10	74	$-2.515^{+0.035}_{-0.033}$	0.054	188	$-2.545^{+0.032}_{-0.029}$	0.055	231	$-2.593^{+0.026}_{-0.025}$	0.056	380	$-2.561^{+0.025}_{-0.024}$	0.038	438	$-2.697^{+0.057}_{-0.051}$	0.10	323
10.5	$-2.614^{+0.052}_{-0.046}$	0.065	92	$-2.542^{+0.037}_{-0.034}$	0.045	172	$-2.556^{+0.036}_{-0.033}$	0.063	227	$-2.566^{+0.028}_{-0.026}$	0.026	412	$-2.575^{+0.025}_{-0.024}$	0.063	441	$-2.783^{+0.044}_{-0.040}$	0.081	304
10.6	$-2.691^{+0.059}_{-0.053}$	0.083	73	$-2.640^{+0.041}_{-0.038}$	0.056	139	$-2.617^{+0.038}_{-0.035}$	0.044	197	$-2.646^{+0.028}_{-0.026}$	0.044	357	$-2.579^{+0.050}_{-0.045}$	0.075	401	$-2.873^{+0.036}_{-0.034}$	0.038	301
10.7	$-2.769^{+0.065}_{-0.057}$	0.066	61	$-2.736^{+0.046}_{-0.041}$	0.056	116	$-2.615^{+0.036}_{-0.033}$	0.074	195	$-2.686^{+0.028}_{-0.026}$	0.048	332	$-2.612^{+0.045}_{-0.041}$	0.082	390	$-2.944^{+0.034}_{-0.031}$	0.066	289
10.8	$-2.894^{+0.087}_{-0.073}$	0.096	39	$-2.865^{+0.055}_{-0.049}$	0.071	83	$-2.762^{+0.041}_{-0.037}$	0.069	146	$-2.815^{+0.031}_{-0.029}$	0.045	252	$-2.744^{+0.029}_{-0.027}$	0.053	333	$-2.908^{+0.041}_{-0.038}$	0.10	280
10.9	$-3.18^{+0.10}_{-0.10}$	0.028	19	$-2.905^{+0.059}_{-0.052}$	0.063	74	$-2.978^{+0.067}_{-0.059}$	0.071	84	$-2.980^{+0.035}_{-0.033}$	0.033	189	$-2.788^{+0.037}_{-0.034}$	0.079	304	$-3.011^{+0.036}_{-0.033}$	0.079	242
11.0	$-3.38^{+0.20}_{-0.20}$	0.20	7	$-3.113^{+0.078}_{-0.067}$	0.054	46	$-3.117^{+0.061}_{-0.054}$	0.092	69	$-3.139^{+0.043}_{-0.039}$	0.023	130	$-3.000^{+0.042}_{-0.038}$	0.049	193	$-3.113^{+0.043}_{-0.039}$	0.10	203
11.1	$-3.37^{+0.20}_{-0.10}$	0.094	10	$-3.43^{+0.10}_{-0.090}$	0.086	24	$-3.347^{+0.083}_{-0.070}$	0.061	40	$-3.368^{+0.060}_{-0.053}$	0.090	73	$-3.148^{+0.045}_{-0.041}$	0.097	139	$-3.279^{+0.044}_{-0.040}$	0.10	148
11.2	...	...	...	$-3.67^{+0.20}_{-0.10}$	0.076	13	$-3.54^{+0.10}_{-0.093}$	0.10	24	$-3.539^{+0.069}_{-0.060}$	0.084	55	$-3.286^{+0.059}_{-0.052}$	0.10	107	$-3.405^{+0.063}_{-0.055}$	0.065	114
11.3	$-4.60^{+1.00}_{-0.40}$	1.6	1	$-4.04^{+0.40}_{-0.20}$	0.20	4	$-3.83^{+0.20}_{-0.10}$	0.090	13	$-3.93^{+0.10}_{-0.100}$	0.10	20	$-3.671^{+0.072}_{-0.063}$	0.10	51	$-3.630^{+0.063}_{-0.056}$	0.095	72
11.4	...	...	...	$-4.15^{+0.40}_{-0.20}$	0.20	3	$-4.23^{+0.40}_{-0.20}$	0.20	4	$-4.08^{+0.10}_{-0.10}$	0.10	15	$-4.04^{+0.10}_{-0.092}$	0.096	23	$-3.92^{+0.10}_{-0.087}$	0.10	37
11.5	...	...	...	$-4.57^{+0.60}_{-0.30}$	0.60	2	$-4.73^{+1.00}_{-0.40}$	0.70	1	$-4.66^{+0.30}_{-0.20}$	0.50	5	$-4.43^{+0.20}_{-0.20}$	0.20	7	$-4.22^{+0.10}_{-0.10}$	0.046	19
11.6	...	...	...	...	...	...	$-5.01^{+1.00}_{-0.40}$	1.4	1	$-5.34^{+1.00}_{-0.40}$	0.0089	1	$-5.06^{+0.60}_{-0.30}$	1.0	2	$-5.05^{+0.40}_{-0.20}$	0.10	3
11.7	...	...	...	...	...	...	...	...	...	$-4.81^{+0.40}_{-0.20}$	0.0026	3	$-4.75^{+0.50}_{-0.30}$	0.50	3	$-4.81^{+0.60}_{-0.30}$	0.20	3
11.8	...	...	...	...	...	...	...	...	...	...	...	...	$-4.94^{+1.00}_{-0.40}$	0.80	1	$-5.42^{+1.00}_{-0.40}$	0.60	1
12.0	...	...	...	...	...	...	...	...	...	...	...	...	$-5.48^{+1.00}_{-0.40}$	2.7	1	...	...	...

Table 4
(Continued)

log $\mathcal{M}$ ($\mathcal{M}_\odot$)	0.20 < z < 0.30			0.30 < z < 0.40			0.40 < z < 0.50			0.50 < z < 0.65			0.65 < z < 0.80			0.80 < z < 1.00		
	Φ	σ_{cv}	N	Φ	σ_{cv}	N	Φ	σ_{cv}	N	Φ	σ_{cv}	N	Φ	σ_{cv}	N	Φ	σ_{cv}	N
								Quiescent										
9.3	$-3.27^{+0.20}_{-0.10}$	0.20	10	...	...	...	...	...	...	...	...	...	...	...	...	...	...	...
9.4	$-2.95^{+0.20}_{-0.10}$	0.052	19	...	...	...	...	...	...	...	...	...	...	...	...	...	...	...
9.5	$-2.94^{+0.10}_{-0.10}$	0.047	22	...	...	...	...	...	...	...	...	...	...	...	...	...	...	...
9.6	$-2.79^{+0.10}_{-0.098}$	0.079	32	$-3.043^{+0.100}_{-0.083}$	0.047	29	...	...	...	...	...	...	...	...	...	...	...	...
9.7	$-2.931^{+0.088}_{-0.074}$	0.076	36	$-3.021^{+0.095}_{-0.079}$	0.10	34	...	...	...	...	...	...	...	...	...	...	...	...
9.8	$-2.818^{+0.075}_{-0.064}$	0.096	48	$-2.88^{+0.20}_{-0.10}$	0.20	40	...	...	...	...	...	...	...	...	...	...	...	...
9.9	$-2.910^{+0.079}_{-0.067}$	0.020	43	$-2.880^{+0.070}_{-0.061}$	0.10	57	$-3.02^{+0.20}_{-0.10}$	0.20	33	...	...	...	...	...	...	...	...	...
10.0	$-2.754^{+0.072}_{-0.062}$	0.10	56	$-2.753^{+0.052}_{-0.047}$	0.041	91	$-2.991^{+0.076}_{-0.065}$	0.20	52	...	...	...	...	...	...	...	...	...
10.1	$-2.773^{+0.066}_{-0.058}$	0.040	60	$-2.791^{+0.053}_{-0.047}$	0.064	88	$-2.908^{+0.061}_{-0.054}$	0.10	74	...	...	...	...	...	...	...	...	...
10.2	$-2.655^{+0.057}_{-0.051}$	0.077	76	$-2.700^{+0.046}_{-0.041}$	0.059	114	$-2.854^{+0.056}_{-0.050}$	0.10	87	$-2.988^{+0.052}_{-0.047}$	0.10	107	...	...	...	...	...	...
10.3	$-2.694^{+0.062}_{-0.054}$	0.082	69	$-2.672^{+0.051}_{-0.046}$	0.037	118	$-2.889^{+0.052}_{-0.047}$	0.070	92	$-2.814^{+0.061}_{-0.054}$	0.049	166	...	...	...	...	...	...
10.4	$-2.595^{+0.054}_{-0.048}$	0.067	84	$-2.682^{+0.043}_{-0.039}$	0.027	128	$-2.730^{+0.083}_{-0.070}$	0.044	126	$-2.795^{+0.035}_{-0.032}$	0.042	208	...	...	...	...	...	...
10.5	$-2.760^{+0.064}_{-0.057}$	0.067	62	$-2.631^{+0.041}_{-0.038}$	0.068	137	$-2.726^{+0.056}_{-0.050}$	0.090	142	$-2.746^{+0.031}_{-0.029}$	0.050	255	$-2.672^{+0.054}_{-0.049}$	0.049	231	...	...	...
10.6	$-2.702^{+0.060}_{-0.053}$	0.059	72	$-2.628^{+0.041}_{-0.038}$	0.10	139	$-2.765^{+0.041}_{-0.038}$	0.10	139	$-2.783^{+0.031}_{-0.029}$	0.032	257	$-2.745^{+0.040}_{-0.037}$	0.036	272	...	...	...
10.7	$-2.681^{+0.060}_{-0.053}$	0.077	71	$-2.682^{+0.044}_{-0.040}$	0.077	122	$-2.713^{+0.063}_{-0.056}$	0.047	136	$-2.784^{+0.029}_{-0.027}$	0.031	277	$-2.781^{+0.030}_{-0.029}$	0.062	283	...	...	...
10.8	$-2.799^{+0.069}_{-0.060}$	0.096	55	$-2.698^{+0.046}_{-0.041}$	0.072	116	$-2.830^{+0.045}_{-0.041}$	0.10	119	$-2.792^{+0.030}_{-0.028}$	0.040	273	$-2.745^{+0.028}_{-0.026}$	0.045	334	$-2.861^{+0.040}_{-0.037}$	0.061	241
10.9	$-2.790^{+0.074}_{-0.064}$	0.076	50	$-2.856^{+0.065}_{-0.057}$	0.10	76	$-2.915^{+0.049}_{-0.044}$	0.031	103	$-2.837^{+0.035}_{-0.032}$	0.063	239	$-2.788^{+0.028}_{-0.026}$	0.032	322	$-2.913^{+0.031}_{-0.029}$	0.041	275
11.0	$-2.913^{+0.098}_{-0.081}$	0.082	32	$-2.927^{+0.060}_{-0.053}$	0.079	71	$-2.967^{+0.053}_{-0.047}$	0.052	90	$-2.942^{+0.035}_{-0.032}$	0.027	199	$-2.819^{+0.049}_{-0.045}$	0.056	280	$-2.914^{+0.037}_{-0.034}$	0.042	296
11.1	$-2.97^{+0.10}_{-0.10}$	0.30	20	$-2.942^{+0.062}_{-0.053}$	0.049	66	$-3.220^{+0.072}_{-0.062}$	0.10	53	$-3.114^{+0.041}_{-0.038}$	0.058	139	$-3.008^{+0.037}_{-0.034}$	0.022	213	$-3.040^{+0.038}_{-0.035}$	0.034	250
11.2	$-3.17^{+0.40}_{-0.20}$	0.073	8	$-3.248^{+0.092}_{-0.077}$	0.081	33	$-3.317^{+0.086}_{-0.073}$	0.20	40	$-3.325^{+0.057}_{-0.050}$	0.063	84	$-3.162^{+0.063}_{-0.055}$	0.091	128	$-3.283^{+0.042}_{-0.038}$	0.034	160
11.3	$-3.58^{+0.30}_{-0.20}$	0.065	5	$-3.44^{+0.10}_{-0.092}$	0.20	23	$-3.71^{+0.10}_{-0.10}$	0.10	17	$-3.431^{+0.070}_{-0.061}$	0.081	62	$-3.430^{+0.060}_{-0.053}$	0.076	82	$-3.566^{+0.050}_{-0.045}$	0.085	97
11.4	...	...	...	$-3.72^{+0.20}_{-0.10}$	0.10	9	$-3.81^{+0.10}_{-0.10}$	0.10	13	$-3.85^{+0.10}_{-0.088}$	0.065	27	$-3.606^{+0.068}_{-0.059}$	0.10	58	$-3.63^{+0.10}_{-0.092}$	0.087	63
11.5	...	...	...	$-4.71^{+1.00}_{-0.40}$	1.2	1	$-4.25^{+0.30}_{-0.20}$	0.30	5	$-3.86^{+0.10}_{-0.10}$	0.084	18	$-4.09^{+0.10}_{-0.10}$	0.10	15	$-3.95^{+0.20}_{-0.10}$	0.10	31
11.6	...	...	...	...	...	...	$-4.46^{+0.40}_{-0.20}$	0.045	3	$-4.59^{+0.30}_{-0.20}$	0.50	6	$-4.29^{+0.20}_{-0.20}$	0.10	9	$-4.41^{+0.10}_{-0.10}$	0.089	16
11.7	...	...	...	...	...	...	$-5.09^{+1.00}_{-0.40}$	0.20	1	$-4.33^{+0.30}_{-0.20}$	0.10	5	$-5.12^{+0.60}_{-0.20}$	0.80	2	$-4.68^{+0.20}_{-0.20}$	0.099	8
11.8	...	...	...	...	...	...	$-5.05^{+1.00}_{-0.40}$	0.20	1	...	...	...	...	...	...	$-5.33^{+0.60}_{-0.30}$	0.40	2
11.9	...	...	...	...	...	...	...	...	...	...	...	...	$-4.48^{+1.00}_{-0.40}$	0.20	1	...	...	...
12.0	...	...	...	...	...	...	...	...	...	...	...	...	...	...	...	$-5.71^{+1.00}_{-0.40}$	1.1	1

Notes. PRIMUS stellar mass function at $z = 0.2$–1 for all, star-forming, and quiescent galaxies. The units of Φ are 10^{-4} Mpc^{-3} dex^{-1}, σ_{cv} is the estimated 1σ uncertainty in Φ due to sample variance, and N is the number of galaxies in each stellar mass bin.
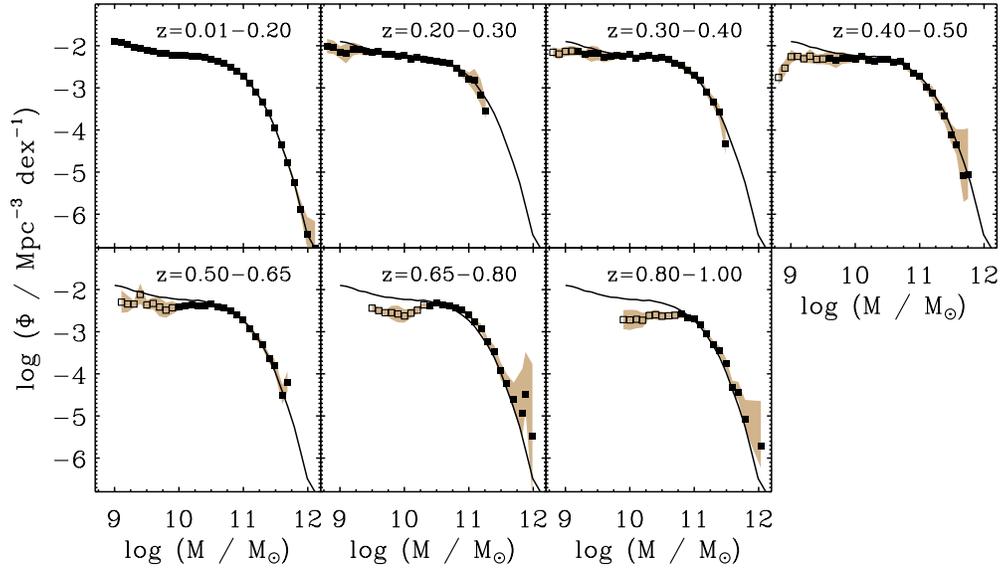
Figure 8. Evolution of the SMF from $z = 0$–1. The black squares show the comoving number density of galaxies in 0.1 dex wide bins of stellar mass based on our SDSS-*GALEX* (upper-left panel) and PRIMUS samples (subsequent six panels), respectively. Filled (open) squares indicate stellar mass bins above (below) the stellar mass completeness limit at the center of each redshift bin. The shaded tan region in each panel reflects the quadrature sum of the Poisson and sample variance uncertainties in the SMF, and the solid curve, reproduced in every panel for reference, shows the SDSS-*GALEX* SMF. We find that the SMF for the ensemble population of galaxies has evolved remarkably little over the range of redshifts and stellar masses where PRIMUS is complete.

(A color version of this figure is available in the online journal.)

Table 5
Cumulative Number and Stellar Mass Density of All Galaxies

$\langle z \rangle$	$\log(n)$[a]	$\log(\rho)$[b]	$\log(n)$	$\log(\rho)$	$\log(n)$	$\log(\rho)$	$\log(n)$	$\log(\rho)$
	$\log(\mathcal{M}/\mathcal{M}_\odot) > 9.5$		$\log(\mathcal{M}/\mathcal{M}_\odot) > 10$		$\log(\mathcal{M}/\mathcal{M}_\odot) > 10.5$		$\log(\mathcal{M}/\mathcal{M}_\odot) > 11$	
0.100	-2.09 ± 0.05	8.35 ± 0.05	-2.32 ± 0.05	8.31 ± 0.05	-2.68 ± 0.05	8.18 ± 0.05	-3.41 ± 0.05	7.78 ± 0.04
0.250	-2.12 ± 0.05	8.32 ± 0.09	-2.36 ± 0.06	8.28 ± 0.10	-2.70 ± 0.09	8.16 ± 0.13	-3.41 ± 0.29	7.78 ± 0.29
0.350	-2.11 ± 0.06	8.35 ± 0.06	-2.30 ± 0.05	8.32 ± 0.06	-2.65 ± 0.07	8.20 ± 0.07	-3.39 ± 0.10	7.77 ± 0.11
0.450	-2.16 ± 0.09	8.31 ± 0.08	-2.35 ± 0.07	8.27 ± 0.08	-2.69 ± 0.08	8.16 ± 0.09	-3.47 ± 0.14	7.70 ± 0.16
0.575	> -2.22	> 8.30	-2.39 ± 0.04	8.28 ± 0.05	-2.69 ± 0.04	8.18 ± 0.05	-3.42 ± 0.08	7.78 ± 0.10
0.725	. . .	. . .	> -2.37	> 8.35	-2.61 ± 0.05	8.27 ± 0.05	-3.28 ± 0.07	7.90 ± 0.08
0.900	. . .	. . .	. . .	. . .	> -2.79	> 8.15	-3.35 ± 0.07	7.85 ± 0.07

Notes.
[a] Number density in h_{70}^3 Mpc^{-3}.
[b] Stellar mass density in $h_{70}\,\mathcal{M}_\odot$ Mpc^{-3}.

result which we quantify below. Given the expected stellar mass growth of galaxies due to star formation (see, e.g., Figure 1) and galaxy mergers, this result may at first appear surprising. However, in Section 5.2.2, we show that the lack of significant evolution in the SMF for the ensemble galaxy population is a consequence of how the SMFs of the star-forming and quiescent galaxy populations separately evolve. Moreover, in Section 6.1 we show that the relative lack of evolution in the global SMF, especially at the massive end, suggests that mergers do not appear to play a significant role for the stellar mass growth of galaxies at $z < 1$.

By integrating the SMF above various stellar mass thresholds we can quantify the observed (lack of) evolution in the SMF, and look for evidence of mass assembly downsizing within the global galaxy population (see Section 1). In Figure 9 we plot versus redshift the cumulative number density of galaxies with stellar masses greater than $10^{9.5}$, 10^{10}, $10^{10.5}$, and $10^{11}\,\mathcal{M}_\odot$. We focus here on the number density evolution, although the evolution in stellar mass density leads to the same basic conclusions (see Table 5). We integrate the observed SMF directly, but exclude stellar mass bins containing fewer than three galaxies

where the SMF is noisiest. We use the best-fitting Schechter model to extrapolate the observed SMF as needed over small intervals of stellar mass. We emphasize, however, that these model-dependent corrections typically modify the measured number densities by $\lesssim 0.02$ dex, and therefore potential errors in the extrapolations do not affect any of our conclusions. The solid black squares in Figure 9 show the mean number density, while the vertical error bars indicate the Poisson uncertainty; the thin black boxes around each point indicate the quadrature sum of the Poisson and sample variance uncertainties in the vertical direction, and the redshift bin width in the horizontal direction. This graphical representation shows that sample variance uncertainties are frequently comparable to or larger than the Poisson uncertainties. Finally, symbols with upward-pointing arrows represent lower limits, and the gray shaded region shows for reference the comoving number density of galaxies at $z \approx 0.1$, to illustrate the case of no evolution.

Figure 9 shows that the cumulative number density of galaxies above all four stellar mass thresholds does not appear to change significantly over the range of redshifts where PRIMUS is complete. To quantify this result, we fit a power-law function of
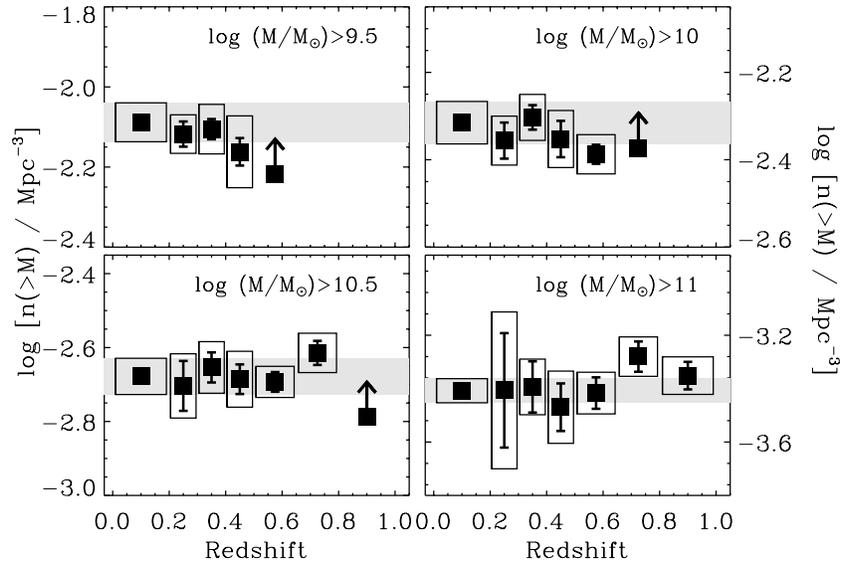
Figure 9. Evolution of the cumulative comoving space density of galaxies more massive than (top-left) $10^{9.5} \, \mathcal{M}_\odot$, (top-right) $10^{10} \, \mathcal{M}_\odot$, (bottom-left) $10^{10.5} \, \mathcal{M}_\odot$, and (bottom-right) $10^{11} \, \mathcal{M}_\odot$ from $z = 0$–1 based on the SMFs presented in Figure 8. The error bars reflect the Poisson uncertainty on each number density measurement, and the thin black boxes reflect the quadrature sum of the Poisson and sample variance uncertainties in the vertical direction, and the redshift bin width in the horizontal direction. We designate lower limits using upward-pointing arrows. The gray shaded region in each panel shows—as the null-evolution hypothesis—the number density of galaxies at $z \approx 0.1$ based on our SDSS-*GALEX* sample. We find that the cumulative number density of galaxies with $\mathcal{M} > 10^{9.5} \, \mathcal{M}_\odot$ and $\mathcal{M} > 10^{10} \, \mathcal{M}_\odot$ has increased by $15\% \pm 10\%$ and $21\% \pm 19\%$ since $z = 0.4$ and $z = 0.6$, respectively, while the cumulative space density of $\mathcal{M} > 10^{10.5} \, \mathcal{M}_\odot$ and $\mathcal{M} > 10^{11} \, \mathcal{M}_\odot$ galaxies has changed by just $4.7\% \pm 12\%$ and $11\% \pm 17\%$ since $z = 0.8$ and $z = 1$, respectively.

redshift, $n \propto (1+z)^\gamma$, to the measured densities, excluding lower limits. We scale the formal statistical uncertainties by $\sqrt{\chi_\nu^2}$, the square root of the χ^2 statistic divided by the number of degrees of freedom, in order to be able to intercompare the significance of the evolutionary trends across all four stellar mass thresholds. We find $\gamma = -0.43 \pm 0.3, -0.40 \pm 0.4, 0.17 \pm 0.4$, and 0.32 ± 0.4 for the evolution in the cumulative number of galaxies more massive than $10^{9.5}, 10^{10}, 10^{10.5},$ and $10^{11} \, \mathcal{M}_\odot$, respectively. Above the two highest stellar mass thresholds, the measured number densities at $z \approx 0.7$, and to a lesser extent at $z \approx 0.9$, are clearly affected by the large-scale overdensities in several of the PRIMUS fields (see Figure 7). Therefore, excluding the $z \approx 0.7$ redshift bin, we obtain $\gamma = -0.08 \pm 0.2$ and 0.16 ± 0.3 above $10^{10.5}$ and $10^{11} \, \mathcal{M}_\odot$, respectively. Stated another way, the cumulative number of $\mathcal{M} > 10^{9.5} \, \mathcal{M}_\odot$ and $\mathcal{M} > 10^{10} \, \mathcal{M}_\odot$ galaxies has increased by $15\% \pm 10\%$ and $21\% \pm 19\%$ since $z = 0.4$ and $z = 0.6$, respectively. Meanwhile, the cumulative space density of $\mathcal{M} > 10^{10.5} \, \mathcal{M}_\odot$ and $\mathcal{M} > 10^{11} \, \mathcal{M}_\odot$ galaxies has remained relatively constant, changing by just $4.7\% \pm 12\%$ and $11\% \pm 17\%$ since $z = 0.8$ and $z = 1$, respectively.

Thus, while we find hints of mass assembly downsizing—a more rapid increase in the number of lower-mass galaxies toward low redshift—the trends are only marginally significant. By contrast, previous studies have found much stronger evidence for downsizing within the global galaxy population (see, e.g., Fontana et al. 2006; Pérez-González et al. 2008; Pozzetti et al. 2007, 2010). For example, Pozzetti et al. (2010) report a $32\% \pm 6\%$ increase in the cumulative number of $\mathcal{M} > 10^{9.5} \, \mathcal{M}_\odot$ galaxies since $z = 0.44$, and no statistically significant change ($7\% \pm 17\%$) in the number density of galaxies more massive than $10^{11} \, \mathcal{M}_\odot$ since $z = 1$ based on an analysis of the COSMOS field. While our findings are qualitatively consistent with these studies—many of which pushed further down the stellar mass function at higher redshift, and therefore had a larger lever arm with which to detect downsizing—we also find that sample

variance can wash out the significance of the observed trends (see also Fontanot et al. 2009). In any case, we will show in Section 5.2.2 that by measuring the change in the number density of galaxies within fixed bins of stellar mass (as opposed to using stellar mass thresholds) the signatures of downsizing will become more apparent.

5.2.2. Quiescent and Star-forming Galaxies

In the previous section we measured the evolution of the SMF for the ensemble population of galaxies from $z = 0$–1. We found only a marginally significant increase ($16\% \pm 9\%$) in the cumulative number density of all $\mathcal{M} \gtrsim 10^{9.5} \, \mathcal{M}_\odot$ galaxies since $z \approx 0.6$, and very little change ($8\% \pm 10\%$) in the space density of $\mathcal{M} \gtrsim 10^{10.5} \, \mathcal{M}_\odot$ galaxies since $z \approx 1$. Here, we investigate these results in more detail by dividing our sample into quiescent and star-forming galaxies based on the criteria defined in Section 3.2.

In Figure 10 we plot the SMFs of quiescent and star-forming galaxies in seven redshift bins from $z = 0$–1. Filled (open) symbols indicate stellar mass bins above (below) our completeness limit at the center of each redshift bin, and the solid red and dashed blue curves, reproduced in every panel for reference, show the SDSS-*GALEX* quiescent and star-forming galaxy SMFs, respectively. In Section 5.3 we compare our type-dependent SMFs against published measurements and show that they are broadly consistent with previous studies.

Figure 10 shows that the strong stellar mass dependence of galaxy bimodality observed among local galaxies persists over the full range of redshifts probed by PRIMUS. In other words, we find that quiescent galaxies dominate the massive end ($\gtrsim 10^{11} \, \mathcal{M}_\odot$) of the SMF, and star-forming galaxies dominate among intermediate-mass ($\sim 10^{10} \, \mathcal{M}_\odot$) galaxies at all redshifts from $z = 0$–1. However, we also observe several striking evolutionary trends. Among quiescent galaxies, the number of intermediate-mass galaxies increases dramatically toward the current epoch, while the massive end of the SMF remains
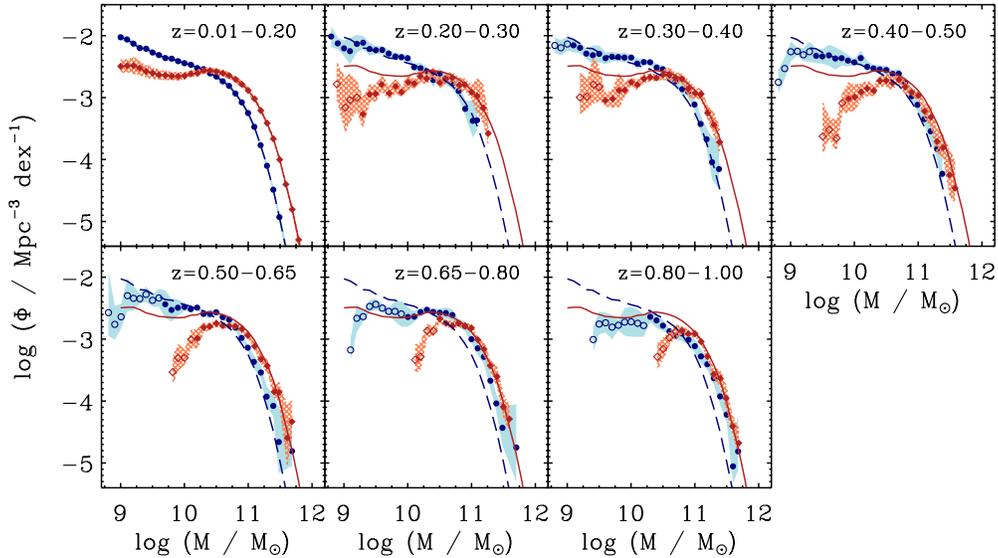
Figure 10. Evolution of the SMFs of quiescent (dark red diamonds and light red hatched region) and star-forming (dark blue points and light blue shaded region) galaxies from $z = 0$–1. Filled (open) symbols correspond to stellar mass bins above (below) our stellar mass completeness limit in each redshift interval. The dashed blue and solid red curves are the SDSS-*GALEX* star-forming and quiescent-galaxy SMFs (upper-left panel), and have been reproduced in every panel for reference. We find a significant increase in the number of intermediate-mass ($\sim 10^{10}\,\mathcal{M}_\odot$) quiescent galaxies toward lower redshift, but essentially no change in the SMF of quiescent galaxies above $\sim 10^{11}\,\mathcal{M}_\odot$. Meanwhile, the SMF of star-forming galaxies is largely invariant below $\sim 10^{11}\,\mathcal{M}_\odot$ (at least where PRIMUS is complete), but exhibits significant evolution above $\sim 10^{11}\,\mathcal{M}_\odot$ by shifting toward lower stellar mass at fixed number density with decreasing redshift.

(A color version of this figure is available in the online journal.)

remarkably fixed. Meanwhile, the largest changes in the SMF of star-forming galaxies occur at the massive end. We find a perceptible shift in the star-forming galaxy SMF toward lower mass at fixed number density with decreasing redshift, while the low-mass end of the SMF remains relatively constant over the whole range of stellar masses and redshifts where our sample is complete. The so-called transition mass—the stellar mass at which the quiescent and star-forming galaxy SMFs cross—evolves roughly as $\propto (1 + z)^{1.5}$, from $\sim 3 \times 10^{10}\,\mathcal{M}_\odot$ at $z \approx 0.1$ to $\sim 7 \times 10^{10}\,\mathcal{M}_\odot$ at $z \approx 0.9$, which agrees reasonably well with previous measurements (e.g., Bundy et al. 2006; Vergani et al. 2008; Pozzetti et al. 2010). It is not clear, however, that the transition mass has any physical interpretation, as Figure 10 shows that its evolution is entirely driven by the rise in the number of intermediate-mass quiescent galaxies (e.g., Borch et al. 2006; Cattaneo et al. 2008).

Another way to visualize these results is with Figure 11, which shows the individual SMFs from all seven redshift bins on top of one another. For clarity, we only plot each SMF above our stellar mass completeness limit, and we only show stellar mass bins containing three or more galaxies. In the left panel we use progressively lighter shades of blue to show the evolution of the star-forming galaxy SMF, and in the right panel we show the evolution of the quiescent-galaxy SMF using progressively lighter shades of orange. The black shaded region shows the corresponding SDSS-*GALEX* SMF, which we plot on top so that the changes in the SMF with redshift can be more easily evaluated. This figure clearly shows the significant steepening of the low-mass end of the SMF of quiescent galaxies toward lower redshift, and the simultaneous decline in the number of massive star-forming galaxies.

In Figure 12 we quantify the observed evolution by plotting the integrated number density of galaxies measured in four 0.5 dex wide intervals of stellar mass between $10^{9.5}$–$10^{11.5}\,\mathcal{M}_\odot$. As in Section 5.2.1, we calculate the number density by integrating the observed SMFs directly, excluding stellar mass bins

with fewer than three galaxies, and use our Schechter model fits to extrapolate over small ranges of stellar mass. We plot the evolution in the number density of all, quiescent, and star-forming galaxies using black squares, red diamonds, and blue points, respectively, and indicate lower limits on the number density in redshift bins where our SMF is partially incomplete using upward-pointing arrows. The error bars reflect the quadrature sum of the Poisson and sample variance uncertainties. We list the derived number and stellar mass densities in Table 6.

We quantify the observed trends by fitting a power-law function of redshift to the measured number densities, given by

$$n(z) = n_0(1 + z)^{\gamma}. \tag{9}$$

In addition, we model the evolution in the stellar mass density, $\rho(z)$, as

$$\rho(z) = \rho_0(1 + z)^{\beta}. \tag{10}$$

In detail, we fit the data in $\log(n)$–$\log(1+z)$ and $\log(\rho)$–$\log(1+z)$ space using weighted linear least-squares minimization, and we only fit over the range of redshifts where our measurements are complete (i.e., we ignore lower limits). We also exclude from the fits our measurements at $z \approx 0.7$ because of the above-average overdensity of galaxies in this redshift bin (see Figure 7). We emphasize, however, that including this redshift bin would only strengthen our claim of minimal evolution in the number density of massive galaxies; in other words, excluding the $z \approx 0.7$ measurements is a conservative choice. The solid black, dot-dashed red, and dashed blue lines in Figure 12 show the results of fitting the number density of all, quiescent, and star-forming galaxies, respectively, and the corresponding shaded regions show the 1σ range of power-law fits drawn from the full covariance matrix. Table 7 lists the best-fitting coefficients and uncertainties, where the uncertainties have been rescaled as in Section 5.2.1 such that $\chi^2_\nu = 1$.

Figure 12 synthesizes nearly all the key results of this section, and conveys many of the core conclusions of this paper. First,
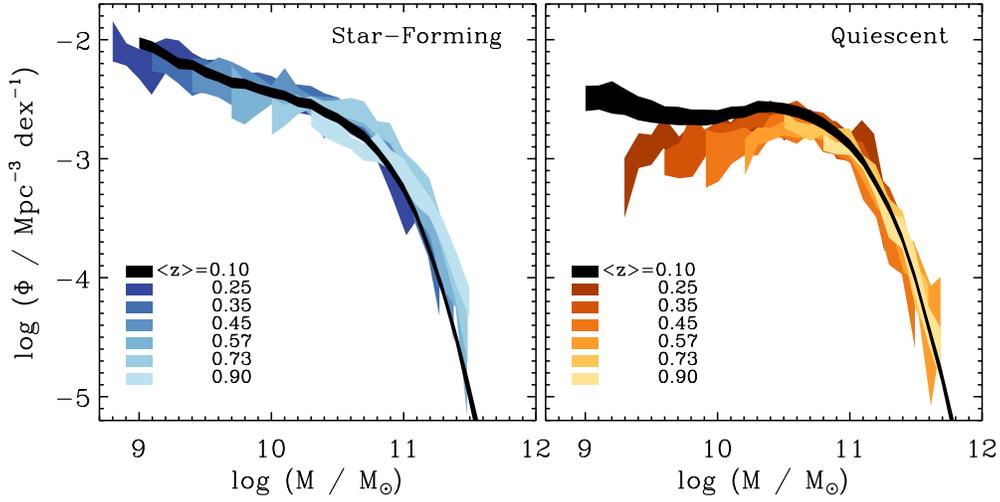
Figure 11. Evolution of the SMFs of (left) star-forming and (right) quiescent galaxies from $z = 0–1$ based on the data presented in Figure 10. We use progressively lighter shades of blue to show the evolution of the star-forming galaxy SMF, and shades of orange to show how the SMF of quiescent galaxies has evolved. The black shaded region in each panel shows the corresponding SDSS-*GALEX* SMF.

(A color version of this figure is available in the online journal.)
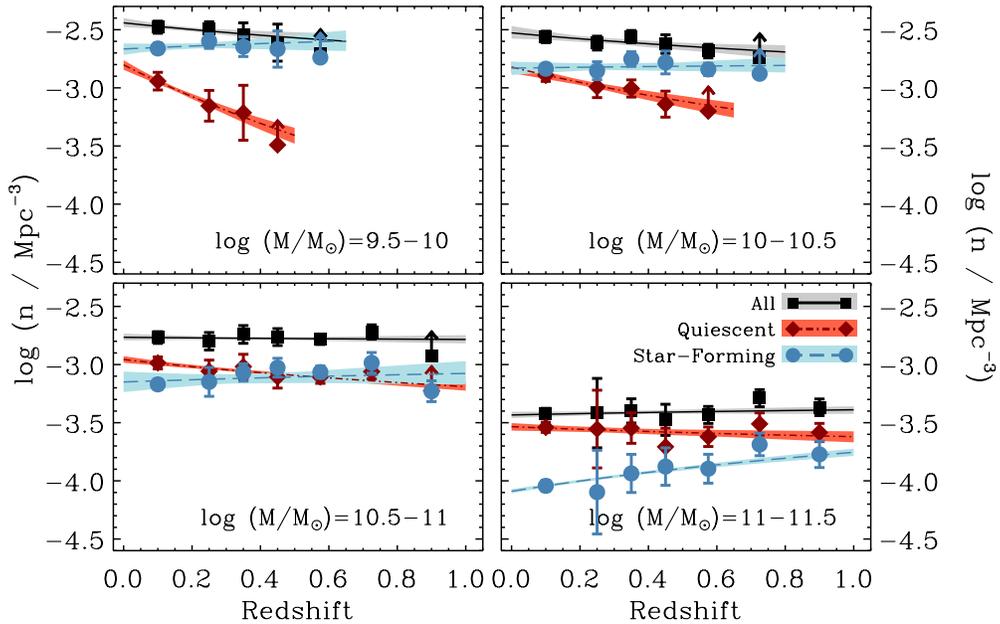
Figure 12. Evolution in the number density of all (black squares), quiescent (red diamonds), and star-forming (blue points) galaxies in four 0.5 dex wide intervals of stellar mass ranging from $10^{9.5}–10^{10} \mathcal{M}_\odot$ in the upper-left panel, to $10^{11}–10^{11.5} \mathcal{M}_\odot$ in the lower-right panel. The error bar on each measurement is due to the quadrature sum of the Poisson and sample variance uncertainties in each redshift interval; we denote lower limits on the number density using upward-pointing arrows. The solid black, dot-dashed red, and dashed blue lines show weighted linear least-squares fits to the data, and the corresponding shaded regions show the 1σ range of power-law fits drawn from the full covariance matrix. We find a factor of ~ 2–3 increase in the number density of $\sim 10^{9.5}–10^{10.5} \mathcal{M}_\odot$ quiescent galaxies since $z \approx 0.5$, and a remarkably little change ($-8\% \pm 10\%$) in the space density of star-forming galaxies over the same range of stellar mass and redshift. Between $10^{10.5}–10^{11} \mathcal{M}_\odot$, the space density of quiescent galaxies increases by $58\% \pm 9\%$, while the number density of star-forming galaxies declines by $-13\% \pm 23\%$. Meanwhile, above $10^{11} \mathcal{M}_\odot$ we find a steep $54\% \pm 7\%$ decline in the number of massive star-forming galaxies since $z \approx 1$, and a small increase ($22\% \pm 12\%$) in the space density of comparably massive quiescent galaxies. The distinct evolutionary trends exhibited by star-forming and quiescent galaxies conspire to keep the number density of *all* galaxies relatively constant over the range of stellar masses and redshifts probed by PRIMUS.

(A color version of this figure is available in the online journal.)

we find that the number density of $10^{9.5}–10^{10} \mathcal{M}_\odot$ quiescent galaxies increases significantly toward lower redshift, by a factor of 3.2 ± 0.5 since $z = 0.4$, whereas the number density of star-forming galaxies decreases marginally, by $-10\% \pm 15\%$ over the same redshift range. Meanwhile, the number density of $10^{10}–10^{10.5} \mathcal{M}_\odot$ quiescent galaxies increases by a factor of 2.2 ± 0.4 since $z = 0.6$, while the number of comparably massive star-forming galaxies changes by $-4\% \pm 15\%$. Finally,

in the $10^{10.5}–10^{11} \mathcal{M}_\odot$ stellar masses bin we find a $58\% \pm 9\%$ increase in the space density of quiescent galaxies since $z = 0.8$, and a $-13\% \pm 23\%$ decrease in the number of star-forming galaxies over the same redshift range. Thus, we find remarkably little change ($-8\% \pm 10\%$) in the number density of $10^{9.5}–10^{10.5} \mathcal{M}_\odot$ star-forming galaxies over the full range of redshifts where PRIMUS is complete, and a gradual, but significant buildup in the population of quiescent galaxies

Table 6
Number and Stellar Mass Density of All, Quiescent, and Star-forming Galaxies

$\langle z \rangle$	$\log(n)$ $(h_{70}^3 \text{ Mpc}^{-3})$			$\log(\rho)$ $(h_{70} \, \mathcal{M}_\odot \text{ Mpc}^{-3})$		
	$9.5 < \log(\mathcal{M}/\mathcal{M}_\odot) < 10$					
	All	Q[a]	SF[a]	All	Q	SF
0.100	-2.48 ± 0.05	-2.94 ± 0.07	-2.66 ± 0.04	7.28 ± 0.05	6.83 ± 0.07	7.10 ± 0.04
0.250	-2.49 ± 0.03	-3.15 ± 0.04	-2.60 ± 0.03	7.27 ± 0.03	6.63 ± 0.05	7.16 ± 0.03
0.350	-2.54 ± 0.09	-3.21 ± 0.16	-2.65 ± 0.07	7.24 ± 0.08	6.58 ± 0.13	7.13 ± 0.06
0.450	-2.61 ± 0.15	> -3.49	-2.67 ± 0.14	7.16 ± 0.13	> 6.33	7.10 ± 0.12
0.575	> -2.71	$\dots$	> -2.74	> 7.06	$\dots$	> 7.02
	$10 < \log(\mathcal{M}/\mathcal{M}_\odot) < 10.5$					
	All	Q	SF	All	Q	SF
0.100	-2.56 ± 0.05	-2.89 ± 0.05	-2.84 ± 0.04	7.71 ± 0.05	7.39 ± 0.05	7.42 ± 0.04
0.250	-2.62 ± 0.03	-2.99 ± 0.05	-2.85 ± 0.04	7.65 ± 0.03	7.29 ± 0.04	7.39 ± 0.04
0.350	-2.56 ± 0.04	-3.01 ± 0.04	-2.75 ± 0.04	7.71 ± 0.03	7.28 ± 0.04	7.51 ± 0.04
0.450	-2.62 ± 0.04	-3.14 ± 0.07	-2.78 ± 0.03	7.65 ± 0.04	7.16 ± 0.05	7.47 ± 0.04
0.575	-2.68 ± 0.05	> -3.20	-2.84 ± 0.04	7.60 ± 0.05	> 7.12	7.42 ± 0.04
0.725	> -2.74	$\dots$	> -2.88	> 7.56	$\dots$	> 7.40
	$10.5 < \log(\mathcal{M}/\mathcal{M}_\odot) < 11$					
	All	Q	SF	All	Q	SF
0.100	-2.77 ± 0.05	-2.99 ± 0.05	-3.17 ± 0.04	7.97 ± 0.05	7.76 ± 0.05	7.55 ± 0.04
0.250	-2.80 ± 0.04	-3.06 ± 0.04	-3.15 ± 0.07	7.93 ± 0.04	7.70 ± 0.04	7.55 ± 0.09
0.350	-2.74 ± 0.06	-3.02 ± 0.09	-3.07 ± 0.04	7.99 ± 0.06	7.73 ± 0.08	7.66 ± 0.04
0.450	-2.76 ± 0.06	-3.11 ± 0.06	-3.03 ± 0.06	7.97 ± 0.06	7.64 ± 0.06	7.69 ± 0.06
0.575	-2.78 ± 0.03	-3.11 ± 0.04	-3.06 ± 0.03	7.96 ± 0.03	7.65 ± 0.04	7.66 ± 0.03
0.725	-2.72 ± 0.05	-3.06 ± 0.04	-2.99 ± 0.07	8.03 ± 0.05	7.70 ± 0.04	7.75 ± 0.07
0.900	> -2.93	> -3.23	-3.23 ± 0.07	> 7.84	> 7.56	7.52 ± 0.08
	$11 < \log(\mathcal{M}/\mathcal{M}_\odot) < 11.5$					
	All	Q	SF	All	Q	SF
0.100	-3.42 ± 0.04	-3.54 ± 0.04	-4.04 ± 0.04	7.74 ± 0.04	7.63 ± 0.04	7.09 ± 0.04
0.250	-3.42 ± 0.20	-3.55 ± 0.24	-4.10 ± 0.17	7.75 ± 0.21	7.60 ± 0.27	7.03 ± 0.28
0.350	-3.40 ± 0.04	-3.55 ± 0.06	-3.94 ± 0.03	7.76 ± 0.04	7.62 ± 0.07	7.20 ± 0.05
0.450	-3.48 ± 0.10	-3.71 ± 0.11	-3.88 ± 0.09	7.68 ± 0.12	7.45 ± 0.12	7.27 ± 0.10
0.575	-3.43 ± 0.04	-3.62 ± 0.04	-3.90 ± 0.07	7.74 ± 0.05	7.56 ± 0.04	7.25 ± 0.08
0.725	-3.29 ± 0.05	-3.51 ± 0.05	-3.69 ± 0.05	7.88 ± 0.05	7.66 ± 0.06	7.47 ± 0.05
0.900	-3.37 ± 0.05	-3.58 ± 0.03	-3.77 ± 0.08	7.81 ± 0.05	7.59 ± 0.04	7.40 ± 0.07

Note. [a] Q = quiescent; SF = star-forming.

toward low redshift. Moreover, we find that the *rate* at which the quiescent galaxy population builds up toward low redshift increases steeply with *decreasing* stellar mass.

Among the most massive galaxies in our sample, however, Figure 12 reveals a striking inversion of the trends seen at lower stellar mass. Between 10^{11}–$10^{11.5} \, \mathcal{M}_\odot$ the number density of quiescent galaxies increases by $22\% \pm 12\%$ since $z \approx 1$, while the number of massive star-forming galaxies *declines* by $54\% \pm 7\%$ over the same redshift range. The reason this destruction of massive star-forming galaxies (and presumed transformation into quiescent systems) does not significantly affect the space density of massive quiescent galaxies is because quiescent galaxies vastly outnumber star-forming galaxies above $\sim 10^{11} \, \mathcal{M}_\odot$ at all redshifts from $z = 0$–1. For example, at $z = 1$ quiescent galaxies outnumber 10^{11}–$10^{11.5} \, \mathcal{M}_\odot$ star-forming galaxies by ≈ 0.13 dex ($\approx 35\%$); therefore, the $\approx 55\%$ decline in the number of massive star-forming galaxies can easily be subsumed into the quiescent galaxy population by the current epoch.

Reviewing Figures 10–12, it is now clear why the SMF for the global population of galaxies (Figures 8 and 9) evolves so little

since $z \approx 1$ over the range of stellar masses where PRIMUS is complete. Between $10^{9.5}$–$10^{10.5} \, \mathcal{M}_\odot$ the SMF is dominated by star-forming galaxies, whose number density remains relatively constant. Meanwhile, among $\mathcal{M} \gtrsim 10^{10.5} \, \mathcal{M}_\odot$ galaxies the SMF becomes increasingly dominated by quiescent galaxies, whose number density *also* remains roughly constant with redshift. Consequently, the bimodal nature of the galaxy SMF combined with the distinct evolutionary trends exhibited by star-forming and quiescent galaxies conspire to keep the SMF for the global population of galaxies from changing significantly at these redshifts.

In Section 5.2.1 we found hints of differential evolution in the SMF of all galaxies based on stellar mass-threshold samples, but the results were not very significant. Do we find more significant evidence for mass assembly downsizing based on the number densities derived within fixed-interval bins of stellar mass? Our power-law fits to the black squares in Figure 12 (see also Table 7) indicate a $28\% \pm 11\%$ increase in the space density of all $10^{9.5}$–$10^{10} \, \mathcal{M}_\odot$ galaxies since $z = 0.4$, and a $35\% \pm 14\%$ increase in the number density of 10^{10}–$10^{10.5} \, \mathcal{M}_\odot$ galaxies since $z = 0.6$. By contrast, among $10^{10.5}$–$10^{11} \, \mathcal{M}_\odot$

Table 7
Power-law Fits to the Number and Stellar Mass Density Evolution[a]

Sample[a]	$\log(n_0)$[b]	γ[b]	$\log(\rho_0)$[c]	β[c]
	$9.5 < \log(\mathcal{M}/\mathcal{M}_\odot) < 10$			
All	-2.441 ± 0.03	-0.729 ± 0.328	7.319 ± 0.03	-0.663 ± 0.294
Q	-2.802 ± 0.03	-3.444 ± 0.441	6.957 ± 0.04	-3.150 ± 0.514
SF	-2.666 ± 0.04	0.317 ± 0.445	7.091 ± 0.03	0.351 ± 0.400
	$10 < \log(\mathcal{M}/\mathcal{M}_\odot) < 10.5$			
All	-2.527 ± 0.04	-0.644 ± 0.318	7.735 ± 0.04	-0.576 ± 0.313
Q	-2.821 ± 0.03	-1.668 ± 0.363	7.456 ± 0.03	-1.551 ± 0.326
SF	-2.830 ± 0.04	0.090 ± 0.326	7.419 ± 0.04	0.168 ± 0.339
	$10.5 < \log(\mathcal{M}/\mathcal{M}_\odot) < 11$			
All	-2.766 ± 0.02	-0.062 ± 0.145	7.968 ± 0.02	-0.037 ± 0.130
Q	-2.956 ± 0.02	-0.775 ± 0.144	7.786 ± 0.02	-0.699 ± 0.132
SF	-3.150 ± 0.06	0.245 ± 0.390	7.559 ± 0.05	0.344 ± 0.347
	$11 < \log(\mathcal{M}/\mathcal{M}_\odot) < 11.5$			
All	-3.433 ± 0.02	0.148 ± 0.124	7.730 ± 0.02	0.189 ± 0.123
Q	-3.534 ± 0.02	-0.285 ± 0.168	7.641 ± 0.02	-0.297 ± 0.174
SF	-4.090 ± 0.01	1.114 ± 0.100	7.036 ± 0.01	1.274 ± 0.109

Notes.
[a] Q = quiescent; SF = star-forming.
[b] Model given by $n(z) = n_0(1 + z)^\gamma$ with n in h_{70}^3 Mpc^{-3}.
[c] Model given by $\rho(z) = \rho_0(1 + z)^\beta$ with ρ in h_{70} $\mathcal{M}_\odot$ Mpc^{-3}.

galaxies the number density increases by $4\% \pm 9\%$ since $z = 0.8$, and declines by $-10\% \pm 9\%$ for 10^{11}–$10^{11.5}$ $\mathcal{M}_\odot$ galaxies since $z = 1$. Thus, we *do* find evidence for mass assembly downsizing—a continued buildup of the low- and intermediate-mass galaxy population toward low redshift, and no significant changes in the space density of massive galaxies—within the global galaxy population. However, with the benefit of hindsight we now see that these relatively subtle evolutionary trends are being driven entirely by the much more significant evolutionary trends separately exhibited by the population of quiescent and star-forming galaxies.

To summarize, we have shown that the evolution of the SMFs of both quiescent and star-forming galaxies depends sensitively on stellar mass. Above $\mathcal{M} \sim 10^{11} \mathcal{M}_\odot$ quiescent galaxies dominate the galaxy population at all redshifts, and their number density changes relatively little since $z = 1$, whereas the number of star-forming galaxies declines precipitously toward lower redshift. Between $10^{9.5}$–$10^{10.5}$ $\mathcal{M}_\odot$, on the other hand, star-forming galaxies vastly outnumber quiescent galaxies, and their number density changes by just $-8\% \pm 10\%$ between $z \approx 0.6$ and $z \approx 0$. Meanwhile, the number of $10^{9.5}$–$10^{10.5}$ $\mathcal{M}_\odot$ quiescent galaxies increases significantly since $z \approx 0.6$ at a rate that accelerates with decreasing stellar mass. Finally, the stellar mass range between $10^{10.5}$–10^{11} $\mathcal{M}_\odot$ marks the transition regime between the dominance of star-forming galaxies and the rise of quiescent galaxies at low mass, and the dominance of quiescent galaxies and the decline of the star-forming population at large stellar mass.

5.3. Comparison with Previous Studies

A detailed quantitative comparison of our results against previous studies is challenging for several reasons. First, previous studies have used a wide variety of techniques to divide the galaxy population into "quiescent" and "star-forming" galaxies; however, many of these techniques result in a quiescent population that is highly contaminated by dusty star-forming galaxies (e.g., Maller et al. 2009; Zhu et al. 2011), which can severely bias the inferred SMF in mass-dependent ways. Second, systematic differences in stellar mass estimates due to different prior assumptions and population synthesis models can significantly affect the inferred SMF (e.g., Marchesini et al. 2009; Kajisawa et al. 2009; see also Appendix B). And finally, many previous studies have neglected the effects of sample variance, and therefore have underestimated the statistical uncertainties of their results. Nevertheless, we can still perform a rudimentary comparison of our quiescent and star-forming galaxy SMFs against previous measurements assembled from the literature.

To facilitate this comparison, we recompute our SMFs using four broader redshift bins with $\Delta z = 0.2$ (due to the typically smaller area and sample size of these analyses) centered on $\langle z \rangle = 0.3$, 0.5, 0.7, and 0.9. In Figure 13 we plot the SMFs for (top row) quiescent and (bottom row) star-forming galaxies from PRIMUS as a tan shaded region, reflecting the quadrature sum of the Poisson and sample variance uncertainties in each redshift bin. We compare these results to the SMFs published by Borch et al. (2006; red triangles), Drory et al. (2009; purple diamonds), Pozzetti et al. (2010; blue squares), and Ilbert et al. (2010; orange crosses), accounting for differences in the adopted Hubble constant and IMF. For reference, the SMFs published by Drory et al. (2009), Ilbert et al. (2010), and Pozzetti et al. (2010) are all based on the $\sim$2 deg^2 COSMOS field, while Borch et al. (2006) analyzed the three COMBO-17 (Wolf et al. 2003) fields, totaling $\sim$0.8 deg^2.

Examining Figure 13, we find reasonably good agreement between our SMFs and the literature, modulo expected differences due to sample variance in PRIMUS (see, e.g., Figure 7) and the other reasons outlined above. Among the largest discrepancies are in the $\langle z \rangle = 0.5$ and $\langle z \rangle = 0.7$ redshift bins for quiescent galaxies, which shows that our SMF agrees with the SMFs derived by Borch et al. (2006) and Pozzetti et al. (2010), but
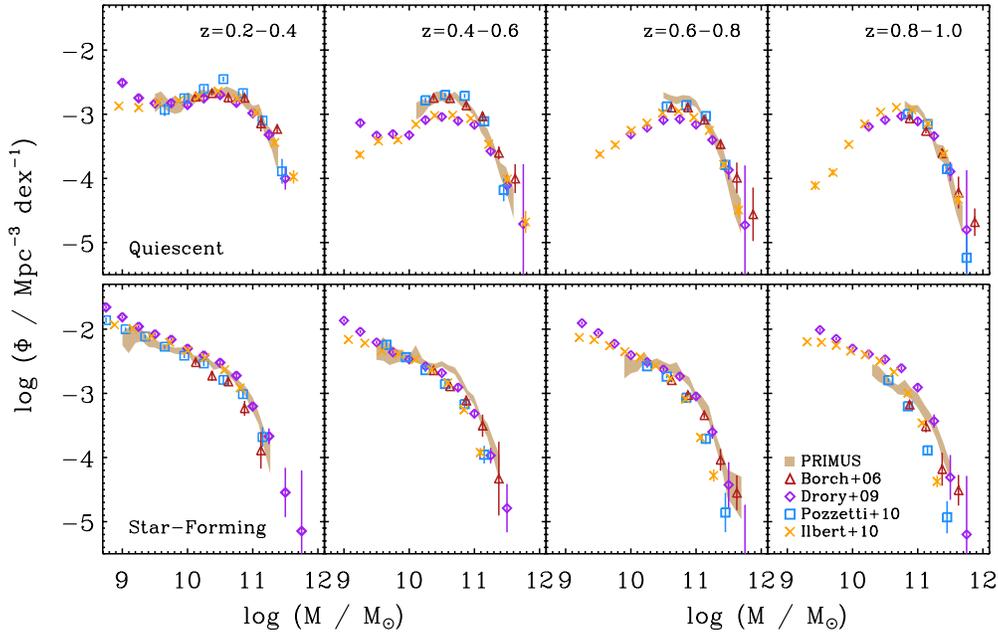
Figure 13. Comparison of the SMFs for (top row) quiescent and (bottom row) star-forming galaxies in four redshift bins from $z = 0.2–1.0$ against previously measured SMFs assembled from the literature. We find that our SMFs are generally consistent with these previous studies.

(A color version of this figure is available in the online journal.)

disagrees noticeably with the Drory et al. (2009) and Ilbert et al. (2010) SMFs. We also find a somewhat higher number density of $\sim 10^{10.5}$–10^{11} $\mathcal{M}_\odot$ star-forming galaxies at $\langle z \rangle = 0.5$. Overall, however, we conclude that our results are consistent with previous measurements of the SMF at intermediate redshift.

6. DISCUSSION

We have measured the evolution of the SMF since $z \approx 1$ of quiescent and star-forming galaxies using PRIMUS, one of the largest spectroscopic surveys of intermediate-redshift galaxies ever conducted. Our goals have been to characterize the stellar mass growth of each population, and to measure the rate at which star-forming galaxies are being quenched as a function of stellar mass and redshift. Compared to many previous studies, our analysis has benefited from a large, statistically complete sample of faint galaxies ($\sim$40,000 galaxies to $i \approx 23$) spread across five widely separated fields totaling $\approx$5.5 deg^2, and a well-defined local SDSS-*GALEX* comparison sample. With these data, we have been able to study the detailed evolution of the SMF over a large dynamic range of stellar mass and redshift in a consistent way, with well-quantified sample variance uncertainties.

We find that the evolution of the SMFs of both quiescent and star-forming galaxies depends acutely on stellar mass, but in very different ways (see Figure 12). Among quiescent galaxies, the number of intermediate-mass ($\sim 10^{10}$ $\mathcal{M}_\odot$) galaxies increases by a factor of $\sim$2–3 since $z \approx 0.5$, but remains approximately constant for massive ($\gtrsim 10^{11}$ $\mathcal{M}_\odot$) galaxies since $z \approx 1$. By contrast, the most significant evolutionary trends for star-forming galaxies occur above $\sim 10^{11}$ $\mathcal{M}_\odot$. Specifically, we find no significant change in the number density of intermediate-mass galaxies, and a $\approx$55% *decrease* in the number of massive star-forming galaxies since $z \approx 1$.

These galaxy-type dependent trends conspire rather remarkably to make the SMF for the global galaxy population *appear* to not have changed significantly since $z \approx 1$, at least over the range of stellar masses and redshifts probed by PRIMUS (Figure 8). One implication of these results is that an analysis

of the global galaxy population by itself would yield a highly incomplete view of galaxy evolution because it would mask the rich interplay between the coevolution of star-forming and quiescent galaxies.

In the next two sections we synthesize our results to investigate the effect of mergers on the stellar mass growth of galaxies, and to quantify the stellar mass dependence of star formation quenching from $z = 0$–1.

6.1. Constraints on the Stellar Mass Growth of Galaxies by Mergers

The stellar mass of an individual galaxy can change by forming new stars, or by merging with other galaxies. By accounting for the stellar mass growth of galaxies by in situ star formation, the redshift evolution of the SMF (i.e., the derivative of the SMF with respect to cosmic time) in principal can be used to constrain the growth of galaxies by mergers (e.g., Drory & Alvarez 2008; Walcher et al. 2008; Conroy & Wechsler 2009; Pozzetti et al. 2010).

Our finding that the SMF of the global galaxy population evolves relatively little between $z \approx 1$ and $z \approx 0$ (see Figure 8) suggests that mergers play a subdominant role for the stellar mass growth of galaxies at these redshifts. To quantify this result, we use the measured SFR of each galaxy (see Section 4.1) to estimate how much their stellar mass will increase by in situ star formation. Specifically, we compute for each galaxy of a given stellar mass, $\mathcal{M}$, a new stellar mass, $\mathcal{M}'$, given by

$$\mathcal{M}'(z') = \mathcal{M}(z) + (1 - \mathcal{R}) \times (\psi \Delta t), \quad (11)$$

where $\mathcal{R}$ is the *return fraction*, the stellar mass returned (assumed instantaneously) to the interstellar medium by supernovae and stellar winds, ψ is the SFR in $\mathcal{M}_\odot$ yr^{-1}, and $\Delta t \equiv t(z') - t(z)$ is the elapsed cosmic time (increase in the age of the universe) in years between redshift z and z', where $z' < z$. We adopt $\mathcal{R} \approx 0.5$, which is appropriate for the Chabrier (2003) IMF (Leitner & Kravtsov 2011), and make the simplifying assumption that the SFR is constant over the time

interval Δt. Although the SFRs of most star-forming galaxies at these redshifts are declining with decreasing redshift (see, e.g., Figure 1; Noeske et al. 2007), Δt in our analysis is sufficiently short ($\lesssim 1$ Gyr) for all but the last redshift bin (where $\Delta t \approx 1.6$ Gyr), that incorporating a more detailed star formation history (SFH) into our calculation would not significantly change our results. Moreover, recall that our UV-based SFRs trace star formation over the last ~ 100 Myr, which is reasonably well matched to the Δt timescale.

Using this formalism, we can use the *observed* SMF at redshift z to *predict* what the SMF will look like at a (lower) redshift z' if galaxies grow by star formation alone (i.e., assuming mergers do not occur). Note that although in situ star formation conserves the *total* number of galaxies, the number of galaxies of a given stellar mass can increase or decrease because the SFR varies with stellar mass (see, e.g., Figure 1). After controlling for star formation growth, any residual change in the number density of galaxies of a given stellar mass must be due to merging. We emphasize that our measurement complements, but is only implicitly related to measurements of the major and minor *merger rate* (see, e.g., Lotz et al. 2011, and references therein). For example, the technique we use only reveals whether mergers have a *net* effect on the SMF, but cannot be used to infer the underlying stellar mass distribution of galaxies that are merging (see Drory & Alvarez 2008 for more details). Another caveat regarding this technique is its implicit assumption that mergers retain *all* the stellar mass involved in the merger, when it is likely that a non-negligible fraction of that mass is dispersed to large radii to form the diffuse stellar component (DSC) of groups and clusters (e.g., Murante et al. 2007). In fact, our precise measurement of the evolution of the SMF above $\sim 10^{11}\,\mathcal{M}_\odot$ could be turned around to help constrain this fraction in the context of the cosmological growth of dark-matter halos (e.g., Monaco et al. 2006; Behroozi et al. 2012).

With the preceding discussion in mind, we define the fractional *merger growth rate*, $\mathcal{G}(\mathcal{M}, z)$, as

$$\mathcal{G}(\mathcal{M}, z) \equiv \frac{1}{n}\frac{\Delta n}{\Delta t}\bigg|_{\text{mergers}} = \frac{1}{\Delta t(z, z')}\left[1 - \frac{n^{\text{pred}}(\mathcal{M}, z)}{n^{\text{obs}}(\mathcal{M}, z)}\right],$$
(12)

where n^{obs} and n^{pred} are the observed (measured) and predicted number density of galaxies at redshift z, respectively, and Δt is in Gyr. We divide by the observed number density to account for the shape of the SMF; for example, a merger-induced absolute increase in number density of 10^{-3} galaxies Mpc^{-3} Gyr^{-1} will have a much larger fractional effect on the exponential tail of the SMF relative to the low-mass end, where such a change would be negligible. We derive the number densities in Equation (12) as in Section 5.2 by numerically integrating the observed and predicted SMFs over chosen intervals of stellar mass, but use the best-fitting single or double Schechter model to extrapolate to lower or higher mass as needed. Note that $\mathcal{G}$ can be either positive or negative depending on whether mergers result in a net increase or decrease of galaxies of a certain stellar mass. Moreover, $\mathcal{G} \approx 0$ does not *necessarily* indicate that mergers are not occurring or important; mergers could result in a small value of $\mathcal{G}$ if the growth and destruction of galaxies into and out of a certain stellar mass bin on average balanced one another.

In Figure 14 we plot $\mathcal{G}$ versus redshift in four intervals of stellar mass between $10^{9.5}$–$10^{11.5}\,\mathcal{M}_\odot$. Qualitatively, we find no significant variations of $\mathcal{G}$ with either stellar mass or redshift (where PRIMUS is complete). Quantitatively, we find a net change in the number density of $10^{9.5}$–$10^{10.5}\,\mathcal{M}_\odot$ galaxies
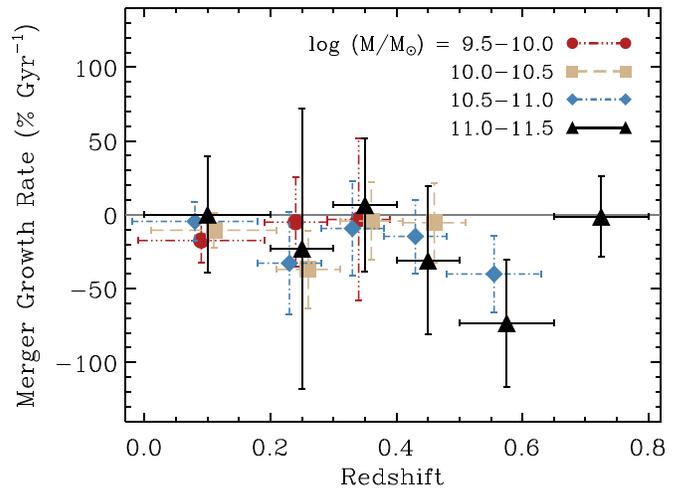
Figure 14. Merger growth rate, $\mathcal{G}(\mathcal{M}, z)$, the fractional change in the number density of galaxies due to mergers after accounting for stellar mass growth by in situ star formation, vs. redshift in four 0.5 dex wide intervals of stellar mass between $10^{9.5}\,\mathcal{M}_\odot$ and $10^{11.5}\,\mathcal{M}_\odot$. Note that $\mathcal{G}$ as defined by Equation (12) can be either negative or positive depending on whether mergers preferentially destroy or create galaxies of a given stellar mass. We find a net change in the number density of $10^{9.5}$–$10^{10.5}\,\mathcal{M}_\odot$ galaxies of $-13\% \pm 9\%$ Gyr^{-1} from $z \approx 0$ to $z \approx 0.5$, and a change of $-14\% \pm 18\%$ Gyr^{-1} in the number density of $10^{10.5}$–$10^{11.5}\,\mathcal{M}_\odot$ galaxies since $z \approx 0.8$. In other words, although mergers are almost certainly occurring, they do not have a large *net* effect on the SMF over this range of stellar masses and redshifts.

(A color version of this figure is available in the online journal.)

of $-13\% \pm 9\%$ Gyr^{-1} from $z \approx 0$ to $z \approx 0.5$, and a change of $-14\% \pm 18\%$ Gyr^{-1} in the number density of $10^{10.5}$–$10^{11.5}\,\mathcal{M}_\odot$ galaxies since $z \approx 0.8$. Although the uncertainties are significant, we conclude, therefore, that mergers do not appear to be an important channel for stellar mass growth at late cosmic times, even among massive ($\gtrsim 10^{11}\,\mathcal{M}_\odot$) galaxies (see also Pozzetti et al. 2010). Although beyond the scope of the present study, a detailed comparison of these results with theoretical galaxy formation models, which generally find that massive galaxies grow much more substantially through mergers at $z < 1$ (e.g., De Lucia et al. 2006; Cattaneo et al. 2008, 2011), would be very interesting.

We extend our analysis further by separately considering the stellar mass growth of quiescent and star-forming galaxies. One particularly important question we would like to address is whether quiescent galaxies grow significantly by dissipationless mergers (also known as *dry mergers*) at $z < 1$. To investigate this question we measure the redshift evolution of $\mathcal{M}_c$, the stellar mass at fixed cumulative number density, $n(\mathcal{M} > \mathcal{M}_c)$. To a good approximation, both star formation and mergers will increase $\mathcal{M}_c$ without changing the number density, while the transformation of one galaxy type into another (e.g., due to star formation quenching) will tend to decrease $\mathcal{M}_c$ at a given cumulative number density (van Dokkum et al. 2010; Brammer et al. 2011). Because the amount of in situ star formation in our sample of quiescent galaxies is by construction negligible (see Figure 1), an increase in $\mathcal{M}_c$ with decreasing redshift can be attributed to dissipationless mergers.

In Figure 15 we plot $\mathcal{M}_c$ versus redshift for quiescent (hatched red shading) and star-forming (light blue shading) galaxies corresponding to $n(\mathcal{M} > \mathcal{M}_c) = 10^{-3.5}$ Mpc^{-3}. We choose this number density threshold because it samples a significant fraction of the exponential tail of the SMF at each redshift, and because PRIMUS is complete to both galaxy types
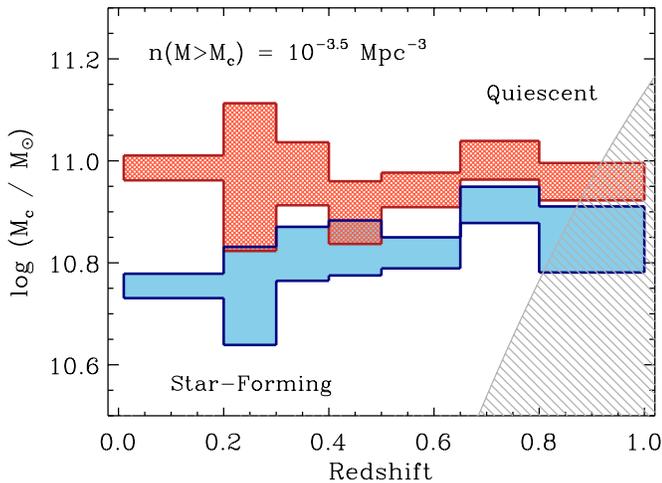
Figure 15. Stellar mass, $\mathcal{M}_c$, at which the cumulative number density, $n(\mathcal{M} > \mathcal{M}_c)$, equals $10^{-3.5}$ Mpc^{-3} vs. redshift. The red and blue shaded regions correspond to quiescent and star-forming galaxies, respectively, and the gray hatched area indicates for reference the stellar mass completeness limit for quiescent galaxies; the completeness limit for star-forming galaxies extends to much lower stellar mass. The constancy of $\mathcal{M}_c$ for quiescent galaxies indicates negligible growth of this population due to mergers, while the decline in $\mathcal{M}_c$ with decreasing redshift reflects the progressive quenching and transformation of massive star-forming galaxies into quiescent galaxies from $z = 0$–1.

(A color version of this figure is available in the online journal.)

all the way to $z \approx 1$. For reference, the gray shaded region in the lower-right corner of Figure 15 shows the stellar mass completeness limit for quiescent galaxies (the stellar mass limit for star-forming galaxies is much lower). In each redshift bin, our measurement of $\mathcal{M}_c$ reflects the quadrature sum of both the Poisson and sample variance uncertainties.

We find no notable change in $\mathcal{M}_c$ for quiescent galaxies from $z = 0$–1, and a significant decrease for star-forming galaxies with decreasing redshift. Modeling the observed trends as a power-law function of redshift, $\mathcal{M}_c \propto (1 + z)^q$, we find $q = -0.09 \pm 0.16$ for quiescent galaxies, and $q = 0.60 \pm 0.17$ for star-forming galaxies. In other words, $\mathcal{M}_c$ for star-forming galaxies decreases on average by 0.18 ± 0.05 dex ($51\% \pm 12\%$) since $z = 1$, whereas $\mathcal{M}_c$ for quiescent galaxies is constant to within ± 0.05 dex ($\pm 12\%$) over the same redshift range.

The decline in $\mathcal{M}_c$ for star-forming galaxies is most likely due to the progressive transformation of massive star-forming galaxies into quiescent, passively evolving systems toward low redshift (see Figure 12 and Section 6.2). In essence, $\mathcal{M}_c$ decreases toward low redshift because we have to integrate further down the SMF to count the same total number of galaxies. Meanwhile, the constancy of $\mathcal{M}_c$ for quiescent galaxies follows directly from the lack of evolution at the massive end of the SMF. Note that $\mathcal{M}_c$ for quiescent galaxies remains approximately constant even though star-forming galaxies are being quenched because massive star-forming galaxies constitute a very small fraction of the total number of massive galaxies at $z = 0$–1 (see Section 5.2.2). We conclude, therefore, that most massive, quiescent galaxies are fully assembled by $z \approx 1$, and do not appear to grow significantly by dissipationless mergers over the last ~ 8 billion years of cosmic time.

6.2. Buildup of the Quiescent Galaxy Population by Star Formation Quenching

Our analysis of the SMF has revealed significant changes in the population of both quiescent and star-forming galaxies.

The two key results we focus on in this section are the rapid rise in the number of intermediate-mass ($\sim 10^{10} \mathcal{M}_\odot$) quiescent galaxies since $z \approx 0.5$, and the steep decline in the population of massive ($\gtrsim 10^{11} \mathcal{M}_\odot$) star-forming galaxies since $z \approx 1$. Taken together, these results indicate that quenching—the rapid cessation of star formation in galaxies—is an important driver of galaxy evolution at $z < 1$. Moreover, whatever mechanism or mechanisms are responsible for quenching must affect galaxies spanning a wide range of stellar mass at these redshifts.

We can use the results presented in Section 5 to quantify both the *quenching rate*—the frequency with which star-forming galaxies are being transformed into quiescent galaxies—and the stellar mass growth of the quiescent galaxy population due to the addition of newly quenched galaxies. The evolution with redshift of both these quantities should place important constraints on the broad range of proposed quenching processes, and their implementation into theoretical galaxy formation models.

In the subsequent analysis we make the simplifying but well-motivated assumption (see Section 6.1) that we can neglect the effects of mergers. More specifically, we implicitly assume that if mergers are taking place, they do not cause a significant number of galaxies to shift from one 0.5 dex wide stellar mass bin to another (e.g., from the 10^{10}–$10^{10.5} \mathcal{M}_\odot$ to the $10^{10.5}$–$10^{11} \mathcal{M}_\odot$ stellar mass bin). Consequently, although we do not explicitly include their potential contribution, mergers could still be a viable means of quenching star formation in some galaxies. In addition, we implicitly ignore in situ star formation within the quiescent galaxy population, which by design is negligible (see Figure 1).

With the preceding caveats in mind, we define the fractional quenching rate as $F_{\text{quench}} \equiv (dn_Q/dt)/n_{\text{SF}}$, or the fraction of star-forming galaxies that must be quenched per Gyr as a function of stellar mass and redshift in order to account for the measured evolution of the quiescent-galaxy population with decreasing redshift. Using Equation (9), we obtain

$$F_{\text{quench}} = \gamma_Q \left(\frac{n_{0,Q}}{n_{0,\text{SF}}} \right) (1 + z)^{\gamma_Q - \gamma_{\text{SF}} - 1} \left(\frac{dt}{dz} \right)^{-1}, \quad (13)$$

where the Q and SF subscripts refer to quiescent and star-forming galaxies, respectively, and the relevant coefficients and uncertainties are listed in Table 7. The (dt/dz) term is the derivative of the age-redshift function, $t(z)$, where t is the age of the universe (Hogg 1999). For convenience, we note that in our adopted cosmology (dt/dz) can be approximated from $0 < z < 1$ to an accuracy of better than 0.5% by a third-order polynomial of the form $(dt/dz) \approx -13.8835 + 19.3598z - 13.621z^2 + 4.2141z^3$ Gyr^{-1}.

In Figure 16 we plot F_{quench} versus redshift in four bins of stellar mass between $10^{9.5}$–$10^{11.5} \mathcal{M}_\odot$. This figure reveals several interesting results. First, we find that F_{quench} is relatively small at all redshifts and stellar masses; it varies between $\approx 5\%$–10% Gyr^{-1}, except in the lowest stellar mass bin at $z \lesssim 0.2$, where it rises to $\approx 12\%$–18% Gyr^{-1}. For comparison, Blanton (2006) estimates that roughly 25% of blue star-forming galaxies must be quenched since $z \approx 1$ in order to match the measured buildup of the optical luminosity function for red-sequence galaxies. Second, although the uncertainties are large, our measurements suggest that F_{quench} varies systematically with stellar mass. Among $> 10^{11} \mathcal{M}_\odot$ galaxies, we find a typical quenching rate of $\approx 5\%$ Gyr^{-1}, whereas among $\lesssim 10^{10.5} \mathcal{M}_\odot$ galaxies the rate is around $\approx 7\%$–15% Gyr^{-1}, a factor of ~ 2–3
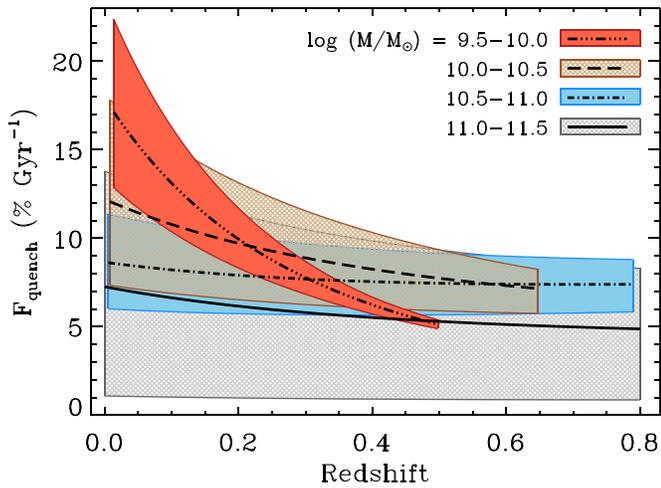
Figure 16. Fractional quenching rate F_{quench} vs. redshift in four intervals of stellar mass between $10^{9.5}$–$10^{11.5}$ $\mathcal{M}_\odot$. F_{quench} is the proportion of star-forming galaxies in a given stellar mass interval that must be quenched per Gyr in order to match the measured evolution in the number density of quiescent galaxies. Although we implicitly ignore the effects of mergers in calculating F_{quench}, that does not necessarily mean that mergers are not responsible for quenching star formation in some galaxies (see the discussion in Section 6.2). Although the uncertainties are large, we find that F_{quench} is typically a factor of ~2–3 higher for $10^{9.5}$–$10^{10.5}$ $\mathcal{M}_\odot$ galaxies compared to more massive galaxies $\gtrsim 10^{11}$ $\mathcal{M}_\odot$. Moreover, the fractional quenching rate in lower-mass systems appears to be increasing toward the current epoch.

(A color version of this figure is available in the online journal.)

higher. Finally, Figure 16 suggests that F_{quench} *increases* toward low redshift among lower-mass galaxies. Specifically, we find a weak trend of an increasing F_{quench} toward $z \approx 0$ among 10^{10}–$10^{10.5}$ $\mathcal{M}_\odot$ galaxies, and a much more significant and rapid rise toward low redshift among $10^{9.5}$–10^{10} $\mathcal{M}_\odot$ galaxies. Although the uncertainties are large, these results suggest that star formation quenching is more prevalent among lower-mass galaxies, and that the fraction of low-mass star-forming galaxies that are being quenched is increasing toward the current epoch.

We can extend this analysis one step further and calculate $\dot{\rho}_{SF\rightarrow Q} \equiv d\rho_Q/dt$, the rate of stellar mass transfer from the population of star-forming to quiescent galaxies, using the measured stellar mass growth of the quiescent-galaxy population. Once again, we implicitly assume that the stellar mass growth of the quiescent population is entirely due to the addition of newly quenched (i.e., previously star-forming) galaxies, and that dissipationless mergers between two quiescent galaxies do not cause a significant number of galaxies to change their stellar mass by more than a factor of three. With these caveats in mind, we use Equation (10) to write $\dot{\rho}_{SF\rightarrow Q}$ in units of $\mathcal{M}_\odot$ yr^{-1} Mpc^{-3} as

$$\dot{\rho}_{SF\rightarrow Q} = \rho_{0,Q} \, \beta_Q \, (1+z)^{\beta_Q - 1} \left(\frac{dt}{dz}\right)^{-1}, \qquad (14)$$

where the relevant coefficients are given in Table 7.

In Figure 17 we plot $\dot{\rho}_{SF\rightarrow Q}$ versus stellar mass in four equal-sized bins of redshift from $z = 0$–0.8. The individual symbols with error bars, which have been offset slightly in the horizontal direction for clarity, correspond to different redshift bins, and the gray shaded region reflects the broad trend we deduce. We find that $\dot{\rho}_{SF\rightarrow Q}$ depends weakly on redshift, but has a very strong stellar mass dependence. Quantitatively, $\dot{\rho}_{SF\rightarrow Q}$ rises from $\approx 1.5 \times 10^{-3}$ $\mathcal{M}_\odot$ yr^{-1} Mpc^{-3} around ~$10^{9.8}$ $\mathcal{M}_\odot$ to a peak value of $\approx 3 \times 10^{-3}$ $\mathcal{M}_\odot$ yr^{-1} Mpc^{-3} around ~$10^{10.8}$ $\mathcal{M}_\odot$.
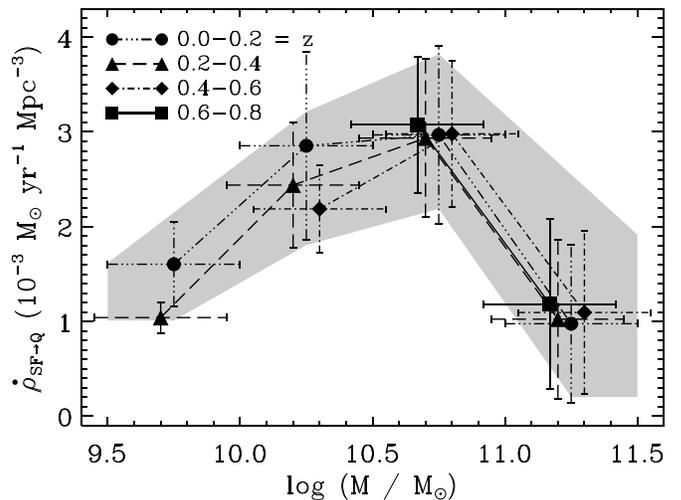
Figure 17. Rate at which stellar mass is being transferred from the star-forming to the quiescent galaxy population, $\dot{\rho}_{SF\rightarrow Q}$, vs. stellar mass in four intervals of redshift between $z = 0$–0.8. The individual symbols with error bars (offset slightly horizontally for clarity) correspond to different redshift bins, and the gray shaded region shows the mean trend and 1σ confidence region over all redshifts. We find that $\dot{\rho}_{SF\rightarrow Q}$ is largely independent of redshift, and peaks around ~$10^{10.8}$ $\mathcal{M}_\odot$. Consequently, although a larger proportion of lower-mass galaxies are being quenched (see Figure 16), the bulk of the stellar mass buildup of the quiescent galaxy population is occurring near the "knee" of the SMF.

Above ~10^{11} $\mathcal{M}_\odot$, $\dot{\rho}_{SF\rightarrow Q}$ declines sharply to a mean value of $\approx 1 \times 10^{-3}$ $\mathcal{M}_\odot$ yr^{-1} Mpc^{-3}.

These results reveal that although fractionally more low- and intermediate-mass (~$10^{9.5}$–$10^{10.5}$ $\mathcal{M}_\odot$) galaxies are being quenched (see Figure 16), the bulk of the stellar-mass buildup within the quiescent galaxy population occurs around ~$10^{10.8}$ $\mathcal{M}_\odot$, near the "knee" of the SMF. As emphasized by Bell et al. (2007), this stellar mass scale appears to be important because both the stellar mass-weighted SFR density in galaxies and the stellar mass growth of the quiescent galaxy population peak around this stellar mass at $z < 1$; however, the underlying physical cause of this coincidence remains unknown.

7. SUMMARY

We have measured the evolution of the SMFs of quiescent and star-forming galaxies from $z = 0$–1 using two large, statistically complete, spectroscopic samples. At low redshift we use a sample of ~170,000 SDSS galaxies with *GALEX*, 2MASS, and *WISE* photometry, and at intermediate redshift we use a sample of ~40,000 galaxies brighter than $i \approx 23$ drawn from PRIMUS with deep *GALEX* and IRAC imaging. Our PRIMUS sample is notable for its depth, sample size, and area, which totals ≈ 5.5 deg^2 over five widely-separated fields, while our SDSS-*GALEX* sample comprises one of the largest statistical samples of local galaxies with SDSS and *GALEX* photometry ever assembled.

The exceptional multi-wavelength coverage of both datasets provides deep UV to mid-infrared imaging over the entire spectroscopic survey area, allowing us to robustly estimate SFRs and stellar masses using a new Bayesian SED-modeling code (iSEDfit; see Appendix A). We use these measurements to separate the galaxy population into quiescent and star-forming based on their position in the SFR-stellar mass diagram, and to measure the evolution of the SMF over a large dynamic range in stellar mass and redshift with relatively small sample variance

and Poisson uncertainties. In addition, we carefully assess the effect of systematic errors in our stellar mass and SFR estimates, and find that the evolutionary trends we measure are broadly insensitive to the exact choice of priors and population synthesis models.

Our principal quantitative results are as follows:

1. We find for the global galaxy population that the SMF has evolved relatively little since $z = 1$, although we do find evidence for differential evolution—mass assembly downsizing. We measure a $31\% \pm 9\%$ increase in the integrated number density of $\sim 10^{10}\,\mathcal{M}_\odot$ galaxies since $z \approx 0.6$, and a $-3\% \pm 6\%$ change in the number density of all $\sim 10^{11}\,\mathcal{M}_\odot$ galaxies since $z \approx 0.9$. Most massive galaxies, therefore, appear to be largely in place by $z = 1$, while lower-mass galaxies continue to assemble toward the present epoch.

2. The relatively subtle changes in the SMF of the global population, however, mask much more dramatic evolution in the SMFs of star-forming and quiescent galaxies. Within the star-forming population the most rapid evolution occurs among massive galaxies, whereas the low-mass end of the star-forming galaxy SMF does not change significantly. We find that the comoving number density of $10^{9.5}$–$10^{11}\,\mathcal{M}_\odot$ star-forming galaxies changes by $-8\% \pm 10\%$ between $z \approx 0.8$ and $z \approx 0.0$, whereas the space density of massive (10^{11}–$10^{11.5}\,\mathcal{M}_\odot$) star-forming galaxies *declines* by $54\% \pm 7\%$ since $z \approx 1$.

3. Meanwhile, among quiescent galaxies the most significant evolutionary changes occur among low- and intermediate-mass ($10^{9.5}$–$10^{10.5}\,\mathcal{M}_\odot$) galaxies, whereas most massive ($\gtrsim 10^{11}\,\mathcal{M}_\odot$) quiescent galaxies are largely in place from $z = 0$–1. Quantitatively, we find a factor of ~ 2–3 increase in the number density of $10^{9.5}$–$10^{10}\,\mathcal{M}_\odot$ galaxies since $z \approx 0.5$, and a marginally significant increase, $22\% \pm 12\%$, in the space density of $> 10^{11}\,\mathcal{M}_\odot$ quiescent galaxies since $z \approx 1$.

We use these measurements to place new constraints on the growth of galaxies by mergers, and to quantify the buildup of the quiescent galaxy population due to star formation quenching as a function of redshift and stellar mass:

1. Using a simple model to account for the expected growth of galaxies due to star formation, we find that mergers do not appear to be a dominant channel for the stellar mass buildup of galaxies at $z < 1$, even among massive ($\gtrsim 10^{11}\,\mathcal{M}_\odot$) systems. Quantitatively, we find that mergers are responsible for a net change in the number density of $10^{9.5}$–$10^{10.5}\,\mathcal{M}_\odot$ galaxies of $-13\% \pm 9\%$ Gyr^{-1} from $z \approx 0$ to $z \approx 0.5$, and a change of $-14\% \pm 18\%$ Gyr^{-1} in the number density of $10^{10.5}$–$10^{11.5}\,\mathcal{M}_\odot$ galaxies since $z \approx 0.8$. These results do not imply that mergers are not occurring, only that they do not have a large *net* effect on the SMF over the range of stellar masses and redshifts probed by PRIMUS.

2. Our results also imply that the rate at which star formation is quenched in galaxies depends both on stellar mass and redshift, with a peak around $\sim 10^{10.8}\,\mathcal{M}_\odot$, and an increase in the quenching rate at lower redshift for lower mass galaxies. In particular, we find that the quenching rate for massive galaxies with $> 10^{11}\,\mathcal{M}_\odot$ is consistently low ($\approx 5\%$ Gyr^{-1}) at all redshifts to $z \approx 1$.

To fully characterize the buildup of stellar mass for all galaxies to $z = 1$, additional measurements at the lower mass end of the SMF are needed, which requires both deeper multi-wavelength imaging and spectroscopy. In addition, while our results at intermediate redshift use a large sample of $\sim 40{,}000$ galaxies across five separate fields covering ≈ 5.5 deg^2, they are still dominated by sample variance. This result argues that even more wide-field imaging and spectroscopy to at least $i = 23$ are needed to precisely measure the SMF from $z = 0$–1.

APPENDIX A

iSEDfit SPECTRAL ENERGY DISTRIBUTION MODELING CODE

A.1. Background

iSEDfit[39] was developed in the IDL programming language to be a fast and flexible tool to extract the physical properties of both nearby and high-redshift galaxies from their broadband UV, optical, and near-infrared SEDs. It builds on the Bayesian formalism pioneered by Kauffmann et al. (2003a) to model the optical spectral features of SDSS galaxies, and its subsequent extension to broadband photometry (e.g., Bundy et al. 2005; Salim et al. 2005, 2007; da Cunha et al. 2008; Auger et al. 2009; McGee et al. 2011; Taylor et al. 2011). To date, stellar masses and other physical parameters derived using iSEDfit have been used to measure the evolution of the stellar mass-metallicity relation (Moustakas et al. 2011), the stellar mass dependence of AGN accretion (Aird et al. 2012), the stellar mass and SFR surface densities of compact starbursts with high-velocity outflows (Diamond-Stanic et al. 2012), and the ages, SFRs, and stellar masses of galaxies at $z = 6$–10 (Zitrin et al. 2012; Zheng et al. 2012), with many subsequent applications forthcoming.

Like all SED-modeling codes designed to extract the physical properties of galaxies,[40] iSEDfit relies on stellar population synthesis (SPS) models to provide as input $\mathcal{S}(\lambda, t, Z)$, the spectral evolution of a simple stellar population (SSP) of a given stellar metallicity, Z. An SSP is an idealized stellar population formed in an instantaneous burst of star formation which evolves passively thereafter with time t. The basic ingredients of an SSP are (e.g., Tinsley 1968; Bruzual 1983): (1) stellar evolution calculations for stars spanning the full range of initial mass; (2) a stellar library that provides the emergent spectrum of a star at each position in the Hertzsprung–Russell (HR) diagram; and

(3) an assumed IMF, which specifies the relative number of stars of a given stellar mass.

Unfortunately, even the relatively "simple" goal of modeling SSPs is limited by uncertainties in calculating particular phases of stellar evolution, inadequacies in the stellar libraries (e.g., non-solar abundance ratios, spectral coverage and resolution, etc.), and other simplifying assumptions (see Conroy et al. 2009 and Conroy & Gunn 2010 for recent in-depth discussions). For example, among the least well understood phases of stellar evolution are the thermally pulsating asymptotic giant branch (TP-AGB) stars, blue stragglers (BS), and horizontal branch (HB) stars, all of which are relatively luminous and can therefore affect the integrated spectrum of the stellar population (e.g., Maraston 2005; Melbourne et al. 2012). SSP calculations also implicitly assume a well-sampled (i.e., fully populated) IMF, which may not always be satisfied (e.g., Fumagalli et al. 2011).

Differences in how these issues are addressed (or ignored) for a given IMF can lead to significant systematic discrepancies among SSPs derived using different SPS models. In principal, the uncertainties affecting SSPs should be incorporated into the SED modeling in order to obtain reliable parameter estimates and realistic confidence intervals (e.g., Conroy et al. 2010). In practice, however, this procedure is both cumbersome and computationally challenging. Instead, iSEDfit adopts the simplified approach of allowing the user to select from among many different SPS models, thereby allowing the effects of choosing one set of SSPs over another to be systematically investigated.

A.2. From Simple Stellar Populations to Spectral Energy Distributions of "Galaxies"

Given $\mathcal{S}(\lambda, t, Z)$, iSEDfit computes the integrated SED of a "galaxy" (a composite stellar population) as a function of time t using the following convolution integral:

$$\mathcal{C}(\lambda, t, Z) = \int_0^t \psi(t - t') \mathcal{S}[\lambda, t', Z(t - t')] \, 10^{-0.4A(\lambda, t')} \, dt',$$

(A1)

where $\psi(t)$ is the SFH, and $A(\lambda)$ is the wavelength-dependent attenuation, which in general may depend on time (e.g., Charlot & Fall 2000). The current version of iSEDfit only handles mono-metallic stellar populations (i.e., it does not treat the chemical evolution of the system self-consistently) in which case Equation (A1) reduces to

$$\mathcal{C}(\lambda, t, Z) = \int_0^t \psi(t - t') \mathcal{S}(\lambda, t', Z) \, 10^{-0.4A(\lambda, t')} \, dt'. \quad \text{(A2)}$$

In order to solve this integral, iSEDfit requires several additional inputs (implicit prior assumptions) from the user. First, an extinction or attenuation[41] curve, $k(\lambda) \equiv A(\lambda)/E(B - V)$, must be chosen among several different possibilities, where $A(\lambda)$ is the total wavelength-dependent attenuation and $E(B - V)$ is the color excess (Calzetti 2001). The currently supported possibilities are the Calzetti et al. (2000) starburst galaxy attenuation curve, the Charlot & Fall (2000) attenuation law, the O'Donnell (1994) Milky Way extinction curve, the extinction curve of the Small Magellanic Cloud (Gordon et al. 2003), or no attenuation. Note that among these only the Charlot & Fall (2000) attenuation curve is time-dependent.

Next, a parametric form for the SFH must be specified. In principal, $\psi(t)$ could be arbitrarily complex, or even non-parametric (e.g., Cid Fernandes et al. 2005; Tojeiro et al. 2007; Panter et al. 2008). In practice, however, it is challenging if not impossible to constrain the detailed SFHs of individual galaxies from broadband photometry alone (i.e., without high-resolution spectroscopy, although see Dye 2008). On the other hand, the integrated spectra of many star-forming galaxies may be poorly fitted by simple (e.g., exponentially declining) SFHs. Therefore, `iSEDfit` optionally allows stochastic bursts to be superposed on a backbone of smooth SFHs (e.g., Kauffmann et al. 2003a). For the underlying smooth component, the user can choose either exponentially declining SFHs (so-called simple τ-models; Sandage 1986):

$$\psi_s(t) = \frac{\mathcal{M}_{\rm tot}}{\tau} e^{-t/\tau}; \qquad (A3)$$

or "delayed" τ-models:

$$\psi_s(t) = \frac{\mathcal{M}_{\rm tot}}{\tau^2} t \, e^{-t/\tau}, \qquad (A4)$$

where the subscript "s" indicates that these are "smooth" SFHs, t is the age of the stellar population (the time since the onset of star formation), τ is the characteristic time for star formation, and the normalization is defined to be $\mathcal{M}_{\rm tot} = 1\,\mathcal{M}_\odot$. The delayed τ-models are advantageous because they allow for both exponentially declining ($t/\tau \gg 1$) and linearly rising ($t/\tau \ll 1$) SFHs to be explored, the latter of which are needed to accurately reproduce the colors of high-redshift ($z \gtrsim 2$) galaxies (e.g., Maraston et al. 2010; Papovich et al. 2011; Behroozi et al. 2012).

We characterize each burst by three independent parameters: the time the burst begins, t_b, its duration, Δt_b, and the *burst fraction*, the relative strength of the burst, $\mathcal{F}_b$. The SFH of each burst, $\psi_b(t)$, is a Gaussian function given by

$$\psi_b(t) = \frac{\mathcal{A}_b}{\sqrt{2\pi}} e^{-(t-t_b)^2/2\Delta t_b^2}, \qquad (A5)$$

where $\mathcal{A}_b$ is the *burst amplitude*. Defining $\mathcal{F}_b$ to be the mass formed in the burst divided by the total mass formed by the underlying τ model until the peak of burst, we obtain

$$\mathcal{F}_b \equiv \frac{\mathcal{M}_b}{\mathcal{M}_\tau(t_b)} = \frac{\Delta t_b}{\mathcal{M}_{\rm tot}(1 - e^{-t_b/\tau})} \mathcal{A}_b, \qquad (A6)$$

where $\mathcal{M}_\tau(t_b) \equiv \int_0^{t_b} \psi_\tau(t)\,dt$, and $\mathcal{M}_{\rm tot} = 1\,\mathcal{M}_\odot$. Equation (A6) assumes a simple τ-model, but a similar expression can be derived for the delayed τ-model. The final composite SFH is given by

$$\psi(t) = \psi_s(t) + \sum_{j=1}^{N_{\rm burst}} \psi_{b_j}(t), \qquad (A7)$$

where $N_{\rm burst}$ is the total number of bursts experienced by each model galaxy. The number of bursts is determined by specifying the cumulative probability $P_{\rm burst}$ for a burst to occur within a $\Delta P_{\rm burst}$ time interval. Finally, we note that the current version of `iSEDfit` additionally allows the final burst to be truncated exponentially with a characteristic time $\tau_{\rm trunc}$, thereby allowing the SFHs and physical properties of post-starburst galaxies to be investigated (e.g., Tremonti et al. 2007).

A.3. Extracting the Physical Properties of Galaxies from Broadband Photometry

Based on the large number of free parameters needed to model the integrated SEDs of galaxies, it would be far too computationally expensive to explore all possible parameter combinations (e.g., on a uniform grid). Moreover, traditional best-fitting (maximum likelihood) techniques are limited because they only account for photometric uncertainties, but not physical degeneracies among different models (parameter combinations). Alternatively, Markov Chain Monte Carlo (MCMC) algorithms may be more suitable for exploring the multi-dimensional parameter space (e.g., Acquaviva et al. 2011). However, MCMC methods are typically too slow to enable tens, hundreds, or even millions of galaxies to be fitted in a timely manner with multiple independent prior parameter combinations or SPS models.

Given the limitations of these other techniques, `iSEDfit` extracts the physical parameters of interest using a simplified Bayesian approach (Walcher et al. 2011, and references therein). First, the model parameters are drawn from a user-specified prior probability distribution using a Monte Carlo technique. Next, given the broadband fluxes F_i of a galaxy at redshift z in $i = 1, N$ filters, and the corresponding σ_i uncertainties, `iSEDfit` uses Bayes' theorem to compute the posterior PDF

$$p(\mathbf{Q}|F_i, z) = p(\mathbf{Q}) \times p(F_i, z|\mathbf{Q}), \qquad (A8)$$

where $\mathbf{Q}$ represents the set of model parameters (stellar mass, age, metallicity, etc.). Here, $p(\mathbf{Q})$ is the prior probability of the model parameters, $p(F_i, z|\mathbf{Q})$ is the likelihood $\mathcal{L} \propto \exp[-\chi^2(F_i, z|\mathbf{Q})/2]$ of the data given the model, and χ^2 is the usual goodness-of-fit statistic appropriate for normally distributed photometric uncertainties, given by

$$\chi^2(F_i, z|\mathbf{Q}) = \sum_{i=1}^{N} \frac{[F_i - \mathcal{A}\,\mathcal{C}_i(\mathbf{Q}, z)]^2}{\sigma_i^2}, \qquad (A9)$$

where $\mathcal{A}$ is a normalization factor, and the $\mathcal{C}_i(\mathbf{Q}, z)$ are the broadband fluxes of each model SED given the redshift and parameter combination $\mathbf{Q}$. Once χ^2 has been computed for every model, the marginalized posterior PDF of the parameter of interest, for example $p(\mathcal{M})$ for the stellar mass, can be derived by randomly drawing each parameter value with probability given by Equation (A8), thereby effectively integrating (using histogram binning) over the other "nuisance" parameters. Although `iSEDfit` is capable of reconstructing the full posterior distributions in post-processing after the computationally intensive fitting has been completed, the code by default provides the median of the posterior PDF as the best estimate of each parameter, and estimates the uncertainty in each parameter as 1/4 of the 2.3–97.7 percentile range of the posterior distribution, which would be equivalent to 1σ for a Gaussian distribution.

A.4. Consistency Checks

In Figure 18 we verify that the stellar masses we derive using `iSEDfit` for our SDSS-*GALEX* sample based on our fiducial prior parameters (see Section 4.1 and Appendix B) are reasonable, by comparing them against the stellar masses of the same objects derived using four other independent techniques. In each panel the solid line indicates the median residual trend, and the dashed lines show the interquartile range of the residuals.
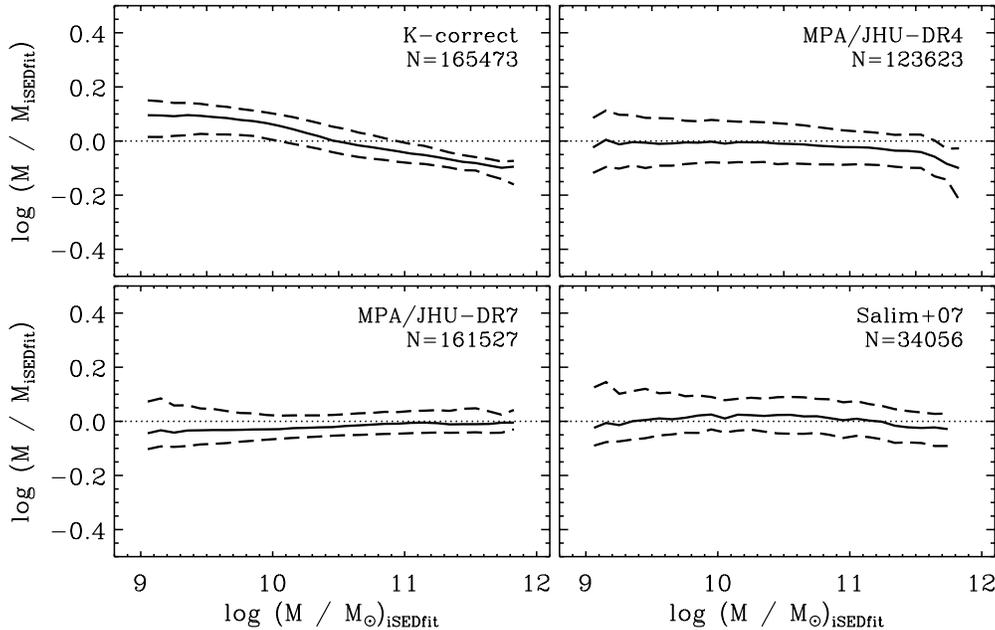
Figure 18. Comparison of stellar masses derived using `iSEDfit` (see Section 4.1) for our SDSS-*GALEX* sample vs. stellar masses derived using the four independent techniques described in Appendix A.4. The solid line in each panel indicates the median residual trend, and the dashed lines show the interquartile range of the residuals. The dotted horizontal line shows for reference the one-to-one relation. Overall, we find very good agreement between the stellar masses derived using `iSEDfit` and these various other methods.

The upper-left panel compares our stellar masses against the stellar masses derived using `K-correct` (Blanton & Roweis 2007), fitted to the same 12-band UV to mid-infrared photometry as `iSEDfit` (see Section 2.4). We find a weak residual trend with stellar mass, in the sense that `K-correct` yields slightly higher (lower) stellar masses for lower-mass (higher-mass) galaxies, which for the massive galaxies at least is similar to the residual trend reported by Bernardi et al. (2010). The upper-right and lower-left panels compare our masses against the stellar masses publicly released by the MPA/JHU team based on the SDSS DR4[42] and DR7[43] data releases. The MPA/JHU-DR4 masses are based on fitting the $H\delta_A$ and $D_n(4000)$ optical spectral indices (Kauffmann et al. 2003a), and the DR7 stellar masses are derived using a similar technique as `iSEDfit`, but only fitting to the SDSS *ugriz* photometry. In both cases the agreement between the various independent determinations is outstanding. Finally, in the lower-right panel we compare our mass estimates against the stellar masses derived by Salim et al. (2007) using a similar SED-modeling technique as `iSEDfit`, but just fitting to the *GALEX* plus *ugriz* photometry. Once again, the agreement between the two stellar mass estimates is very good.

APPENDIX B

EFFECT OF PRIOR PARAMETER CHOICES AND POPULATION SYNTHESIS MODELS ON OUR RESULTS

In this appendix we examine the effect of varying the SPS models and prior parameters we use to derive stellar masses and SFRs on our results (see also Section 4.1). We consider four distinct SPS models: FSPS (v2.3; Conroy et al. 2009; Conroy & Gunn 2010); Bruzual & Charlot (2003, hereafter

BC03); the SPS models of Maraston (2005, hereafter Ma05);[44] and PEGASE[45] (Fioc & Rocca-Volmerange 1997, 1999; Le Borgne et al. 2004). For the FSPS and BC03 models we adopt the Chabrier (2003) IMF from 0.1–100 $\mathcal{M}_\odot$, and for Ma05 and PEGASE we use the Kroupa (2001) IMF from 0.1–100 $\mathcal{M}_\odot$. We neglect the ∼0.03 dex systematic difference between the two IMFs. Each of these models relies on a different combination of stellar evolution calculations and stellar libraries and therefore they differ in their predictions of the integrated spectra of galaxies.

For completeness, we briefly summarize the salient features of each of these SPS models. Our fiducial stellar masses and SFRs are based on the empirically calibrated version of the FSPS models described by Conroy & Gunn (2010). We couple these models to the Padova[46] stellar evolutionary isochrones (Girardi et al. 2000; Marigo & Girardi 2007; Marigo et al. 2008), which have been supplemented with the Vassiliadis & Wood (1994) models for post-AGB stars. Integrated spectra are generated using the low-resolution, semi-empirical BaSeL 3.1 library (Lejeune et al. 1997, 1998; Westera et al. 2002), which extends from the UV to the rest-frame near-infrared, except for the TP-AGB stars, for which the empirical spectra of Lançon & Mouhcine (2002) are used over the full wavelength range. The BC03 models we use are based on the Padova 1994 isochrones (Alongi et al. 1993; Bressan et al. 1993; Fagotto et al. 1994), supplemented with the Vassiliadis & Wood (1993) and Vassiliadis & Wood (1994) models for TP-AGB and post-AGB stars, respectively. Integrated spectra are synthesized using the empirical STELIB stellar library (Le Borgne et al. 2003) in the optical (3200–9500 Å) and extended into the UV
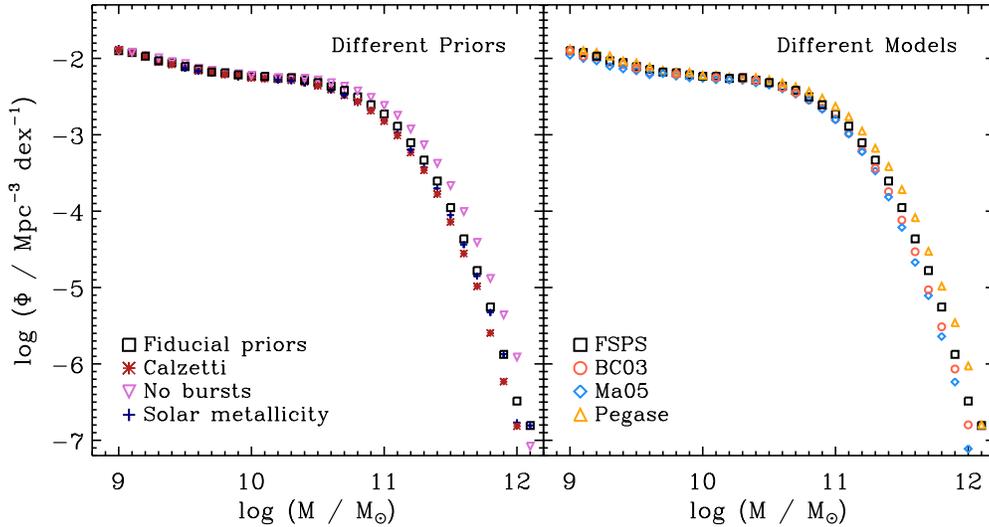
[42] http://www.mpa-garching.mpg.de/SDSS/DR4
[43] http://www.mpa-garching.mpg.de/SDSS/DR7

[44] http://www-astro.physics.ox.ac.uk/∼maraston/Claudia's_Stellar_Population_Models.html
[45] http://www2.iap.fr/pegase/pegasehr
[46] http://stev.oapd.inaf.it/cgi-bin/cmd

Figure 19. Effect on the SDSS-*GALEX* SMF of (left) different prior parameter combinations and (right) different population synthesis models (see the text in Appendix B for acronym definitions and details). We find that assuming that galaxies do not experience stochastic bursts ("no bursts") has a significant effect on the massive end ($\mathcal{M} \gtrsim 10^{11} \, \mathcal{M}_{\odot}$) of the SMF, whereas for all other combinations of priors and population synthesis models the effects are relatively small ($\lesssim$0.1 dex). (A color version of this figure is available in the online journal.)

and near-IR at lower resolution using the BaSeL 3.1 library. Finally, the Ma05 models are based on the stellar tracks and isochrones through the main-sequence turnoff published by Schaller et al. (1992) and Cassisi et al. (1997, 2000). The fuel consumption theorem (Maraston 1998, 2005) is used to calculate the post-main-sequence phases of stellar evolution, including the TP-AGB phase. These evolutionary calculations are then tied to the Lançon & Mouhcine (2002) empirical spectra for TP-AGB stars and to the BaSeL 3.1 spectral library for other stellar populations, resulting in a set of integrated spectra from the UV to the near-infrared. In our calculations we adopt the version of the models computed using the "red horizontal branch" morphology (see Maraston 2005 for details). Finally, PEGASE utilizes the early-1990s version of the Padova stellar isochrones and couples those to the BaSeL stellar library.

Our fiducial prior parameters were briefly described in Section 4.1, but here we provide more details (see Appendix A for additional salient details and parameter definitions). We assume exponentially declining SFHs with Gaussian bursts of varying onset, strength, and duration randomly superposed. Following Kauffmann et al. (2003a) and Salim et al. (2007), we draw τ^{-1} from a uniform distribution in the range 0.01–10 Gyr^{-1} and allow bursts to occur with a cumulative probability $P_{\rm burst} = 0.5$ every $\Delta P_{\rm burst} = 2$ Gyr. We draw Δt_b from a logarithmic distribution in the range 30–300 Myr (i.e., shorter-duration bursts are preferred) and $\mathcal{F}_b$ from a logarithmic distribution spanning 0.03–4 (Salim et al. 2007; Wild et al. 2009). We allow the age t (time for the onset of star formation) of each model to range with equal probability between 0.1–13 Gyr, although we disallow ages older than the age of the universe at the redshift of each galaxy. We assume a uniform prior on stellar metallicity Z in the range 0.004–0.03 (roughly 20%–150% times the solar metallicity; Asplund et al. 2009). Because the SSP models are generally only available for a small number of tabulated values of Z, we linearly interpolate between these values to obtain an SSP with an arbitrary metallicity. Finally, we adopt the time-dependent attenuation curve of Charlot & Fall (2000), in which

stellar populations older than 10 Myr are attenuated by a factor μ times less than younger stellar populations. We draw μ from an order four Gamma distribution that ranges from zero to unity centered on a typical value $\langle \mu \rangle = 0.3$ (Charlot & Longhetti 2001; Wild et al. 2011) and the V-band optical depth from an order two Gamma distribution that peaks around $A_V \approx 1.2$ mag, with a tail to $A_V \approx 6$ mag.

We consider the effect of varying a small number of these priors and SPS models on our results. Specifically, we consider stellar masses and SFRs derived assuming: (1) the Calzetti et al. (2000) starburst galaxy attenuation curve ("Calzetti"); (2) that galaxies do not experience stochastic bursts of star formation ("no bursts"); and (3) fixed solar metallicity ("solar metallicity"). Although these parameter combinations are not exhaustive, they have been chosen to reasonably span the range of priors commonly adopted in other studies of the SMF (see, e.g., Marchesini et al. 2009).

In Figure 19 we plot the SDSS-*GALEX* SMF derived using these different priors and SPS models. In the left panel we use our fiducial FSPS models and vary the prior assumptions, and in the right panel we use the same fiducial priors and vary the SPS models. Overall we find that these variations have a relatively small systematic effect on the SMF. The most significant differences result when we do not include the effects of bursts, which leads to typically higher stellar masses for massive galaxies. In Figure 20 we plot number density versus redshift for (top) quiescent and (bottom) star-forming galaxies in four bins of stellar mass between $10^{9.5}$–$10^{11.5} \, \mathcal{M}_{\odot}$ (see Section 5.2). For clarity we only show the slope of the line [in log-log space; see Equation (9)] fitted to the mean number density of galaxies measured in each redshift bin, normalized by the number density at $z = 0.1$ so that the *relative* evolutionary trends can be compared. In each panel, the gray shaded region reflects the 1σ confidence region of the mean fitted relation based on our fiducial SPS models and prior assumptions (see Figure 12 and Table 7). We find that the relative evolutionary trends we infer are generally within $\pm 1\sigma$ of the trends inferred using these other SPS models and prior assumptions.
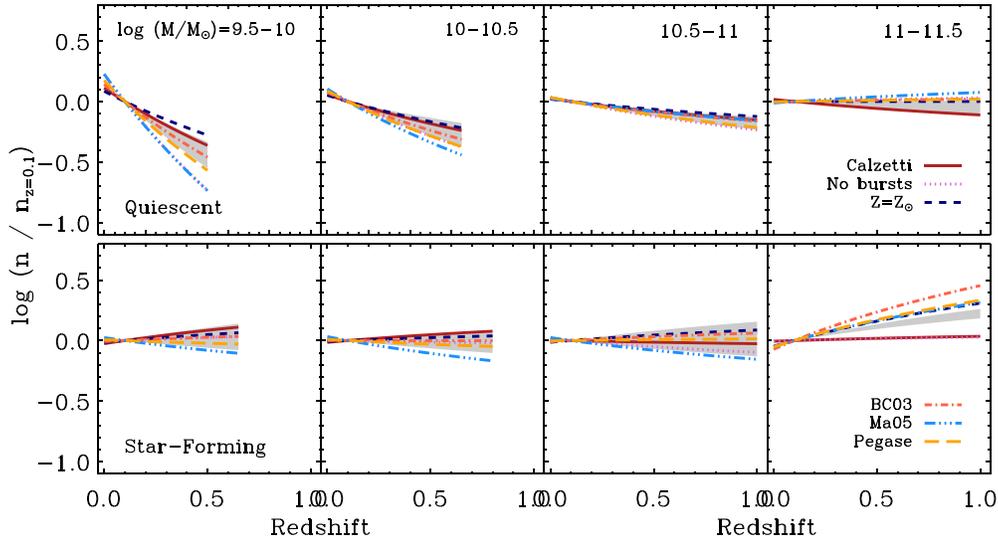
Figure 20. Relative number density vs. redshift for (top) quiescent and (bottom) star-forming galaxies in four bins of stellar mass between $10^{9.5}$–$10^{11.5}\,\mathcal{M}_\odot$ based on different SPS models and prior assumptions (see text). Each relation has been normalized by the number density at $z = 0.1$ so that the relative evolutionary trends can be compared. The gray shaded region reflects the 1σ confidence region of the mean fitted relation based on our fiducial SPS models and prior assumptions (see Figure 12). We find that the individual evolutionary trends are generally consistent with one another at the $\pm 1\sigma$ level except for the stellar masses and SFRs derived using the Calzetti et al. (2000) dust law, which exhibits a shallower (steeper) decline (increase) in the number of massive star-forming (quiescent) galaxies. Overall, however, we conclude that our results are broadly insensitive to our choice of SPS models and priors.

(A color version of this figure is available in the online journal.)

REFERENCES

Abazajian, K., Adelman-McCarthy, J. K., Agüeros, M. A., et al. 2004, AJ, 128, 502

Abazajian, K. N., Adelman-McCarthy, J. K., Agüeros, M. A., et al. 2009, ApJS, 182, 543

Acquaviva, V., Gawiser, E., & Guaita, L. 2011, ApJ, 737, 47

Aird, J., Coil, A. L., Moustakas, J., et al. 2012, ApJ, 746, 90

Alongi, M., Bertelli, G., Bressan, A., et al. 1993, A&AS, 97, 851

Arnouts, S., Walcher, C. J., Le Fèvre, O., et al. 2007, A&A, 476, 137

Asplund, M., Grevesse, N., Sauval, A. J., & Scott, P. 2009, ARA&A, 47, 481

Auger, M. W., Treu, T., Bolton, A. S., et al. 2009, ApJ, 705, 1099

Baldry, I. K., Driver, S. P., Loveday, J., et al. 2012, MNRAS, 421, 621

Baldry, I. K., Glazebrook, K., Brinkmann, J., et al. 2004, ApJ, 600, 681

Baldry, I. K., Glazebrook, K., & Driver, S. P. 2008, MNRAS, 388, 945

Balogh, M. L., Navarro, J. F., & Morris, S. L. 2000, ApJ, 540, 113

Bastian, N., Covey, K. R., & Meyer, M. R. 2010, ARA&A, 48, 339

Behroozi, P. S., Wechsler, R. H., & Conroy, C. 2012, arXiv:1207.6105

Bell, E. F., McIntosh, D. H., Katz, N., & Weinberg, M. D. 2003, ApJS, 149, 289

Bell, E. F., Wolf, C., Meisenheimer, K., et al. 2004, ApJ, 608, 752

Bell, E. F., Zheng, X. Z., Papovich, C., et al. 2007, ApJ, 663, 834

Bernardi, M., Shankar, F., Hyde, J. B., et al. 2010, MNRAS, 404, 2087

Berta, S., Rubele, S., Franceschini, A., et al. 2006, A&A, 451, 881

Berta, S., Rubele, S., Franceschini, A., et al. 2008, A&A, 488, 533

Bertin, E., & Arnouts, S. 1996, A&AS, 117, 393

Bigelow, B. C., & Dressler, A. M. 2003, Proc. SPIE, 4841, 1727

Blanton, M. R. 2006, ApJ, 648, 268

Blanton, M. R., Hogg, D. W., Bahcall, N. A., et al. 2003a, ApJ, 594, 186

Blanton, M. R., Hogg, D. W., Bahcall, N. A., et al. 2003b, ApJ, 592, 819

Blanton, M. R., Kazin, E., Muna, D., Weaver, B. A., & Price-Whelan, A. 2011, AJ, 142, 31

Blanton, M. R., Lin, H., Lupton, R. H., et al. 2003c, AJ, 125, 2276

Blanton, M. R., Lupton, R. H., Schlegel, D. J., et al. 2005a, ApJ, 631, 208

Blanton, M. R., & Moustakas, J. 2009, ARA&A, 47, 159

Blanton, M. R., & Roweis, S. 2007, AJ, 133, 734

Blanton, M. R., Schlegel, D. J., Strauss, M. A., et al. 2005b, AJ, 129, 2562

Borch, A., Meisenheimer, K., Bell, E. F., et al. 2006, A&A, 453, 869

Boselli, A., & Gavazzi, G. 2006, PASP, 118, 517

Boulade, O., Charlot, X., Abbon, P., et al. 2003, Proc. SPIE, 4841, 72

Bower, R. G., Benson, A. J., & Crain, R. A. 2012, MNRAS, 422, 2816

Brammer, G. B., Whitaker, K. E., van Dokkum, P. G., et al. 2009, ApJL, 706, L173

Brammer, G. B., Whitaker, K. E., van Dokkum, P. G., et al. 2011, ApJ, 739, 24

Brand, K., Moustakas, J., Armus, L., et al. 2009, ApJ, 693, 340

Bressan, A., Fagotto, F., Bertelli, G., & Chiosi, C. 1993, A&AS, 100, 647

Brinchmann, J., Charlot, S., White, S. D. M., et al. 2004, MNRAS, 351, 1151

Brown, M. J. I., Dey, A., Jannuzi, B. T., et al. 2007, ApJ, 654, 858

Bruzual, G. 1983, ApJ, 273, 105

Bruzual, G., & Charlot, S. 2003, MNRAS, 344, 1000

Budavári, T., Heinis, S., Szalay, A. S., et al. 2009, ApJ, 694, 1281

Bundy, K., Ellis, R. S., & Conselice, C. J. 2005, ApJ, 625, 621

Bundy, K., Ellis, R. S., Conselice, C. J., et al. 2006, ApJ, 651, 120

Calzetti, D. 2001, PASP, 113, 1449

Calzetti, D., Armus, L., Bohlin, R. C., et al. 2000, ApJ, 533, 682

Capak, P., Aussel, H., Ajiki, M., et al. 2007, ApJS, 172, 99

Cappellari, M., McDermid, R. M., Alatalo, K., et al. 2012, Natur, 484, 485

Carter, D., Smith, D. J. B., Percival, S. M., et al. 2009, MNRAS, 397, 695

Cassata, P., Cimatti, A., Kurk, J., et al. 2008, A&A, 483, L39

Cassisi, S., Castellani, M., & Castellani, V. 1997, A&A, 317, 108

Cassisi, S., Castellani, V., Ciarcelluti, P., Piotto, G., & Zoccali, M. 2000, MNRAS, 315, 679

Cattaneo, A., Dekel, A., Devriendt, J., Guiderdoni, B., & Blaizot, J. 2006, MNRAS, 370, 1651

Cattaneo, A., Dekel, A., Faber, S. M., & Guiderdoni, B. 2008, MNRAS, 389, 567

Cattaneo, A., Mamon, G. A., Warnick, K., & Knebe, A. 2011, A&A, 533, A5

Chabrier, G. 2003, PASP, 115, 763

Charlot, S., & Fall, S. M. 2000, ApJ, 539, 718

Charlot, S., & Longhetti, M. 2001, MNRAS, 323, 887

Cid Fernandes, R., Mateus, A., Sodré, L., Stasińska, G., & Gomes, J. M. 2005, MNRAS, 358, 363

Cimatti, A., Daddi, E., & Renzini, A. 2006, A&A, 453, L29

Coil, A. L., Blanton, M. R., Burles, S. M., et al. 2011, ApJ, 741, 8

Cole, S., Lacey, C. G., Baugh, C. M., & Frenk, C. S. 2000, MNRAS, 319, 168

Cole, S., Norberg, P., Baugh, C. M., et al. 2001, MNRAS, 326, 255

Conroy, C., & Gunn, J. E. 2010, ApJ, 712, 833

Conroy, C., Gunn, J. E., & White, M. 2009, ApJ, 699, 486

Conroy, C., & Wechsler, R. H. 2009, ApJ, 696, 620

Conroy, C., White, M., & Gunn, J. E. 2010, ApJ, 708, 58

Cool, R. J., Eisenstein, D. J., Kochanek, C. S., et al. 2012, ApJ, 748, 10

Cool, R. J., Moustakas, J., Blanton, M. R., et al. 2013, ApJ, in press (arXiv:1303.2672)

Cooper, M. C., Newman, J. A., Coil, A. L., et al. 2007, MNRAS, 376, 1445

Croton, D. J., Springel, V., White, S. D. M., et al. 2006, MNRAS, 365, 11

da Cunha, E., Charlot, S., & Elbaz, D. 2008, MNRAS, 388, 1595

Dai, X., Assef, R. J., Kochanek, C. S., et al. 2009, ApJ, 697, 506

Davé, R. 2008, MNRAS, 385, 147

Davé, R., Finlator, K., & Oppenheimer, B. D. 2011a, MNRAS, 416, 1354

Davé, R., Oppenheimer, B. D., & Finlator, K. 2011b, MNRAS, 415, 11

Dekel, A., & Birnboim, Y. 2006, MNRAS, 368, 2
De Lucia, G., Springel, V., White, S. D. M., Croton, D., & Kauffmann, G. 2006, MNRAS, 366, 499
Diamond-Stanic, A. M., Moustakas, J., Tremonti, C. A., et al. 2012, ApJL, 755, L26
Di Matteo, T., Springel, V., & Hernquist, L. 2005, Natur, 433, 604
Domínguez Sánchez, H., Pozzi, F., Gruppioni, C., et al. 2011, MNRAS, 417, 900
Driver, S. P., Allen, P. D., Graham, A. W., et al. 2006, MNRAS, 368, 414
Driver, S. P., Hill, D. T., Kelvin, L. S., et al. 2011, MNRAS, 413, 971
Drory, N., & Alvarez, M. 2008, ApJ, 680, 41
Drory, N., Bundy, K., Leauthaud, A., et al. 2009, ApJ, 707, 1595
Dye, S. 2008, MNRAS, 389, 1293
Elbaz, D., Daddi, E., Le Borgne, D., et al. 2007, A&A, 468, 33
Erben, T., Hildebrandt, H., Lerchster, M., et al. 2009, A&A, 493, 1197
Faber, S. M., Willmer, C. N. A., Wolf, C., et al. 2007, ApJ, 665, 265
Fagotto, F., Bressan, A., Bertelli, G., & Chiosi, C. 1994, A&AS, 104, 365
Fazio, G. G., Hora, J. L., Allen, L. E., et al. 2004, ApJS, 154, 10
Fioc, M., & Rocca-Volmerange, B. 1997, A&A, 326, 950
Fioc, M., & Rocca-Volmerange, B. 1999, arXiv:astro-ph/9912179
Fontana, A., Salimbeni, S., Grazian, A., et al. 2006, A&A, 459, 745
Fontanot, F., De Lucia, G., Monaco, P., Somerville, R. S., & Santini, P. 2009, MNRAS, 397, 1776
Fumagalli, M., da Silva, R. L., & Krumholz, M. R. 2011, ApJL, 741, L26
Furusawa, H., Kosugi, G., Akiyama, M., et al. 2008, ApJS, 176, 1
Gabor, J. M., Davé, R., Oppenheimer, B. D., & Finlator, K. 2011, MNRAS, 417, 2676
Garn, T., & Best, P. N. 2010, MNRAS, 409, 421
Gehrels, N. 1986, ApJ, 303, 336
Girardi, L., Bressan, A., Bertelli, G., & Chiosi, C. 2000, A&AS, 141, 371
Gonzalez, A. H., Zaritsky, D., & Zabludoff, A. I. 2007, ApJ, 666, 147
Gordon, K. D., Clayton, G. C., Misselt, K. A., Landolt, A. U., & Wolff, M. J. 2003, ApJ, 594, 279
Gott, J. R., III, Jurić, M., Schlegel, D., et al. 2005, ApJ, 624, 463
Guillaume, M., Llebaria, A., Aymeric, D., Arnouts, S., & Milliard, B. 2006, Proc. SPIE, 6064, 332
Gunn, J. E., & Gott, J. R., III 1972, ApJ, 176, 1
Hamilton, A. J. S., & Tegmark, M. 2004, MNRAS, 349, 115
Hammer, D., Hornschemeier, A. E., Mobasher, B., et al. 2010, ApJS, 190, 43
Hogg, D. W. 1999, arXiv:astro-ph/9905116
Hopkins, P. F., Cox, T. J., Kereš, D., & Hernquist, L. 2008a, ApJS, 175, 390
Hopkins, P. F., Hernquist, L., Cox, T. J., & Kereš, D. 2008b, ApJS, 175, 356
Ilbert, O., Capak, P., Salvato, M., et al. 2009, ApJ, 690, 1236
Ilbert, O., Salvato, M., Le Floc'h, E., et al. 2010, ApJ, 709, 644
Jarrett, T. H., Chester, T., Cutri, R., et al. 2000, AJ, 119, 2498
Johnston, R. 2011, A&ARv, 19, 41
Kajisawa, M., Ichikawa, T., Tanaka, I., et al. 2009, ApJ, 702, 1393
Kannappan, S. J., & Gawiser, E. 2007, ApJL, 657, L5
Karim, A., Schinnerer, E., Martínez-Sansigre, A., et al. 2011, ApJ, 730, 61
Kauffmann, G., Heckman, T. M., White, S. D. M., et al. 2003a, MNRAS, 341, 33
Kauffmann, G., Heckman, T. M., White, S. D. M., et al. 2003b, MNRAS, 341, 54
Kelson, D. D., Williams, R. J., Dressler, A., et al. 2012, arXiv:1201.0783
Kereš, D., Katz, N., Davé, R., Fardal, M., & Weinberg, D. H. 2009, MNRAS, 396, 2332
Kereš, D., Katz, N., Weinberg, D. H., & Davé, R. 2005, MNRAS, 363, 2
Kimm, T., Somerville, R. S., Yi, S. K., et al. 2009, MNRAS, 394, 1131
Knobel, C., Lilly, S. J., Kovac, K., et al. 2012, arXiv:1211.5607
Kovač, K., Lilly, S. J., Cucciati, O., et al. 2010, ApJ, 708, 505
Kroupa, P. 2001, MNRAS, 322, 231
Lançon, A., & Mouhcine, M. 2002, A&A, 393, 167
Larson, R. B., Tinsley, B. M., & Caldwell, C. N. 1980, ApJ, 237, 692
Leauthaud, A., Tinker, J., Bundy, K., et al. 2012, ApJ, 744, 159
Le Borgne, D., Rocca-Volmerange, B., Prugniel, P., et al. 2004, A&A, 425, 881
Le Borgne, J.-F., Bruzual, G., Pelló, R., et al. 2003, A&A, 402, 433
Le Fèvre, O., Saisse, M., Mancini, D., et al. 2003, Proc. SPIE, 4841, 1670
Leitner, S. N., & Kravtsov, A. V. 2011, ApJ, 734, 48
Lejeune, T., Cuisinier, F., & Buser, R. 1997, A&AS, 125, 229
Lejeune, T., Cuisinier, F., & Buser, R. 1998, A&AS, 130, 65
Li, C., & White, S. D. M. 2009, MNRAS, 398, 2177
Lilly, S. J., Le Brun, V., Maier, C., et al. 2009, ApJS, 184, 218
Longhetti, M., & Saracco, P. 2009, MNRAS, 394, 774
Lonsdale, C. J., Smith, H. E., Rowan-Robinson, M., et al. 2003, PASP, 115, 897
Lotz, J. M., Jonsson, P., Cox, T. J., et al. 2011, ApJ, 742, 103
Loveday, J., Norberg, P., Baldry, I. K., et al. 2012, MNRAS, 420, 1239
Lu, Y., Mo, H. J., Katz, N., & Weinberg, M. D. 2012, MNRAS, 421, 1779

Maller, A. H., Berlind, A. A., Blanton, M. R., & Hogg, D. W. 2009, ApJ, 691, 394
Mancone, C. L., & Gonzalez, A. H. 2012, PASP, 124, 606
Maraston, C. 1998, MNRAS, 300, 872
Maraston, C. 2005, MNRAS, 362, 799
Maraston, C., Daddi, E., Renzini, A., et al. 2006, ApJ, 652, 85
Maraston, C., Pforr, J., Henriques, B. M., et al. 2012, arXiv:1207.6114
Maraston, C., Pforr, J., Renzini, A., et al. 2010, MNRAS, 407, 830
Marchesini, D., van Dokkum, P. G., Förster Schreiber, N. M., et al. 2009, ApJ, 701, 1765
Marigo, P., & Girardi, L. 2007, A&A, 469, 239
Marigo, P., Girardi, L., Bressan, A., et al. 2008, A&A, 482, 883
Martig, M., Bournaud, F., Teyssier, R., & Dekel, A. 2009, ApJ, 707, 250
Martin, D. C., Fanson, J., Schiminovich, D., et al. 2005, ApJL, 619, L1
Martin, D. C., Wyder, T. K., Schiminovich, D., et al. 2007, ApJS, 173, 342
Matsuoka, Y., & Kawara, K. 2010, MNRAS, 405, 100
McCracken, H. J., Capak, P., Salvato, M., et al. 2010, ApJ, 708, 202
McGee, S. L., Balogh, M. L., Wilman, D. J., et al. 2011, MNRAS, 413, 996
Melbourne, J., Williams, B. F., Dalcanton, J. J., et al. 2012, ApJ, 748, 47
Miyazaki, S., Komiyama, Y., Sekiguchi, M., et al. 2002, PASJ, 54, 833
Monaco, P., Murante, G., Borgani, S., & Fontanot, F. 2006, ApJL, 652, L89
Moore, B., Lake, G., & Katz, N. 1998, ApJ, 495, 139
Morrissey, P., Conrow, T., Barlow, T. A., et al. 2007, ApJS, 173, 682
Morrissey, P., Schiminovich, D., Barlow, T. A., et al. 2005, ApJL, 619, L7
Mortlock, A., Conselice, C. J., Bluck, A. F. L., et al. 2011, MNRAS, 413, 2845
Moster, B. P., Somerville, R. S., Newman, J. A., & Rix, H.-W. 2011, ApJ, 731, 113
Moustakas, J., Zaritsky, D., Brown, M., et al. 2011, arXiv:1112.3300
Murante, G., Giovalli, M., Gerhard, O., et al. 2007, MNRAS, 377, 2
Muzzin, A., Marchesini, D., van Dokkum, P. G., et al. 2009, ApJ, 701, 1839
Nicol, M.-H., Meisenheimer, K., Wolf, C., & Tapken, C. 2011, ApJ, 727, 51
Noeske, K. G., Weiner, B. J., Faber, S. M., et al. 2007, ApJL, 660, L43
Norris, R. P., Afonso, J., Appleton, P. N., et al. 2006, AJ, 132, 2409
O'Donnell, J. E. 1994, ApJ, 422, 158
Oke, J. B., & Gunn, J. E. 1983, ApJ, 266, 713
Oliver, S., Frost, M., Farrah, D., et al. 2010, MNRAS, 405, 2279
Oliver, S., Rowan-Robinson, M., Alexander, D. M., et al. 2000, MNRAS, 316, 749
Panter, B., Jimenez, R., Heavens, A. F., & Charlot, S. 2008, MNRAS, 391, 1117
Papovich, C., Finkelstein, S. L., Ferguson, H. C., Lotz, J. M., & Giavalisco, M. 2011, MNRAS, 412, 1123
Peng, Y.-j., Lilly, S. J., Kovač, K., et al. 2010, ApJ, 721, 193
Pérez-González, P. G., Rieke, G. H., Villar, V., et al. 2008, ApJ, 675, 234
Pforr, J., Maraston, C., & Tonini, C. 2012, MNRAS, 422, 3285
Pierre, M., Valtchanov, I., Altieri, B., et al. 2004, JCAP, 9, 11
Pozzetti, L., Bolzonella, M., Lamareille, F., et al. 2007, A&A, 474, 443
Pozzetti, L., Bolzonella, M., Zucca, E., et al. 2010, A&A, 523, A13
Puget, P., Stadler, E., Doyon, R., et al. 2004, Proc. SPIE, 5492, 978
Robaina, A. R., Bell, E. F., van der Wel, A., et al. 2010, ApJ, 719, 844
Rudnick, G., von der Linden, A., Pelló, R., et al. 2009, ApJ, 700, 1559
Salim, S., Charlot, S., Rich, R. M., et al. 2005, ApJL, 619, L39
Salim, S., Dickinson, M., Michael Rich, R., et al. 2009, ApJ, 700, 161
Salim, S., Rich, R. M., Charlot, S., et al. 2007, ApJS, 173, 267
Sandage, A. 1986, A&A, 161, 89
Sanders, D. B., Salvato, M., Aussel, H., et al. 2007, ApJS, 172, 86
Scarlata, C., Carollo, C. M., Lilly, S. J., et al. 2007, ApJS, 172, 494
Schaller, G., Schaerer, D., Meynet, G., & Maeder, A. 1992, A&AS, 96, 269
Schechter, P. 1976, ApJ, 203, 297
Schiminovich, D., Wyder, T. K., Martin, D. C., et al. 2007, ApJS, 173, 315
Schlegel, D. J., Finkbeiner, D. P., & Davis, M. 1998, ApJ, 500, 525
Scoville, N., Aussel, H., Brusa, M., et al. 2007, ApJS, 172, 1
Skrutskie, M. F., Cutri, R. M., Stiening, R., et al. 2006, AJ, 131, 1163
Smith, J. D. T., Draine, B. T., Dale, D. A., et al. 2007, ApJ, 656, 770
Somerville, R. S., Hopkins, P. F., Cox, T. J., Robertson, B. E., & Hernquist, L. 2008, MNRAS, 391, 481
Springel, V., White, S. D. M., Jenkins, A., et al. 2005, Natur, 435, 629
Stewart, K. R., Bullock, J. S., Wechsler, R. H., & Maller, A. H. 2009, ApJ, 702, 307
Stoughton, C., Lupton, R. H., Bernardi, M., et al. 2002, AJ, 123, 485
Strauss, M. A., Weinberg, D. H., Lupton, R. H., et al. 2002, AJ, 124, 1810
Surace, J. A., Shupe, D. L., Fang, F., et al. 2004, VizieR Online Data Catalog, 2255, 0
Swanson, M. E. C., Tegmark, M., Hamilton, A. J. S., & Hill, J. C. 2008, MNRAS, 387, 1391
Taylor, E. N., Franx, M., van Dokkum, P. G., et al. 2009, ApJ, 694, 1171
Taylor, E. N., Hopkins, A. M., Baldry, I. K., et al. 2011, MNRAS, 418, 1587
Tinsley, B. M. 1968, ApJ, 151, 547

Tojeiro, R., Heavens, A. F., Jimenez, R., & Panter, B. 2007, MNRAS, 381, 1252
Tremonti, C. A., Moustakas, J., & Diamond-Stanic, A. M. 2007, ApJL, 663, L77
Treu, T., Auger, M. W., Koopmans, L. V. E., et al. 2010, ApJ, 709, 1195
van Dokkum, P. G., Whitaker, K. E., Brammer, G., et al. 2010, ApJ, 709, 1018
Vassiliadis, E., & Wood, P. R. 1993, ApJ, 413, 641
Vassiliadis, E., & Wood, P. R. 1994, ApJS, 92, 125
Vergani, D., Scodeggio, M., Pozzetti, L., et al. 2008, A&A, 487, 89
Walcher, C. J., Lamareille, F., Vergani, D., et al. 2008, A&A, 491, 713
Walcher, J., Groves, B., Budavári, T., & Dale, D. 2011, Ap&SS, 331, 1
Wang, L., Farrah, D., Oliver, S. J., et al. 2012, arXiv:1203.5828
Weinmann, S. M., Pasquali, A., Oppenheimer, B. D., et al. 2012, MNRAS, 426, 2797
Weinmann, S. M., van den Bosch, F. C., Yang, X., & Mo, H. J. 2006, MNRAS, 366, 2
Werner, M. W., Roellig, T. L., Low, F. J., et al. 2004, ApJS, 154, 1
Westera, P., Lejeune, T., Buser, R., Cuisinier, F., & Bruzual, G. 2002, A&A, 381, 524
Wetzel, A. R., Tinker, J. L., Conroy, C., & van den Bosch, F. C. 2012, MNRAS, 424, 232

Whitaker, K. E., Labbé, I., van Dokkum, P. G., et al. 2011, ApJ, 735, 86
Whitaker, K. E., van Dokkum, P. G., Brammer, G., et al. 2010, ApJ, 719, 1715
Wild, V., Charlot, S., Brinchmann, J., et al. 2011, MNRAS, 417, 1760
Wild, V., Walcher, C. J., Johansson, P. H., et al. 2009, MNRAS, 395, 144
Williams, R. J., Quadri, R. F., Franx, M., van Dokkum, P., & Labbé, I. 2009, ApJ, 691, 1879
Witt, A. N., & Gordon, K. D. 2000, ApJ, 528, 799
Witt, A. N., Thronson, H. A., Jr., & Capuano, J. M., Jr. 1992, ApJ, 393, 611
Wolf, C., Meisenheimer, K., Rix, H.-W., et al. 2003, A&A, 401, 73
Woo, J., Dekel, A., Faber, S. M., et al. 2013, MNRAS, 428, 3306
Wright, E. L., Eisenhardt, P. R. M., Mainzer, A. K., et al. 2010, AJ, 140, 1868
Wyder, T. K., Martin, D. C., Schiminovich, D., et al. 2007, ApJS, 173, 293
Xu, C. K., Donas, J., Arnouts, S., et al. 2005, ApJL, 619, L11
York, D. G., Adelman, J., Anderson, J. E., Jr., et al. 2000, AJ, 120, 1579
Zamojski, M. A., Schiminovich, D., Rich, R. M., et al. 2007, ApJS, 172, 468
Zheng, W., Postman, M., Zitrin, A., et al. 2012, Natur, 489, 406
Zhu, G., Blanton, M. R., Burles, S. M., et al. 2011, ApJ, 726, 110
Zhu, G., Moustakas, J., & Blanton, M. R. 2009, ApJ, 701, 86
Zitrin, A., Moustakas, J., Bradley, L., et al. 2012, ApJL, 747, L9